

1 SEARCH FOR PRODUCTION OF A HIGGS BOSON AND A SINGLE TOP
2 QUARK IN MULTILEPTON FINAL STATES IN pp COLLISIONS AT $\sqrt{s} = 13$
3 TeV.

4 by

5 Jose Andres Monroy Montañez

A DISSERTATION

7 Presented to the Faculty of

8 The Graduate College at the University of Nebraska

9 In Partial Fulfilment of Requirements

10 For the Degree of Doctor of Philosophy

11 Major: Physics and Astronomy

¹² Under the Supervision of Kenneth Bloom and Aaron Dominguez

13 Lincoln, Nebraska

14 July, 2018

15 SEARCH FOR PRODUCTION OF A HIGGS BOSON AND A SINGLE TOP
16 QUARK IN MULTILEPTON FINAL STATES IN pp COLLISIONS AT $\sqrt{s} = 13$
17 TeV.

18 Jose Andres Monroy Montañez, Ph.D.

19 University of Nebraska, 2018

20 Adviser: Kenneth Bloom and Aaron Dominguez

²¹ Table of Contents

²² Table of Contents	iii
²³ List of Figures	vii
²⁴ List of Tables	x
²⁵ 1 INTRODUCTION	1
²⁶ 2 Theoretical approach	2
27 2.1 Introduction	2
28 2.2 Standard model of particle physics	3
29 2.2.1 Fermions	5
30 2.2.1.1 Leptons	6
31 2.2.1.2 Quarks	8
32 2.2.2 Fundamental interactions	13
33 2.2.3 Gauge bosons	18
34 2.3 Electroweak unification and the Higgs mechanism	20
35 2.3.1 Spontaneous symmetry breaking (SSB)	28
36 2.3.2 Higgs mechanism	32
37 2.3.3 Masses of the gauge bosons	35

38	2.3.4	Masses of the fermions	36
39	2.3.5	The Higgs field	37
40	2.3.6	Production of Higgs bosons at LHC	38
41	2.3.7	Higgs boson decay channels	42
42	2.4	Associated production of a Higgs boson and a single Top quark.	43
43	2.5	The CP-mixing in tH processes	47
44	2.6	Experimantal status of the anomalous Higg-fermion coupling.	52
45	3	The CMS experiment at the LHC	54
46	3.1	Introduction	54
47	3.2	The LHC	55
48	3.3	The CMS experiment	65
49	3.3.1	Coordinate system	67
50	3.3.2	Pixels detector	68
51	3.3.3	Silicon strip tracker	70
52	3.3.4	Electromagnetic calorimeter	72
53	3.3.5	Hadronic calorimeter	73
54	3.3.6	Superconducting solenoid magnet	75
55	3.3.7	Muon system	76
56	3.3.8	CMS trigger system	77
57	3.3.9	CMS computing	79
58	4	Event generation, simulation and reconstruction	83
59	4.1	Event generation	84
60	4.2	Monte Carlo Event Generators.	88
61	4.3	CMS detector simulation.	89
62	4.4	Event reconstruction.	91

63	4.4.1	Particle-Flow Algorithm.	92
64	4.4.2	Event reconstruction examples	104
65	5	Statistical methods	107
66	5.1	Multivariate analysis	107
67	5.1.1	Decision trees	110
68	5.1.2	Boosted decision trees (BDT)	113
69	5.1.3	Overtraining.	116
70	5.1.4	Variable ranking.	116
71	5.1.5	BDT output example.	117
72	5.2	Statistical inference.	118
73	5.2.1	Nuisance parameters.	118
74	5.2.2	Maximum likelihood estimation method	119
75	5.3	exclusion limits	120
76	5.4	asymptotic limits	120
77	6	Search for production of a Higgs boson and a single top quark in multilepton final states in pp collisions at $\sqrt{s} = 13$ TeV	121
79	6.1	Introduction	121
80	6.2	Data and MC Samples	123
81	6.2.1	Full 2016 dataset and MC samples	123
82	6.2.2	Triggers	126
83	6.2.2.1	Trigger efficiency scale factors	126
84	6.3	Object Identification and event selection	127
85	6.3.1	Jets and b tagging	127
86	6.3.2	Lepton selection	128
87	6.3.3	Lepton selection efficiency	129

88	6.4	Background predictions	130
89	6.5	Signal discrimination	131
90	6.5.1	Classifiers response	135
91	6.6	Additional discriminating variables	138
92	Bibliography		139
93	References		141

⁹⁴ List of Figures

95	2.1 Standard model of particle physics.	4
96	2.2 Transformations between quarks	12
97	2.3 Fundamental interactions in nature.	13
98	2.4 SM interactions diagrams	14
99	2.5 Neutral current processes	21
100	2.6 Spontaneous symmetry breaking mechanism	29
101	2.7 SSB Potential form	30
102	2.8 Potential for complex scalar field	31
103	2.9 SSB mechanism for complex scalar field	32
104	2.10 Proton-Proton collision	39
105	2.11 Higgs boson production mechanism Feynman diagrams	40
106	2.12 Higgs boson production cross section and decay branching ratios	41
107	2.13 Associated Higgs boson production mechanism Feynman diagrams	43
108	2.14 Cross section for tHq process as a function of κ_t	46
109	2.15 Cross section for tHW process as a function of κ_{Htt}	47
110	2.16 NLO cross section for tX_0 and $t\bar{t}X_0$	50
111	2.17 NLO cross section for tWX_0 , $t\bar{t}X_0$	51

112	2.18 Two dimentional κ_t - κ_V plot of the coupling modifiers. ATLAS and CMS 113 combination.	52
114	3.1 CERN accelerator complex	55
115	3.2 LHC protons source. First acceleration stage.	56
116	3.3 The LINAC2 accelerating system at CERN.	57
117	3.4 LHC layout and RF cavities module.	58
118	3.5 LHC dipole magnet.	60
119	3.6 Integrated luminosity delivered by LHC and recorded by CMS during 2016	62
120	3.7 LHC interaction points	63
121	3.8 Multiple pp collision bunch crossing at CMS.	65
122	3.9 Layout of the CMS detector	66
123	3.10 CMS detector coordinate system	67
124	3.11 CMS pixel detector schematic view.	70
125	3.12 SST Schematic view.	71
126	3.13 CMS ECAL schematic view	72
127	3.14 CMS HCAL schematic view	74
128	3.15 CMS solenoid magnet	75
129	3.16 CMS Muon system schematic view	76
130	3.17 CMS Level-1 trigger architecture	78
131	3.18 WLCG structure	80
132	3.19 Data flow from CMS detector through hardware Tiers	82
133	4.1 Event generation process.	84
134	4.2 Particle flow algorithm.	92
135	4.3 Jet reconstruction.	100
136	4.4 Jet energy corrections.	101

137	4.5	Secondary vertex in a b-hadron decay.	103
138	4.6	HIG-13-004 Event 1 reconstruction.	104
139	4.7	$e\mu$ event reconstruction.	105
140	4.8	Recorded event reconstruction.	106
141	5.1	Scatter plots-MVA event classification.	109
142	5.2	Scalar test statistical.	109
143	5.3	Decision tree.	111
144	5.4	Decision tree output example.	114
145	5.5	BDT output example.	117
146	6.1	The two leading-order diagrams of tHq production.	122
147	6.2	Input variables to the BDT for signal discrimination normalized.	132
148	6.3	Input variables to the BDT for signal discrimination not normalized.	134
149	6.4	BDT inputs as seen by TMVA against $t\bar{t}$.	135
150	6.5	BDT inputs as seen by TMVA against $t\bar{t}V$.	136
151	6.6	Correlation matrices for the input variables in the TMVA.	137
152	6.7	MVA classifiers performance.	137
153	6.8	Additional discriminating variables distributions.	139

¹⁵⁴ List of Tables

155	2.1	Fermions of the SM.	5
156	2.2	Fermion masses.	6
157	2.3	Leptons properties.	9
158	2.4	Quarks properties.	9
159	2.5	Fermion weak isospin and weak hypercharge multiplets.	11
160	2.6	Fundamental interactions features.	15
161	2.7	SM gauge bosons.	20
162	2.8	Higgs boson properties.	38
163	2.9	Predicted branching ratios for a SM Higgs boson with $m_H = 125 \text{ GeV}/c^2$	42
164	2.10	Predicted SM cross sections for tH production at $\sqrt{s} = 13 \text{ TeV}$	44
165	2.11	Predicted enhancement of the tHq and tHW cross sections at LHC	48
166	6.1	Signal samples and their cross section and branching fraction.	123
167	6.2	κ_V and κ_t combinations.	124
168	6.3	List of background samples used in this analysis (CMSSW 80X).	125
169	6.4	Leading-order $t\bar{t}W$ and $t\bar{t}Z$ samples used in the signal BDT training.	125
170	6.5	Table of high-level triggers that we consider in the analysis.	126
171	6.6	Trigger efficiency scale factors and associated uncertainties.	127
172	6.7	Requirements on each of the three muon selections.	128

173	6.8 Criteria for each of the three electron selections.	129
174	6.9 MVA input discriminating variables	133
175	6.10 TMVA input variables ranking for BDTA_GRAD method	138
176	6.11 TMVA configuration used in the BDT training.	138
177	6.12 ROC-integral for all the testing cases.	140

¹⁷⁸ Chapter 1

¹⁷⁹ INTRODUCTION

¹⁸⁰ **Chapter 2**

¹⁸¹ **Theoretical approach**

¹⁸² **2.1 Introduction**

¹⁸³ The physical description of the universe is a challenge that physicists have faced by
¹⁸⁴ making theories that refine existing principles and proposing new ones in an attempt
¹⁸⁵ to embrace emerging facts and phenomena.

¹⁸⁶

¹⁸⁷ At the end of 1940s Julian Schwinger [1] and Richard P. Feynman [2], based in the
¹⁸⁸ work of Sin-Itiro Tomonaga [3], developed an electromagnetic theory consistent with
¹⁸⁹ special relativity and quantum mechanics that describes how matter and light inter-
¹⁹⁰ act; the so-called “quantum eletrodynamics” (QED) had born.

¹⁹¹

¹⁹² QED has become the guide in the development of theories that describe the universe.
¹⁹³ It was the first example of a quantum field theory (QFT), which is the theoretical
¹⁹⁴ framework for building quantum mechanical models that describes particles and their
¹⁹⁵ interactions. QFT is composed of a set of mathematical tools that combines classical
¹⁹⁶ fields, special relativity and quantum mechanics, while keeping the quantum point

197 particles and locality ideas.

198 This chapter gives an overview of the standard model of particle physics, starting
 199 with a description of the particles and interactions that compose it, followed by a
 200 description of the electroweak interaction, the Higgs boson and the associated pro-
 201 duction of Higgs boson and a single top quark (tH). The description contained in
 202 this chapter is based on references [4–6].

203 2.2 Standard model of particle physics

204 Particle physics at the fundamental level is modeled in terms of a collection of in-
 205 teracting particles and fields in a theory known as the “standard model of particle
 206 physics (SM)”¹.

207

208 The full picture of the SM is composed of three fields², whose excitations are inter-
 209 preted as particles called mediators or force-carriers; a set of fields, whose excitations
 210 are interpreted as elementary particles, interacting through the exchange of those
 211 mediators and a field that gives the mass to elementary particles. Figure 2.1 shows
 212 an scheme of the SM particles organization. In addition to the particles in the scheme
 213 (but not listed in it), their corresponding anti-particles, with opposite quantum num-
 214 bers, are also part of the picture; some particles are their own anti-particles, like
 215 photon or Higgs, or anti-particle is already listed like in the W^+ and W^- case.

216

217 The mathematical formulation of the SM is based on group theory and the use of
 218 Noether’s theorem [8] which states that for a physical system modeled by a Lagrangian

¹ The formal and complete treatment of the SM is out of the scope of this document, however a plenty of textbooks describing it at several levels are available in the literature. The treatment in references [?] is quite comprehensive and detailed.

² Note that gravitational field is not included in the standard model formulation

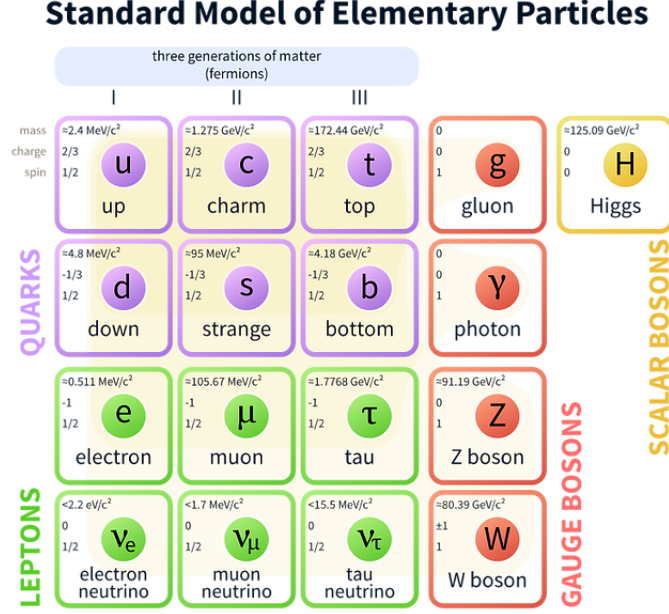


Figure 2.1: Schematic representation of the Standard model of particle physics. SM is a theoretical model intended to describe three of the four fundamental forces of the universe in terms of a set of particles and their interactions. [7].

that is invariant under a group of transformations a conservation law is expected. For instance, a system described by a time-independent Lagrangian is invariant (symmetric) under time changes (transformations) with the total energy conservation law as the expected conservation law. In QED, the charge operator (Q) is the generator of the $U(1)$ symmetry which according to the Noether's theorem means that there is a conserved quantity; this conserved quantity is the electric charge and thus the law of conservation of electric charge is established.

226

227 In the SM, the symmetry group $SU(3)_C \otimes SU(2)_L \otimes U(1)_Y$ describes three of the 228 four fundamental interactions in nature(see section 2.2.2): strong interaction(SI), 229 weak interaction(WI) and electromagnetic interactions (EI) in terms of symmetries 230 associated to physical quantities:

- 231 • Strong: $SU(3)_C$ associated to color charge
- 232 • Weak: $SU(2)_L$ associated to weak isospin and chirality
- 233 • Electromagnetic: $U(1)_Y$ associated to weak hypercharge and electric charge
- 234 It will be shown that the electromagnetic and weak interactions are combined in
 235 the so-called electroweak interaction where chirality, hypercharge, weak isospin and
 236 electric charge are the central concepts.

237 2.2.1 Fermions

238 The basic constituents of the ordinary matter at the lowest level, which form the set
 239 of elementary particles in the SM formulation, are quarks and leptons. All of them
 240 have spin 1/2, therefore they are classified as fermions since they obey Fermi-Dirac
 241 statistics. There are six “flavors” of quarks and three of leptons organized in three
 242 generations, or families, as shown in table 2.1.

243

		Generation		
		1st	2nd	3rd
Leptons	Charged	Electron (e)	Moun(μ)	Tau (τ)
	Neutral	Electron neutrino (ν_e)	Muon neutrino (ν_μ)	Tau neutrino (ν_τ)
Quarks	Up-type	Up (u)	Charm (c)	Top (t)
	Down-type	Down (d)	Strange (s)	Bottom (b)

Table 2.1: Fermions of the SM. There are six flavors of quarks and three of leptons, organized in three generations, or families, composed of two pairs of closely related particles. The close relationship is motivated by the fact that WI between leptons is limited to the members of the same generation; WI between quarks is not limited but greatly favoured, to same generation members.

244

245 There is a mass hierarchy between generations (see table 2.2), where the higher gener-
 246 ation particles decays to the lower one, which can explain why the ordinary matter is

made of particles in the first generation. In the SM, neutrinos are modeled as massless particles so they are not subject to this mass hierarchy; however, today it is known that neutrinos are massive so the hierarchy could be restated. The reason behind this mass hierarchy is one of the most important open questions in particle physics, and it becomes more puzzling when noticing that the mass difference between first and second generation fermions is small compared to the mass difference with respect to the third generation.

Lepton	Mass (MeV/c ²)	Quark	Mass (MeV/c ²)
e	0.51	u	2.2
μ	105.65	c	1.28×10^3
τ	1776.86	t	173.1×10^3
ν_e	Unknown	d	4.7
ν_μ	Unknown	s	96
τ_μ	Unknown	b	4.18×10^3

Table 2.2: Fermion masses [9]. Generations differ by mass in a way that have been interpreted as a masss hierarchy. Approximate values with no uncertainties are used, for comparison purpose.

Usually, the second and third generation fermions are produced in high energy processes, like the ones recreated in particle accelerators.

2.2.1.1 Leptons

A lepton is an elementary particle that is not subject to the SI. As seen in table 2.1, there are two types of leptons, the charged ones (electron, muon and tau) and the neutral ones (the three neutrinos). The electric charge (Q) is the property that gives leptons the ability to participate in the EI. From the classical point of view, Q plays a central role determining, among others, the strength of the electric field through which the electromagnetic force is exerted. It is clear that neutrinos are not affected

264 by EI because they don't carry electric charge.

265

266 Another feature of the leptons that is fundamental in the mathematical description
267 of the SM is the chirality, which is closely related to spin and helicity. Helicity defines
268 the handedness of a particle by relating its spin and momentum such that if they
269 are parallel then the particle is right-handed; if spin and momentum are antiparallel
270 the particle is said to be left-handed. The study of parity conservation (or viola-
271 tion) in β -decay has shown that only left-handed electrons/neutrinos or right-handed
272 positrons/anti-neutrinos are created [10]; the inclusion of that feature in the theory
273 was achieved by using projection operators for helicity, however, helicity is frame de-
274 pendent for massive particles which makes it not Lorentz invariant and then another
275 related attribute has to be used: *chirality*.

276

277 Chirality is a purely quantum attribute which makes it not so easy to describe in
278 graphical terms but it defines how the wave function of a particle transforms under
279 certain rotations. As with helicity, there are two chiral states, left-handed chiral (L)
280 and right-handed chiral (R). In the highly relativistic limit where $E \approx p \gg m$ helicity
281 and chirality converge, becoming exactly the same for massless particles.

282

283 In the following, when referring to left-handed (right-handed) it will mean left-handed
284 chiral (right-handed chiral). The fundamental fact about chirality is that while EI
285 and SI are not sensitive to chirality, in WI left-handed and right-handed fermions are
286 treated asymmetrically, such that only left handed fermions and right-handed anti-
287 fermions are allowed to couple to WI mediators, which is a violation of parity. The
288 way to translate this statement in a formal mathematical formulation is based on the
289 isospin symmetry group $SU(2)_L$.

290

291 Each generation of leptons is seen as a weak isospin doublet.³ The left-handed charged
 292 lepton and its associated left-handed neutrino are arranged in doublets of weak isospin
 293 T=1/2 while their right-handed partners are singlets:

$$\begin{pmatrix} \nu_l \\ l \end{pmatrix}_L, l_R := \begin{pmatrix} \nu_e \\ e \end{pmatrix}_L, \begin{pmatrix} \nu_\mu \\ \mu \end{pmatrix}_L, \begin{pmatrix} \nu_\tau \\ \tau \end{pmatrix}_L, e_R, \mu_R, \tau_R, \nu_{eR}, \nu_{\mu R}, \nu_{\tau R} \quad (2.1)$$

294 The isospin third component refers to the eigenvalues of the weak isospin operator
 295 which for doublets is $T_3 = \pm 1/2$, while for singlets it is $T_3 = 0$. The physical meaning
 296 of this doublet-singlet arrangement falls in that the WI couples the two particles in
 297 the doublet by exchanging the interaction mediator while the singlet member is not
 298 involved in WI. The main properties of the leptons are summarized in table 2.3.

299

300 Altough all three flavor neutrinos have been observed, their masses remain unknown
 301 and only some estimations have been made [11]. The main reason is that the fla-
 302 vor eigenstates are not the same as the mass eigenstates which implies that when
 303 a neutrino is created its mass state is a linear combination of the three mass eigen-
 304 states and experiments can only probe the squared difference of the masses. The
 305 Pontecorvo-Maki-Nakagawa-Sakata (PMNS) mixing matrix encode the relationship
 306 between flavor and mass eigenstates.

307

308 2.2.1.2 Quarks

309 Quarks are the basic constituents of protons and neutrons. The way quarks join to
 310 form bound states, called “hadrons”, is through the SI. Quarks are affected by all the

³ The weak isospin is an analogy of the isospin symmetry in strong interaction where neutron and proton are affected equally by strong force but differ in their charge.

Lepton	Q(e)	T_3	L_e	L_μ	L_τ	Lifetime (s)
Electron (e)	-1	-1/2	1	0	0	Stable
Electron neutrino(ν_e)	0	1/2	1	0	0	Unknown
Muon (μ)	-1	-1/2	0	1	0	2.19×10^{-6}
Muon neutrino (ν_μ)	0	1/2	0	1	0	Unknown
Tau (τ)	-1	-1/2	0	0	1	290.3×10^{-15}
Tau neutrino (τ_μ)	0	1/2	0	0	1	Unknown

Table 2.3: Leptons properties [9]. Q: electric charge, T_3 : weak isospin. Only left-handed leptons and right-handed anti-leptons participate in the WI. Anti-particles with inverted T_3 , Q and lepton number complete the leptons set but are not listed. Right-handed leptons and left-handed anti-leptons, neither listed, form weak isospin singlets with $T_3 = 0$ and do not take part in the weak interaction.

311 fundamental interactions which means that they carry all the four types of charges:
 312 color, electric charge, weak isospin and mass.

Flavor	Q(e)	I_3	T_3	B	C	S	T	B'	Y	Color
Up (u)	2/3	1/2	1/2	1/3	0	0	0	0	1/3	r,b,g
Charm (c)	2/3	0	1/2	1/3	1	0	0	0	4/3	r,b,g
Top(t)	2/3	0	1/2	1/3	0	0	1	0	4/3	r,b,g
Down(d)	-1/3	-1/2	-1/2	1/3	0	0	0	0	1/3	r,b,g
Strange(s)	-1/3	0	-1/2	1/3	0	-1	0	0	-2/3	r,b,g
Bottom(b)	-1/3	0	-1/2	1/3	0	0	0	-1	-2/3	r,b,g

Table 2.4: Quarks properties [9]. Q: electric charge, I_3 : isospin, T_3 : weak isospin, B: baryon number, C: charmness, S: strangeness, T: topness, B' : bottomness, Y: hypercharge. Anti-quarks posses the same mass and spin as quarks but all charges (color, flavor numbers) have opposite sign.

313
 314 Table 2.4 summarizes the features of quarks, among which the most particular is
 315 their fractional electric charge. Note that fractional charge is not a problem, given
 316 that quarks are not found isolated, but serves to explain how composed particles are
 317 formed out of two or more valence quarks⁴.
 318

⁴ Hadrons can contain an indefinite number of virtual quarks and gluons, known as the quark and gluon sea, but only the valence quarks determine hadrons' quantum numbers.

319 Color charge is the responsible for the SI between quarks and is the symmetry
 320 ($SU(3)_C$) that defines the formalism to describe SI. There are three colors: red (r),
 321 blue(b) and green(g) and their corresponding three anti-colors; thus each quark carries
 322 one color unit while anti-quarks carries one anti-color unit. As said above, quarks are
 323 not allowed to be isolated due to the color confinement effect, therefore their features
 324 have been studied indirectly by observing their bound states created when:

- 325 • one quark with a color charge is attracted by an anti-quark with the correspond-
 326 ing anti-color charge forming a colorless particle called a “meson.”
- 327 • three quarks (anti-quarks) with different color (anti-color) charges are attracted
 328 among them forming a colorless particle called a “baryon(anti-baryon).”

329 In practice, when a quark is left alone isolated a process called “hadronization” occurs
 330 where the quark emits gluons (see section 2.2.3) which eventually will generate new
 331 quark-antiquark pairs and so on; those quarks will recombine to form hadrons that
 332 will decay into leptons. This proliferation of particles looks like a “jet” coming from
 333 the isolated quark. More details about the hadronization process and jet structure
 334 will be given in chapter4.

335 In the first version of the quark model (1964), M. Gell-Mann [12] and G. Zweig
 336 [13, 14] developed a consistent way to classify hadrons according to their properties.
 337 Only three quarks (u, d, s) were involved in a scheme in which all baryons have
 338 baryon number $B=1$ and therefore quarks have $B=1/3$; non-baryons have $B=0$. The
 339 scheme organizes baryons in a two-dimensional space ($I_3 - Y$); Y (hypercharge) and I_3
 340 (isospin) are quantum numbers related by the Gell-Mann-Nishijima formula [15, 16]:

$$Q = I_3 + \frac{Y}{2} \quad (2.2)$$

341 where $Y = B + S + C + T + B'$ are the quantum numbers listed in table 2.4. Baryon
 342 number is conserved in SI and EI which means that single quarks cannot be created
 343 but in pairs $q - \bar{q}$.

344

345 There are six quark flavors organized in three generations (see table 2.1) following a
 346 mass hierarchy which, again, implies that higher generations decay to first generation
 347 quarks.

	Quarks			T_3	Y_W	Leptons			T_3	Y_W
Doublets	$(\begin{smallmatrix} u \\ d' \end{smallmatrix})_L$	$(\begin{smallmatrix} c \\ s' \end{smallmatrix})_L$	$(\begin{smallmatrix} t \\ b' \end{smallmatrix})_L$	$(\begin{smallmatrix} 1/2 \\ -1/2 \end{smallmatrix})$	1/3	$(\begin{smallmatrix} \nu_e \\ e \end{smallmatrix})_L$	$(\begin{smallmatrix} \nu_\mu \\ \mu \end{smallmatrix})_L$	$(\begin{smallmatrix} \nu_\tau \\ \tau \end{smallmatrix})_L$	$(\begin{smallmatrix} 1/2 \\ -1/2 \end{smallmatrix})$	-1
Singlets	u_R	c_R	t_R	0	4/3	ν_{eR}	$\nu_{\mu R}$	$\nu_{\tau R}$	0	-2
	d'_R	s'_R	b'_R	0	-2/3	e_R	μ_R	τ_R		

Table 2.5: Fermion weak isospin and weak hypercharge multiplets. Weak hypercharge is calculated through the Gell-Mann-Nishijima formula 2.2 but using the weak isospin and charge for quarks.

348

349 Isospin doublets of quarks are also defined (see table 2.5) and as for neutrinos, the
 350 mass eigenstates are not the same as the WI eigenstates which means that members of
 351 different quark generations are connected by the WI mediator; thus, up-type quarks
 352 are coupled not to down-type quarks directly but to a superposition of down-type
 353 quarks (q'_d) via WI according to:

$$q'_d = V_{CKM} q_d$$

354

$$\begin{pmatrix} d' \\ s' \\ b' \end{pmatrix} = \begin{pmatrix} V_{ud} & V_{us} & V_{ub} \\ V_{cd} & V_{cs} & V_{cb} \\ V_{td} & V_{ts} & V_{tb} \end{pmatrix} \begin{pmatrix} d \\ s \\ b \end{pmatrix} \quad (2.3)$$

355 where V_{CKM} is known as Cabibbo-Kobayashi-Maskawa (CKM) mixing matrix [17,18].

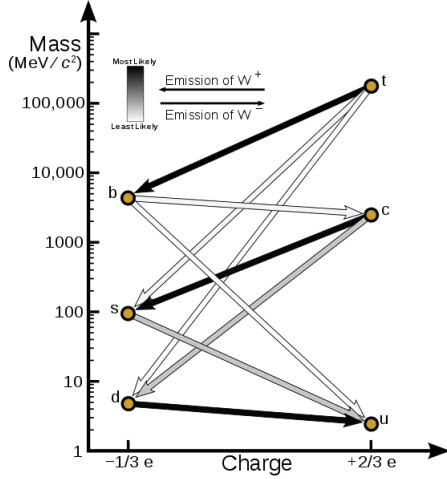


Figure 2.2: Transformations between quarks through the exchange of a WI. Higher generations quarks decay to first generation quarks by emitting a W boson. The arrow color indicates the likelihood of the transition according to the grey scale in the top left side which represent the CKM matrix parameters [19].

356 The weak decays of quarks are represented in the diagram of figure 2.2; again the
 357 CKM matrix plays a central role since it contains the probabilities for the different
 358 quark decay channels, in particular, note that quark decays are greatly favored be-
 359 tween generation members.

360

361 CKM matrix is a 3×3 unitary matrix parametrized by three mixing angles and
 362 the *CP-mixing phase*; the latter is the parameter responsible for the Charge-Parity
 363 symmetry violation (CP-violation) in the SM. The fact that the b quark decays almost
 364 all the times to a top quark is exploited in this thesis when making the selection of
 365 the signal events by requiring the presence of a jet tagged as a jet coming from a
 366 b quark in the final state. The effect of the *CP-mixing phase* on the cross section of
 367 associated production of Higgs boson and a single top process is also explored in this
 368 thesis.

369 2.2.2 Fundamental interactions

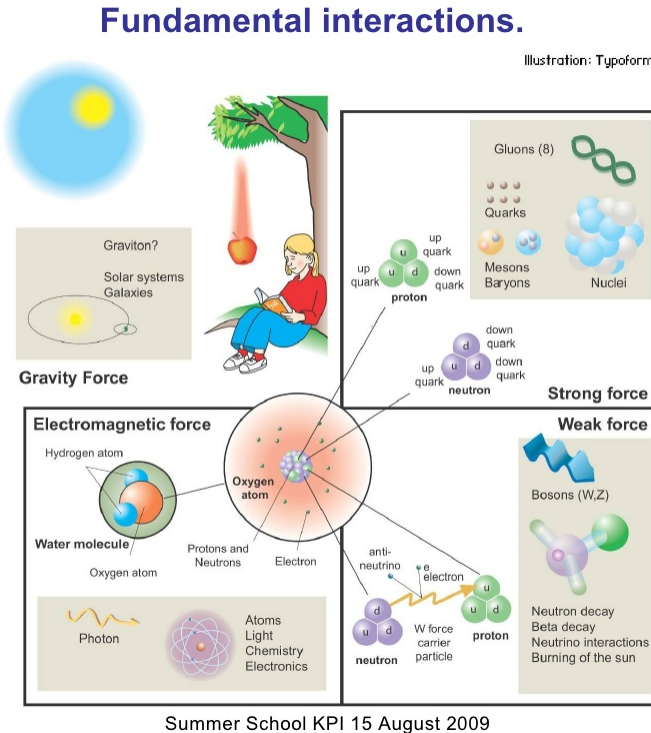


Figure 2.3: Fundamental interactions in nature. Despite the many manifestations of forces in nature, we can track all of them back to one of the fundamental interactions. The most common forces are gravity and electromagnetic given that all of us are subject and experience them in everyday life.

370 Even though there are many manifestations of force in nature, like the ones represented in figure 2.3, we can classify all of them into one of four fundamental interactions:

- 373 • *Electromagnetic interaction (EI)* affects particles that are “electrically charged,”
 374 like electrons and protons. It is described by QED combining quantum mechanics,
 375 special relativity and electromagnetism in order to explain how particles
 376 with electric charge interact through the exchange of photons, therefore, one
 377 says that “Electromagnetic Force” is mediated by “photons”. Figure 2.4a. shows

378 a graphical representation, known as “feynman diagram”, of electron-electron
 379 scattering.

- 380 • *Strong interaction (SI)* described by Quantum Chromodynamics (QCD). Hadrons
 381 like proton and neutron have internal structure given that they are composed
 382 of two or more valence quarks⁵. Quarks have fractional electric charge which
 383 means that they are subject to electromagnetic interaction and in the case of the
 384 proton they should break apart due to electrostatic repulsion; however, quarks
 385 are held together inside the hadrons against their electrostatic repulsion by the
 386 “Strong Force” through the exchange of “gluons.” The analog to the electric
 387 charge is the “color charge”. Electrons and photons are elementary particles
 388 as quarks but they don’t carry color charge, therefore they are not subject to
 389 SI. The feynman diagram for gluon exchange between quarks is shown in figure
 390 2.4b.

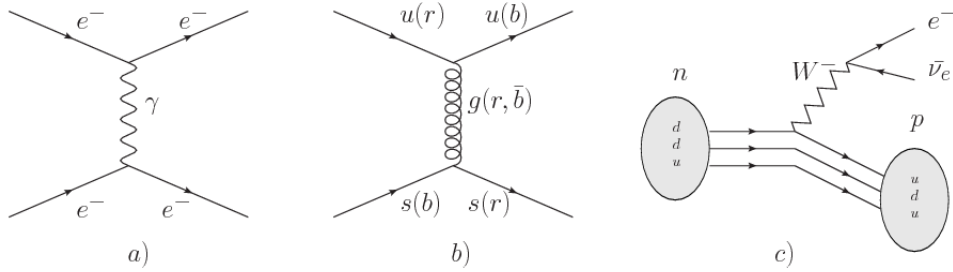


Figure 2.4: Feynman diagrams representing the interactions in SM; a) EI: e-e scattering; b) SI: gluon exchange between quarks ; c) WI: β -decay

- 391 • *Weak interaction (WI)* described by the weak theory (WT), is responsible, for
 392 instance, for the radioactive decay in atoms and proton-proton (pp) fusion
 393 within the sun. Quarks and leptons are the particles affected by the weak
 394 interaction; they possess a property called “flavor charge” (see 2.2.1) which can
 395 be changed by emitting or absorbing one weak force mediator. There are three

⁵ particles made of four and five quarks are exotic states not so common.

396 mediators of the “weak force” known as “Z” boson in the case of electrically
 397 neutral changes and “ W^\pm ” bosons in the case of electrically charged changes.
 398 The “weak isospin” is the WI analog to electric charge in EI, and color charge
 399 in SI, and defines how quarks and leptons are affected by the weak force. Figure
 400 2.4c. shows the feynman diagram of β -decay where a newtron (n) is transformed
 401 in a proton (p) by emmiting a W^- particle. Since this thesis is in the frame
 402 of the electroweak interaction, a more detailed description of it will be given in
 403 section 2.3

404 • *Gravitational interaction (GI)* described by General Theory of Relativity (GR).
 405 It is responsible for the structure of galaxies and black holes as well as the
 406 expansion of the universe. As a classical theory, in the sense that it can be for-
 407 mulated without even appeal to the concept of quantization, it implies that the
 408 spacetime is a continuum and predictions can be made without limitation to the
 409 precision of the measurement tools. The latter represent a direct contradiction
 410 of the quantum mechanics principles. Gravity is deterministic while quantum
 411 mechanics is probabilistic; despite that, efforts to develop a quantum theory of
 412 gravity have predicted the “graviton” as mediator of the Gravitational force⁶.

Interaction	Acts on	Relative strength	Range (m)	Mediators
Electromagnetic (QED)	Electrically charged particles	10^{-2}	Infinite	Photon
Strong (QCD)	Quarks and gluons	1	10^{-15}	Gluon
Weak (WI)	Leptons and quarks	10^{-6}	10^{-18}	W^\pm , Z
Gravitational (GI)	Massive particles	10^{-39}	Infinite	Graviton

Table 2.6: Fundamental interactions features [20].

413

⁶ Actually a wide variety of theories have been developed in an attempt to describe gravity; some famous examples are string theory and supergravity.

414 Table 2.6 summarizes the main features of the fundamental interactions. The rela-
 415 tive strength of the fundamental forces reveals the meaning of strong and weak; in
 416 a context where the relative strength of the SI is 1, the EI is about hundred times
 417 weaker and WI is about million times weaker than the SI. A good description on
 418 how the relative strength and range of the fundamental interactions are calculated
 419 can be found in references [20, 21]. In the everyday life, only EI and GI are explicitly
 420 experienced due to the range of these interactions; i.e., at the human scale distances
 421 only EI and GI have appreciable effects, in contrast to SI which at distances greater
 422 than 10^{-15} m become negligible.

423

424 QED was built successfully on the basis of the classical electrodynamics theory (CED)
 425 of Maxwell and Lorentz, following theoretical and experimental requirements imposed
 426 by

- 427 • lorentz invariance: independence on the reference frame.
- 428 • locality: interacting fields are evaluated at the same space-time point to avoid
 429 action at a distance.
- 430 • renormalizability: physical predictions are finite and well defined
- 431 • particle spectrum, symmetries and conservation laws already known must emerge
 432 from the theory.
- 433 • gauge invariance.

434 The gauge invariance requirement reflects the fact that the fundamental fields cannot
 435 be directly measured but associated fields which are the observables. Electric (“E”)
 436 and magnetic (“B”) fields in CED are associated with the electric scalar potential

437 “V” and the vector potential “A”. In particular, \mathbf{E} can be obtained by measuring
 438 the change in the space of the scalar potential (ΔV); however, two scalar potentials
 439 differing by a constant “f” correspond to the same electric field. The same happens in
 440 the case of the vector potential “A”; thus, different configurations of the associated
 441 fields result in the same set of values of the observables. The freedom in choosing
 442 one particular configuration is known as “gauge freedom”; the transformation law con-
 443 necting two configurations is known as “gauge transformation” and the fact that the
 444 observables are not affected by a gauge transformation is called “gauge invariance”.

445

446 When the gauge transformation:

$$\begin{aligned} \mathbf{A} &\rightarrow \mathbf{A} - \Delta f \\ V &\rightarrow V - \frac{\partial f}{\partial t} \end{aligned} \tag{2.4}$$

447 is applied to Maxwell equations, they are still satisfied and the fields remain invariant.
 448 Thus, CED is invariant under gauge transformations and is called a “gauge theory”.
 449 The set of all gauge transformations form the “symmetry group” of the theory, which
 450 according to the group theory, has a set of “group generators”. The number of group
 451 generators determine the number of “gauge fields” of the theory.

452

453 As mentioned in the first lines of section 2.2, QED has one symmetry group ($U(1)$)
 454 with one group generator (the Q operator) and one gauge field (the electromagnetic
 455 field A^μ). In CED there is not a clear definition, beyond the historical convention, of
 456 which fields are the fundamental and which are the associated, but in QED it is clear
 457 that the fundamental field is A^μ . When a gauge theory is quantized, the gauge field

458 is quantized and its quanta is called “gauge boson”. The word boson characterizes
 459 particles with integer spin which obvey Bose-einstein statistics.

460

461 As will be detailed in section 2.3, interactions between partcles in a system can be
 462 obtained by considering first the Lagrangian density of free particles in the system,
 463 which of course is incomplete because the interaction terms have been left out, and
 464 demanding global phase transformation invariance. Global phase transformation in-
 465 variance means that a gauge transformation is performed identically to every point
 466 in the space⁷ and the Lagrangian remains invariant. Then, the global transformation
 467 is promoted to a local phase transformation (this time the gauge transformation de-
 468 pends on the position in space) and again invariance is required.

469

470 Due to the space dependence of the local tranformation, the Lagrangian density is
 471 not invariant anymore. In order to restate the gauge invariance, the gauge covariant
 472 derivative is introduced in the Lagrangian and with it the gauge field responsible for
 473 the interaction between particles in the system. The new Lagrangian density is gauge
 474 invariant, includes the interaction terms needed to account for the interactions and
 475 provides a way to explain the interaction between particles through the exchange of
 476 the gauge boson.

477 This recipe was used to build QED and the theories that aim to explain the funda-
 478 mental interactions.

479 **2.2.3 Gauge bosons**

480 The importance of the gauge bosons comes from the fact that they are the force
 481 mediators or force carriers. The features of the gauge bosons reflect those of the

⁷ Here space corresponds to the 4-dimensional space i.e. space-time.

482 fields they represent and they are extracted from the Lagrangian density used to
 483 describe the interactions. In section 2.3, it will be shown how the gauge bosons of the
 484 EI and WI emerge from the electroweak Lagrangian. The SI gauge bosons features
 485 are also extracted from the SI Lagrangian but it is not detailed in this document. The
 486 main features of the SM gauge bosons will be briefly presented below and summarized
 487 in table 2.7.

- 488 • **Photon.** EI occurs when the photon couples to (is exchanged between) particles
 489 carrying electric charge; however, the photon itself does not carry electric charge,
 490 therefore, there is no coupling between photons. Given that the photon is
 491 massless the EI is of infinite range, i.e., electrically charged particles interact
 492 even if they are located far away one from each other; this also implies that
 493 photons always move with the speed of light.
- 494 • **Gluon.** SI is mediated by gluons which, same as photons, are massless. They
 495 carry one unit of color charge and one unit of anticolor charge which means that
 496 gluons couple to other gluons. As a result, the range of the SI is not infinite
 497 but very short due to the attraction between gluons, giving rise to the “color
 498 confinement” which explains why color charged particles cannot be isolated but
 499 live within composited particles, like quarks inside protons.
- 500 • **W, Z.** The WI mediators, W^\pm and Z, are massive which explains their short-
 501 range. Given that the WI is the only interaction that can change the flavor
 502 of the interacting particles, the W boson is the responsible for the nuclear
 503 transmutation where a neutron is converted in a proton or vice versa with the
 504 involvement of an electron and a neutrino (see figure 2.4c). The Z boson is the
 505 responsible of the neutral weak processes like neutrino elastic scattering where

506 no electric charge but momentum transference is involved. WI gauge bosons
 507 carry isospin charge which makes possible the interaction between them.

Interaction	Mediator	Electric charge (e)	Color charge	Weak Isospin	mass (GeV/c ²)
Electromagnetic	Photon (γ)	0	No	0	0
Strong	Gluon (g)	0	Yes -octet	No	0
Weak	W^\pm Z	± 1 0	No No	± 1 0	80.385 ± 0.015 91.188 ± 0.002

Table 2.7: SM gauge bosons main features [9].

508

509 **2.3 Electroweak unification and the Higgs 510 mechanism**

511 Physicists dream of building a theory that contains all the interactions in one single
 512 interaction, i.e., showing that at some scale in energy all the four fundamental in-
 513 teractions are unified and only one interaction emerges in a “Theory of everything”.
 514 The first sign of the feasibility of such unification comes from success in the con-
 515 struction of the CED. Einstein spent years trying to reach that dream, which by
 516 1920 only involved electromagnetism and gravity, with no success; however, a new
 517 partial unification was achieved in the 1960’s, when S.Glashow [22], A.Salam [23] and
 518 S.Weinberg [24] independently proposed that electromagnetic and weak interactions
 519 are two manifestations of a more general interaction called “electroweak interaction
 520 (EWT)”. Both, QCD and EWT, were developed in parallel and following the useful
 521 prescription provided by QED and the gauge invariance principles.

522

523 The theory of weak interactions was capable of explaining the β -decay and in general
 524 the processes mediated by W^\pm bosons. However, there were some processes like the

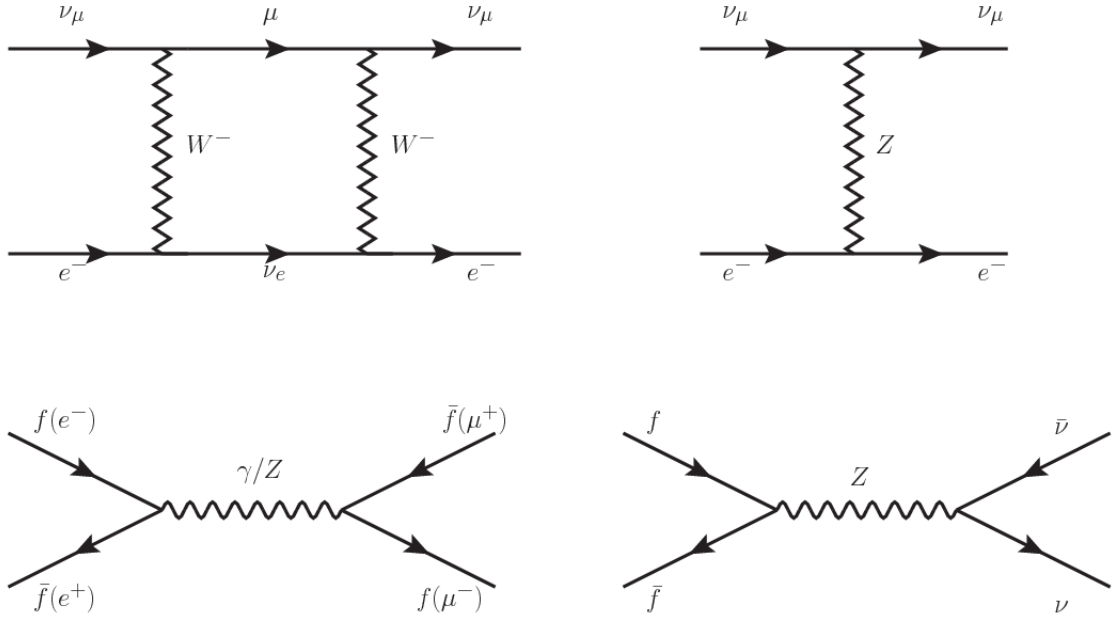


Figure 2.5: Top: $\nu_\mu - e^-$ scattering going through charged currents (left) and neutral currents (right). Bottom: neutral current processes for charged fermions (left) and involving neutrinos (right). While neutral current processes involving only charged fermions can proceed through EI or WI, those involving neutrinos can only proceed via WI.

525 “ $\nu_\mu - e$ scattering” which would require the exchange of two W bosons (see figure 2.5
526 top diagrams) giving rise to divergent loop integrals and then non finite predictions.
527 By including neutral currents involving fermions via the exchange of neutral bosons
528 Z , those divergences are compensated and the predictions become realistic.

529

530 Neutral weak interaction vertices conserve flavor in the same way as the electromag-
531 netic vertices do, but additionally, the Z boson can couple to neutrinos which implies
532 that processes involving charged fermions can proceed through EI or WI but processes
533 involving neutrinos can proceed only through WI.

534

535 The prescription to build a gauge theory of the WI consists of proposing a free field
536 Lagrangian density that includes the particles involved; next, by requesting invari-

537 ance under global phase transformations first and generalizing to local phase trans-
 538 formations invariance later, the conserved currents are identified and interactions are
 539 generated by introducing gauge fields. Given that the goal is to include the EI and
 540 WI in a single theory, the group symmetry considered should be a combination of
 541 $SU(2)_L$ and $U(1)_{em}$, however the latter cannot be used directly because the EI treats
 542 left and right-handed particles indistinctly in contrast to the former. Fortunately, the
 543 weak hypercharge, which is a combination of the weak isospin and the electric charge
 544 (eqn 2.2) is suitable to be used since it is conserved by the EI and WI. Thus, the
 545 symmetry group to be considered is

$$G \equiv SU(2)_L \otimes U(1)_Y \quad (2.5)$$

546 The following treatment applies to any of the fermion generations, but for simplicity
 547 the first generation of leptons will be considered [5, 6, 25, 26].

548

549 Given the first generation of leptons

$$\psi_1 = \begin{pmatrix} \nu_e \\ e^- \end{pmatrix}_L, \quad \psi_2 = \nu_{eR}, \quad \psi_3 = e_R^- \quad (2.6)$$

550 the charged fermionic currents are given by

$$J_\mu \equiv J_\mu^+ = \bar{\nu}_{eL} \gamma_\mu e_L, \quad J_\mu^\dagger \equiv J_\mu^- = \bar{e}_L \gamma_\mu \nu_{eL} \quad (2.7)$$

551 and the free Lagrangian is given by

$$\mathcal{L}_0 = \sum_{j=1}^3 i\bar{\psi}_j(x) \gamma^\mu \partial_\mu \psi_j(x). \quad (2.8)$$

552 Mass terms are included directly in the QED and QCD free Lagrangians since they

553 preserve the invariance under the symmetry transformations involved which treat
 554 left-handed and right-handed similarly, however mass terms of the form

$$m_W^2 W_\mu^\dagger(x) W^\mu(x) + \frac{1}{2} m_Z^2 Z_\mu(x) Z^\mu(x) - m_e \bar{\psi}_e(x) \psi_e(x) \quad (2.9)$$

555 which represent the mass of W^\pm , Z and electrons, are not invariant under G trans-
 556 formations, therefore the gauge fields described by the EWI are in principle massless.

557

558 Experiments have shown that the gauge fields are not massless; however, they have
 559 to acquire mass through a mechanism compatible with the gauge invariance; that
 560 mechanism is known as the “Higgs mechanism” and will be considered later in this
 561 section. The global transformations in the combined symmetry group G can be
 562 written as

$$\begin{aligned} \psi_1(x) &\xrightarrow{G} \psi'_1(x) \equiv U_Y U_L \psi_1(x), \\ \psi_2(x) &\xrightarrow{G} \psi'_2(x) \equiv U_Y \psi_2(x), \\ \psi_3(x) &\xrightarrow{G} \psi'_3(x) \equiv U_Y \psi_3(x) \end{aligned} \quad (2.10)$$

563 where U_L represent the $SU(2)_L$ transformation acting only on the weak isospin dou-
 564 blet and U_Y represent the $U(1)_Y$ transformation acting on all the weak isospin mul-
 565 tiplets. Explicitly

$$U_L \equiv \exp\left(i \frac{\sigma_i}{2} \alpha^i\right), \quad U_Y \equiv \exp(i y_i \beta) \quad (i = 1, 2, 3) \quad (2.11)$$

566 with σ_i the Pauli matrices and y_i the weak hypercharges. In order to promote the
 567 transformations from global to local while keeping the invariance, it is required that

568 $\alpha^i = \alpha^i(x)$, $\beta = \beta(x)$ and the replacement of the ordinary derivatives by the covariant
 569 derivatives

$$\begin{aligned} D_\mu \psi_1(x) &\equiv \left[\partial_\mu + ig\sigma_i W_\mu^i(x)/2 + ig'y_1 B_\mu(x) \right] \psi_1(x) \\ D_\mu \psi_2(x) &\equiv \left[\partial_\mu + ig'y_2 B_\mu(x) \right] \psi_2(x) \\ D_\mu \psi_3(x) &\equiv \left[\partial_\mu + ig'y_3 B_\mu(x) \right] \psi_3(x) \end{aligned} \quad (2.12)$$

570 introducing in this way four gauge fields, $W_\mu^i(x)$ and $B_\mu(x)$, in the process. The
 571 covariant derivatives (eqn 2.12) are required to transform in the same way as fermion
 572 fields $\psi_i(x)$ themselves, therefore, the gauge fields transform as:

$$\begin{aligned} B_\mu(x) &\xrightarrow{G} B'_\mu(x) \equiv B_\mu(x) - \frac{1}{g'} \partial_\mu \beta(x) \\ W_\mu^i(x) &\xrightarrow{G} W_\mu^{i\prime}(x) \equiv W_\mu^i(x) - \frac{i}{g} \partial_\mu \alpha_i(x) - \varepsilon_{ijk} \alpha_i(x) W_\mu^j(x). \end{aligned} \quad (2.13)$$

573 The G invariant version of the Lagrangian density 2.8 can be written as

$$\mathcal{L}_0 = \sum_{j=1}^3 i\bar{\psi}_j(x) \gamma^\mu D_\mu \psi_j(x) \quad (2.14)$$

574 where free massless fermion and gauge fields and fermion-gauge boson interactions
 575 are included. The EWI Lagrangian density must additionally include kinetic terms
 576 for the gauge fields (\mathcal{L}_G) which are built from the field strengths, according to

$$B_{\mu\nu}(x) \equiv \partial_\mu B_\nu - \partial_\nu B_\mu \quad (2.15)$$

$$W_{\mu\nu}^i(x) \equiv \partial_\mu W_\nu^i(x) - \partial_\nu W_\mu^i(x) - g\varepsilon^{ijk}W_\mu^j W_\nu^k \quad (2.16)$$

577 the last term in eqn. 2.16 is added in order to hold the gauge invariance; therefore,

$$\mathcal{L}_G = -\frac{1}{4}B_{\mu\nu}(x)B^{\mu\nu}(x) - \frac{1}{4}W_{\mu\nu}^i(x)W_i^{\mu\nu}(x) \quad (2.17)$$

578 which contains not only the free gauge fields contributions, but also the gauge fields
579 self-interactions and interactions among them.

580

581 The three weak isospin conserved currents resulting from the $SU(2)_L$ symmetry are
582 given by

$$J_\mu^i(x) = \frac{1}{2}\bar{\psi}_1(x)\gamma_\mu\sigma^i\psi_1(x) \quad (2.18)$$

583 while the weak hypercharge conserved current resulting from the $U(1)_Y$ symmetry is
584 given by

$$J_\mu^Y = \sum_{j=1}^3 \bar{\psi}_j(x)\gamma_\mu y_j\psi_j(x) \quad (2.19)$$

585 In order to evaluate the electroweak interactions modeled by an isos triplet field W_μ^i
586 which couples to isospin currents J_μ^i with strength g and additionally the singlet
587 field B_μ which couples to the weak hypercharge current J_μ^Y with strength $g'/2$. The
588 interaction Lagrangian density to be considered is

$$\mathcal{L}_I = -g J^{i\mu}(x) W_\mu^i(x) - \frac{g'}{2} J^{Y\mu}(x) B_\mu(x) \quad (2.20)$$

589 Note that the weak isospin currents are not the same as the charged fermionic currents
 590 that were used to describe the WI (eqn 2.7), since the weak isospin eigenstates are
 591 not the same as the mass eigenstates, but they are closely related

$$J_\mu = \frac{1}{2}(J_\mu^1 + iJ_\mu^2), \quad J_\mu^\dagger = \frac{1}{2}(J_\mu^1 - iJ_\mu^2). \quad (2.21)$$

592 The same happens with the gauge fields W_μ^i which are related to the mass eigenstates
 593 W^\pm by

$$W_\mu^+ = \frac{1}{\sqrt{2}}(W_\mu^1 - iW_\mu^2), \quad W_\mu^- = \frac{1}{\sqrt{2}}(W_\mu^1 + iW_\mu^2). \quad (2.22)$$

594 The fact that there are three weak isospin conserved currents is an indication that in
 595 addition to the charged fermionic currents, which couple charged to neutral leptons,
 596 there should be a neutral fermionic current that does not involve electric charge
 597 exchange; therefore, it couples neutral fermions or fermions of the same electric charge.
 598 The third weak isospin current contains a term that is similar to the electromagnetic
 599 current (j_μ^{em}), indicating that there is a relation between them and resembling the
 600 Gell-Mann-Nishijima formula 2.2 adapted to electroweak interactions

$$Q = T_3 + \frac{Y_W}{2}. \quad (2.23)$$

601 Just as Q generates the $U(1)_{em}$ symmetry, the weak hypercharge generates the $U(1)_Y$
 602 symmetry as said before. It is possible to write the relationship in terms of the currents
 603 as

$$j_\mu^{em} = J_\mu^3 + \frac{1}{2} J_\mu^Y. \quad (2.24)$$

604 The neutral gauge fields W_μ^3 and B_μ cannot be directly identified with the Z and the
 605 photon fields since the photon interacts similarly with left and right-handed fermions;
 606 however, they are related through a linear combination given by

$$\begin{aligned} A_\mu &= B_\mu \cos \theta_W + W_\mu^3 \sin \theta_W \\ Z_\mu &= -B_\mu \sin \theta_W + W_\mu^3 \cos \theta_W \end{aligned} \quad (2.25)$$

607 where θ_W is known as the “Weinberg angle.” The interaction Lagrangian is now given
 608 by

$$\mathcal{L}_I = -\frac{g}{\sqrt{2}}(J^\mu W_\mu^+ + J^{\mu\dagger} W_\mu^-) - \left(g \sin \theta_W J_\mu^3 + g' \cos \theta_W \frac{J_\mu^Y}{2}\right) A^\mu - \left(g \cos \theta_W J_\mu^3 - g' \sin \theta_W \frac{J_\mu^Y}{2}\right) Z^\mu \quad (2.26)$$

609 the first term is the weak charged current interaction, while the second term is the
 610 electromagnetic interaction under the condition

$$g \sin \theta_W = g' \cos \theta_W = e, \quad \frac{g'}{g} = \tan \theta_W \quad (2.27)$$

611 contained in the eqn.2.24; the third term is the neutral weak current.

612

613 Note that the neutral fields transformation given by the eqn. 2.25 can be written in
 614 terms of the coupling constants g and g' as:

$$A_\mu = \frac{g' W_\mu^3 + g B_\mu}{\sqrt{g^2 + g'^2}}, \quad Z_\mu = \frac{g W_\mu^3 - g' B_\mu}{\sqrt{g^2 + g'^2}} \quad (2.28)$$

615 So far, the Lagrangian density describing the non-massive EWI is:

$$\mathcal{L}_{nmEWI} = \mathcal{L}_0 + \mathcal{L}_G \quad (2.29)$$

616 where fermion and gauge fields have been considered massless because their regular
 617 mass terms are manifestly non invariant under G transformations; therefore, masses
 618 have to be generated in a gauge invariant way. The mechanism by which this goal is
 619 achieved is known as the “Higgs mechanism” and is closely connected to the concept
 620 of “spontaneous symmetry breaking.”

621 2.3.1 Spontaneous symmetry breaking (SSB)

622 Figure 2.6 left shows a steel nail (top) which is subject to an external force; the form
 623 of the potential energy is also shown (bottom).

624

625 Before reaching the critical force value, the system has rotational symmetry with re-
 626 spect to the nail axis; however, after the critical force value is reached the nail buckles
 627 (top right). The form of the potential energy (bottom right) changes, preserving its
 628 rotational symmetry although its minima does not exhibit that rotational symmetry
 629 any longer. Right before the nail buckles there is no indication of the direction the
 630 nail will bend because any of the directions are equivalent, but once the nail bends,
 631 choosing a direction, an arbitrary minimal energy state (ground state) is selected and
 632 it does not share the system’s rotational symmetry. This mechanism for reaching an
 633 asymmetric ground state is known as “*spontaneous symmetry breaking*”.

634 The lesson from this analysis is that the way to introduce the SSB mechanism into a
 635 system is by adding the appropriate potential to it.

636

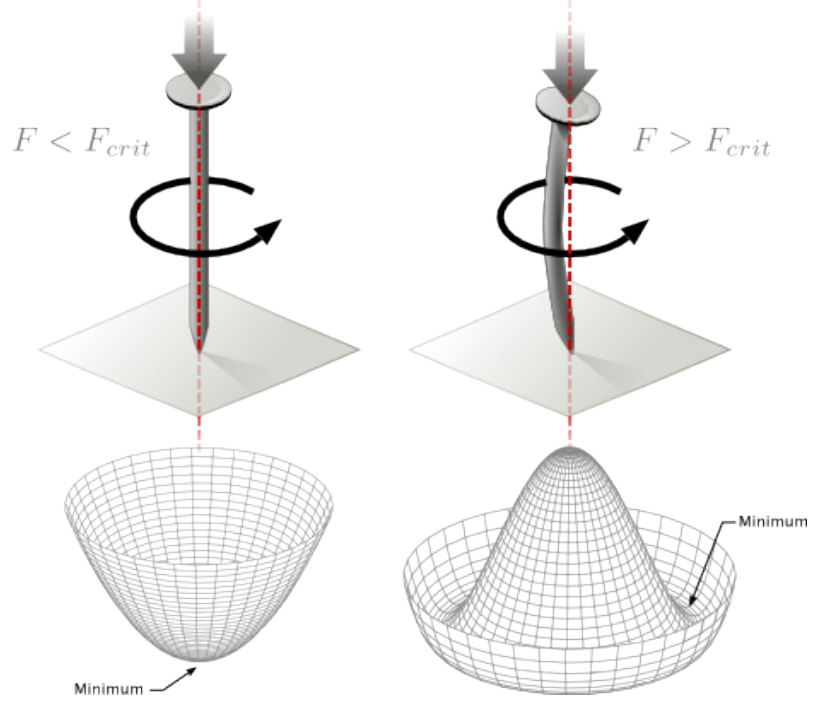


Figure 2.6: Spontaneous symmetry breaking mechanism. The steel nail, subject to an external force (top left), has rotational symmetry with respect to its axis. When the external force overcomes a critical value the nail buckles (top right) choosing a minimal energy state (ground state) and thus “*breaking spontaneously the rotational symmetry*”. The potential energy (bottom) changes but holds the rotational symmetry; however, an infinite number of asymmetric ground states are generated and circularly distributed in the bottom of the potential [27].

637 Figure 2.7 shows a plot of the potential $V(\phi)$ in the case of a scalar field ϕ

$$V(\phi) = \mu^2 \phi^\dagger \phi + \lambda (\phi^\dagger \phi)^2 \quad (2.30)$$

638 If $\mu^2 > 0$ the potential has only one minimum at $\phi = 0$ and describes a scalar field
 639 with mass μ . If $\mu^2 < 0$ the potential has a local maximum at $\phi = 0$ and two minima
 640 at $\phi = \pm\sqrt{-\mu^2/\lambda}$ which enables the SSB mechanism to work.

641

642 In the case of a complex scalar field $\phi(x)$

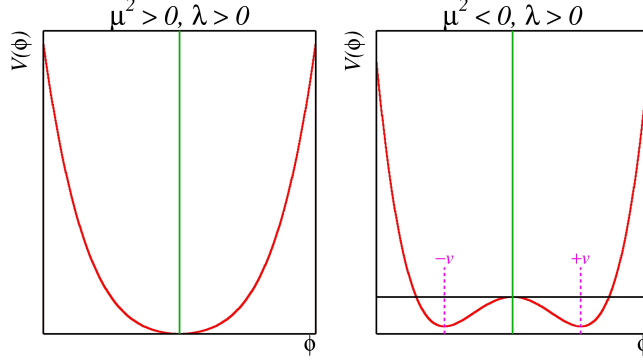


Figure 2.7: Shape of the potential $V(\phi)$ for $\lambda > 0$ and: $\mu^2 > 0$ (left) and $\mu^2 < 0$ (right). The case $\mu^2 < 0$ corresponds to the potential suitable for introducing the SSB mechanism by choosing one of the two ground states which are connected via reflection symmetry. [27].

$$\phi(x) = \frac{1}{\sqrt{2}}(\phi_1 + i\phi_2) \quad (2.31)$$

643 the Lagrangian (invariant under global $U(1)$ transformations) is given by

$$\mathcal{L} = (\partial_\mu \phi)^\dagger (\partial^\mu \phi) - V(\phi), \quad V(\phi) = \mu^2 \phi^\dagger \phi + \lambda (\phi^\dagger \phi)^2 \quad (2.32)$$

644 where an appropriate potential has been added in order to introduce the SSB.

645

646 As seen in figure 2.8, the potential has now an infinite number of minima circularly
 647 distributed along the ξ -direction which makes possible the occurrence of the SSB by
 648 choosing an arbitrary ground state; for instance, $\xi = 0$, i.e. $\phi_1 = v, \phi_2 = 0$

$$\phi_0 = \frac{v}{\sqrt{2}} \exp(i\xi) \xrightarrow{\text{SSB}} \phi_0 = \frac{v}{\sqrt{2}} \quad (2.33)$$

649 As usual, excitations over the ground state are studied by making an expansion about

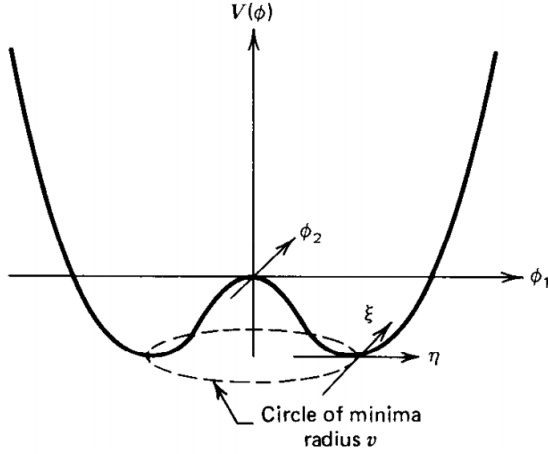


Figure 2.8: Potential for complex scalar field. There is a circle of minima of radius v along the ξ -direction [6].

650 it; thus, the excitation can be parametrized as:

$$\phi(x) = \frac{1}{\sqrt{2}}(v + \eta(x) + i\xi(x)) \quad (2.34)$$

651 which when substituted into eqn. 2.32 produces a Lagrangian in terms of the new
652 fields η and ξ

$$\mathcal{L}' = \frac{1}{2}(\partial_\mu \xi)^2 + \frac{1}{2}(\partial_\mu \eta)^2 + \mu^2 \eta^2 - V(\phi_0) - \lambda v \eta (\eta^2 + \xi^2) - \frac{\lambda}{4}(\eta^2 + \xi^2)^2 \quad (2.35)$$

653 where the last two terms represent the interactions and self-interaction between the
654 two fields η and ξ . The particular feature of the SSB mechanism is revealed when
655 looking to the first three terms of \mathcal{L}' . Before the SSB, only the massless ϕ field is
656 present in the system; after the SSB there are two fields of which the η -field has
657 acquired mass $m_\eta = \sqrt{-2\mu^2}$ while the ξ -field is still massless (see figure 2.9).

658

659 Thus, the SSB mechanism serves as a method to generate mass but as a side effect a

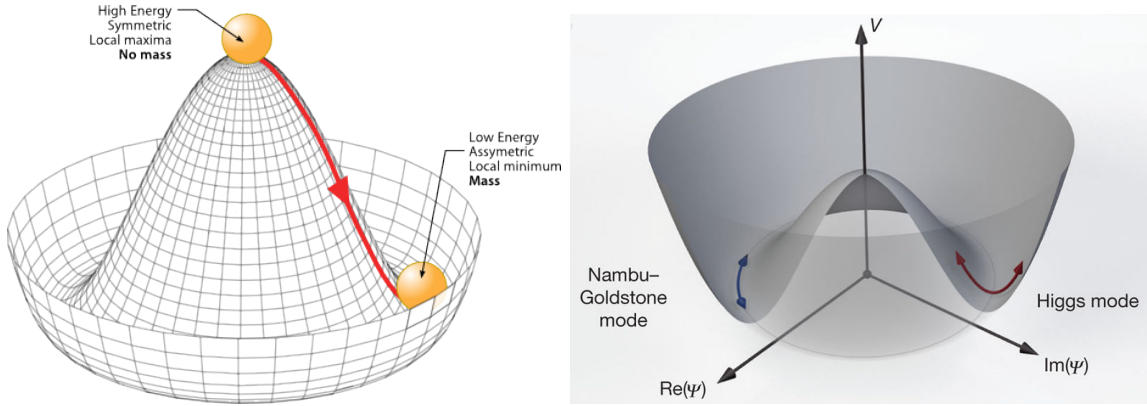


Figure 2.9: SSB mechanism for a complex scalar field [27, 28].

660 *massless field is introduced in the system.* This fact is known as the Goldstone theorem
 661 and states that a massless scalar field appears in the system for each continuous
 662 symmetry spontaneously broken. Another version of the Goldstone theorem states
 663 that “*if a Lagrangian is invariant under a continuous symmetry group G , but the*
 664 *vacuum is only invariant under a subgroup $H \subset G$, then there must exist as many*
 665 *massless spin-0 particles (Nambu-Goldstone bosons) as broken generators.*” [26] The
 666 Nambu-Goldstone boson can be understood considering that the potential in the ξ -
 667 direction is flat so excitations in that direction are not energy consuming and thus
 668 represent a massless state.

669 2.3.2 Higgs mechanism

670 When the SSB mechanism is introduced in the formulation of the EWI in an attempt
 671 to generate the mass of the so far massless gauge bosons and fermions, an interesting
 672 effect is revealed. In order to keep the G symmetry group invariance and generate
 673 the mass of the EW gauge bosons, a G invariant Lagrangian density (\mathcal{L}_S) has to be
 674 added to the non massive EWI Lagrangian (eqn. 2.29)

$$\mathcal{L}_S = (D_\mu \phi)^\dagger (D^\mu \phi) - \mu^2 \phi^\dagger \phi - \lambda (\phi^\dagger \phi)^2, \quad \lambda > 0, \mu^2 < 0 \quad (2.36)$$

$$D_\mu \phi = \left(i\partial_\mu - g \frac{\sigma_i}{2} W_\mu^i - g' \frac{Y}{2} B_\mu \right) \phi \quad (2.37)$$

675 ϕ has to be an isospin doublet of complex scalar fields so it preserves the G invariance;

676 thus ϕ can be defined as:

$$\phi = \begin{pmatrix} \phi^+ \\ \phi^0 \end{pmatrix} \equiv \frac{1}{\sqrt{2}} \begin{pmatrix} \phi_1 + i\phi_2 \\ \phi_3 + i\phi_4 \end{pmatrix}. \quad (2.38)$$

677 The minima of the potential are defined by

$$\phi^\dagger \phi = \frac{1}{2} (\phi_1^2 + \phi_2^2 + \phi_3^2 + \phi_4^2) = -\frac{\mu^2}{2\lambda}. \quad (2.39)$$

678 The choice of the ground state is critical. By choosing a ground state, invariant under

679 $U(1)_{em}$ gauge symmetry, the photon will remain massless and the W^\pm and Z bosons

680 masses will be generated which is exactly what is needed. In that sense, the best

681 choice corresponds to a weak isospin doublet with $T_3 = -1/2$, $Y_W = 1$ and $Q = 0$

682 which defines a ground state with $\phi_1 = \phi_2 = \phi_4$ and $\phi_3 = v$:

$$\phi_0 \equiv \frac{1}{\sqrt{2}} \begin{pmatrix} 0 \\ v \end{pmatrix}, \quad v^2 \equiv -\frac{\mu^2}{\lambda}. \quad (2.40)$$

683 where the vacuum expectation value v is fixed by the Fermi coupling G_F according

684 to $v = (\sqrt{2}G_F)^{1/2} \approx 246$ GeV.

685

686 The G symmetry has been broken and three Nambu-Goldstone bosons will appear.

687 The next step is to expand ϕ about the chosen ground state as:

$$\phi(x) = \frac{1}{\sqrt{2}} \exp\left(\frac{i}{v} \sigma_i \theta^i(x)\right) \begin{pmatrix} 0 \\ v + H(x) \end{pmatrix} \approx \frac{1}{\sqrt{2}} \begin{pmatrix} \theta_1(x) + i\theta_2(x) \\ v + H(x) - i\theta_3(x) \end{pmatrix} \quad (2.41)$$

688 to describe fluctuations from the ground state ϕ_0 . The fields $\theta_i(x)$ represent the
 689 Nambu-Goldstone bosons while $H(x)$ is known as “higgs field.” The fundamental
 690 feature of the parametrization used is that the dependence on the $\theta_i(x)$ fields is
 691 factored out in a global phase that can be eliminated by taking the physical “unitary
 692 gauge” $\theta_i(x) = 0$. Therefore the expansion about the ground state is given by:

$$\phi(x) \frac{1}{\sqrt{2}} \begin{pmatrix} 0 \\ v + H(x) \end{pmatrix} \quad (2.42)$$

693 which when substituted into \mathcal{L}_S (eqn. 2.36) results in a Lagrangian containing the now
 694 massive three gauge bosons W^\pm, Z , one massless gauge boson (photon) and the new
 695 Higgs field (H). The three degrees of freedom corresponding to the Nambu-Goldstone
 696 bosons are now integrated into the massive gauge bosons as their longitudinal po-
 697 larizations which were not available when they were massless particles. The effect
 698 by which vector boson fields acquire mass after an spontaneous symmetry breaking,
 699 but without an explicit gauge invariance breaking is known as the “*Higgs mechanism*”.

700

701 The mechanism was proposed by three independent groups: F.Englert and R.Brout
 702 in August 1964 [29], P.Higgs in October 1964 [30] and G.Guralnik, C.Hagen and
 703 T.Kibble in November 1964 [31]; however, its importance was not realized until
 704 S.Glashow [22], A.Salam [23] and S.Weinberg [24], independently, proposed that elec-
 705 tromagnetic and weak interactions are two manifestations of a more general interac-
 706 tion called “electroweak interaction” in 1967.

707 **2.3.3 Masses of the gauge bosons**

708 The mass of the gauge bosons is extracted by evaluating the kinetic part of Lagrangian

709 \mathcal{L}_S in the ground state (known also as the vacuum expectation value), i.e.,

$$\left| \left(\partial_\mu - ig \frac{\sigma_i}{2} W_\mu^i - i \frac{g'}{2} B_\mu \right) \phi_0 \right|^2 = \left(\frac{1}{2} v g \right)^2 W_\mu^+ W^{-\mu} + \frac{1}{8} v^2 (W_\mu^3, B_\mu) \begin{pmatrix} g^2 & -gg' \\ -gg' & g'^2 \end{pmatrix} \begin{pmatrix} W^{3\mu} \\ B^\mu \end{pmatrix} \quad (2.43)$$

710 comparing with the typical mass term for a charged boson $M_W^2 W^+ W^-$

$$M_W = \frac{1}{2} v g. \quad (2.44)$$

The second term in the right side of the eqn.2.43 comprises the masses of the neutral bosons, but it needs to be written in terms of the gauge fields Z_μ and A_μ in order to be compared to the typical mass terms for neutral bosons, therefore using eqn. 2.28

$$\begin{aligned} \frac{1}{8} v^2 [g^2 (W_\mu^3)^2 - 2gg' W_\mu^3 B^\mu + g'^2 B_\mu^2] &= \frac{1}{8} v^2 [g W_\mu^3 - g' B_\mu]^2 + 0[g' W_\mu^3 + g B_\mu]^2 \quad (2.45) \\ &= \frac{1}{8} v^2 [\sqrt{g^2 + g'^2} Z_\mu]^2 + 0[\sqrt{g^2 + g'^2} A_\mu]^2 \end{aligned}$$

711 and then

$$M_Z = \frac{1}{2} v \sqrt{g^2 + g'^2}, \quad M_A = 0 \quad (2.46)$$

712 2.3.4 Masses of the fermions

713 The lepton mass terms can be generated by introducing a gauge invariant Lagrangian
 714 term describing the Yukawa coupling between the lepton field and the Higgs field

$$\mathcal{L}_{Yl} = -G_l \left[(\bar{\nu}_l, \bar{l})_L \begin{pmatrix} \phi^+ \\ \phi^0 \end{pmatrix} l_R + \bar{l}_R (\phi^-, \bar{\phi}^0) \begin{pmatrix} \nu_l \\ l \end{pmatrix}_L \right], \quad l = e, \mu, \tau. \quad (2.47)$$

715 After the SSB and replacing the usual field expansion about the ground state (eqn.2.40)
 716 into \mathcal{L}_{Yl} , the mass term arises

$$\mathcal{L}_{Yl} = -m_l (\bar{l}_L l_R + \bar{l}_R l_L) - \frac{m_l}{v} (\bar{l}_L l_R + \bar{l}_R l_L) H = -m_l \bar{l} l \left(1 + \frac{H}{v} \right) \quad (2.48)$$

717

$$m_l = \frac{G_l}{\sqrt{2}} v \quad (2.49)$$

718 where the additional term represents the lepton-Higgs interaction. The quark masses
 719 are generated in a similar way as lepton masses but for the upper member of the
 720 quark doublet a different Higgs doublet is needed:

$$\phi_c = -i\sigma_2 \phi^* = \begin{pmatrix} -\bar{\phi}^0 \\ \phi^- \end{pmatrix}. \quad (2.50)$$

721 Additionally, given that the quark isospin doublets are not constructed in terms of
 722 the mass eigenstates but in terms of the flavor eigenstates, as shown in table2.5, the
 723 coupling parameters will be related to the CKM matrix elements; thus the quark
 724 Lagrangian is given by:

$$\mathcal{L}_{Yq} = -G_d^{i,j} (\bar{u}_i, \bar{d}'_i)_L \begin{pmatrix} \phi^+ \\ \phi^0 \end{pmatrix} d_{jR} - G_u^{i,j} (\bar{u}_i, \bar{d}'_i)_L \begin{pmatrix} -\bar{\phi}^0 \\ \phi^- \end{pmatrix} u_{jR} + h.c. \quad (2.51)$$

725 with $i,j=1,2,3$. After SSB and expansion about the ground state, the diagonal form

726 of \mathcal{L}_{Yq} is:

$$\mathcal{L}_{Yq} = -m_d^i \bar{d}_i d_i \left(1 + \frac{H}{v}\right) - m_u^i \bar{u}_i u_i \left(1 + \frac{H}{v}\right) \quad (2.52)$$

727 Fermion masses depend on arbitrary couplings G_l and $G_{u,d}$ and are not predicted by
728 the theory.

729 2.3.5 The Higgs field

730 After the characterization of the fermions and gauge bosons as well as their interac-
731 tions, it is necessary to characterize the Higgs field itself. The Lagrangian \mathcal{L}_S in eqn.
732 2.36 written in terms of the gauge bosons is given by

$$\mathcal{L}_S = \frac{1}{4} \lambda v^4 + \mathcal{L}_H + \mathcal{L}_{HV} \quad (2.53)$$

733

$$\mathcal{L}_H = \frac{1}{2} \partial_\mu H \partial^\mu H - \frac{1}{2} m_H^2 H^2 - \frac{1}{2v} m_H^2 H^3 - \frac{1}{8v^2} m_H^2 H^4 \quad (2.54)$$

734

$$\mathcal{L}_{HV} = m_H^2 W_\mu^+ W^{\mu-} \left(1 + \frac{2}{v} H + \frac{2}{v^2} H^2\right) + \frac{1}{2} m_Z^2 Z_\mu Z^\mu \left(1 + \frac{2}{v} H + \frac{2}{v^2} H^2\right) \quad (2.55)$$

735 The mass of the Higgs boson is deduced as usual from the mass term in the Lagrangian
736 resulting in:

$$m_H = \sqrt{-2\mu^2} = \sqrt{2\lambda}v \quad (2.56)$$

737 however, it is not predicted by the theory either. The experimental efforts to find
738 the Higgs boson, carried out by the “Compact Muon Solenoid (CMS)” experiment
739 and the “A Toroidal LHC AppartuS (ATLAS)” experiments at the “Large Hadron
740 Collider(LHC)”, gave great results by July of 2012 when the discovery of a new
741 particle compatible with the Higgs boson predicted by the electroweak theory [32, 33]
742 was announced. Although at the announcement time there were some reservations
743 about calling the new particle the “Higgs boson”, today this name is widely accepted.

744 The Higgs mass measurement, reported by both experiments [34], is in table 2.8.

Property	Value
Electric charge	0
Colour charge	0
Spin	0
Weak isospin	-1/2
Weak hypercharge	1
Parity	1
Mass (GeV/c^2)	$125.09 \pm 0.21 \text{ (stat.)} \pm 0.11 \text{ (syst.)}$

Table 2.8: Higgs boson properties. Higgs mass is not predicted by the theory and the value here corresponds to the experimental measurement.

745

746 2.3.6 Production of Higgs bosons at LHC

747 At LHC, Higgs boson is produced as a result of the collision of two counter-rotating
 748 protons beams. A detailed description of the LHC machine will be presented in
 749 chapter 3. “The total cross section” is a parameter that quantifies the number of pp
 750 collisions that happen when a number of protons are fired at each other. Different
 751 results can be obtained after a pp collision and for each one the “cross section” is
 752 defined as the number of pp collisions that conclude in that particular result with
 753 respect to the number of protons fired at each other.

754 Protons are composed of quarks and these quarks are bound by gluons; however,
 755 what is commonly called the quark content of the proton makes reference to the
 756 valence quarks. A sea of quarks and gluons is also present inside the proton as repre-
 757 sented in figure 2.10. In a proton-proton (pp) collision, the constituents (quarks and
 758 gluons) are those who collide. The pp cross section depends on the momentum of
 759 the colliding particles, reason for which it is needed to know how the momentum is
 760 distributed inside the proton. Quarks and gluons are known as partons and the func-
 761 tions that describe how the proton momentum is distributed among partons inside it

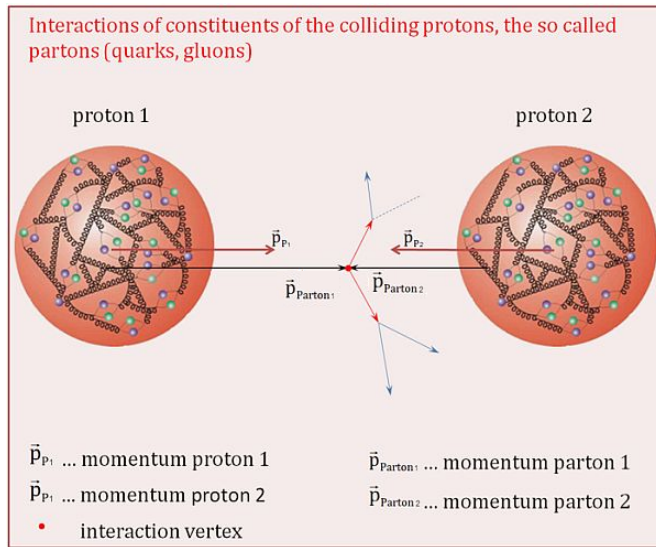


Figure 2.10: Proton-proton collision. Protons are composed of 3 valence quarks, a sea of quarks and gluons; therefore in a proton-proton collision, quarks and gluons are those who collide. [35].

are called “parton distribution functions (PDFs)”; PDFs are determined from experimental data obtained in experiments where the internal structure of hadrons is tested.

764

In addition, in physics, a common approach to study complex systems consists in starting with a simpler version of them, for which a well known description is available, and add an additional “perturbation” which represents a small deviation from the known behavior. If the perturbation is small enough, the physical quantities associated with the perturbed system are expressed as a series of corrections to those of the simpler system; therefore, the more terms are considered in the series (the higher order in the perturbation series), the more precise is the the description of the complex system.

773

774 This thesis explores the Higgs production at LHC; therefore the overview presented
775 here will be oriented specifically to the production mechanisms after pp collisions at

776 LHC.

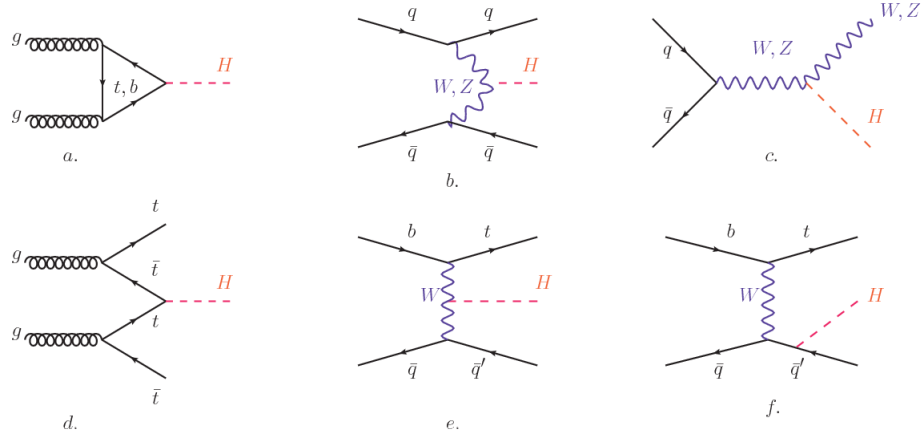


Figure 2.11: Main Higgs boson production mechanism Feynman diagrams. a. gluon-gluon fusion, b. vector boson fusion (VBF), c. Higgs-strahlung, d. Associated production with a top or bottom quark pair, e-f. associated production with a single top quark.

777 Figure 2.11 shows the Feynman diagrams for the leading order (first order) Higgs
778 production processes at LHC, while the cross section for Higgs production as a func-

779 tion of the center of mass-energy (\sqrt{s}) for pp collisions is showed in figure 2.12 left.

780 The tags NLO (next to leading order), NNLO (next to next to leading order) and

781 N3LO (next to next to next to leading order) make reference to the order at which

782 the perturbation series have been considered.

783 As shown in eqns 2.47, 2.51 and 2.55, the strength of the Higgs-fermion interaction

784 is proportional to the fermion mass while the strength of the Higgs-gauge boson

785 interaction is proportional to the square of the gauge boson mass, which implies

786 that the Higgs production and decay mechanisms are dominated by couplings $H -$

787 (W, Z, t, b, τ) .

788 The main production mechanism is the gluon fusion (figure 2.11a and $pp \rightarrow H$ in figure

789 2.12) given that gluons carry the highest fraction of momentum of the protons in pp

790 colliders. Since the Higgs boson does not couple to gluons, the mechanism proceeds

791 through the exchange of a virtual top-quark loop given that for it the coupling is

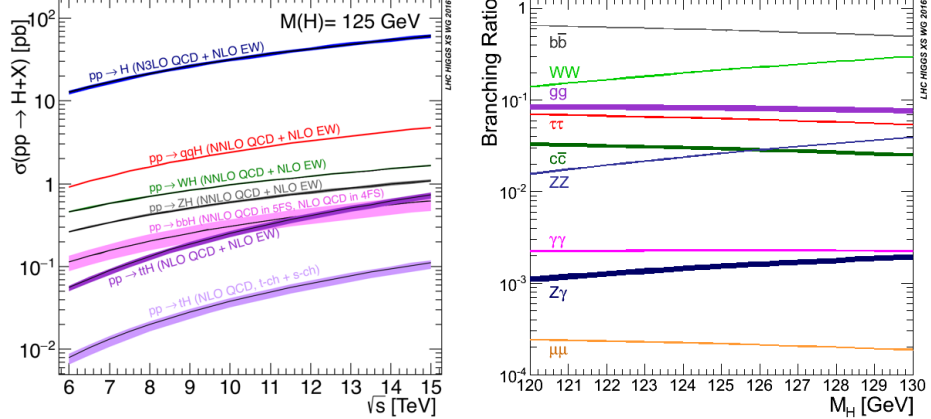


Figure 2.12: Higgs boson production cross sections (left) and decay branching ratios (right) for the main mechanisms. The VBF is indicated as qqH [36].

the biggest. Note that in this process, the Higgs boson is produced alone, which makes this mechanism experimentally clean when combined with the two-photon or the four-lepton decay channels (see section 2.3.7).

Vector boson fusion (figure 2.11b and $pp \rightarrow qqH$ in figure 2.12) has the second largest production cross section. The scattering of two fermions is mediated by a weak gauge boson which later emits a Higgs boson. In the final state, the two fermions tend to be located in a particular region of the detector which is used as a signature when analyzing the datasets provided by the experiments. More details about how to identify events of interest in an analysis will be given in chapter 6.

The next production mechanism is Higgs-strahlung (figure 2.11c and $pp \rightarrow WH, pp \rightarrow ZH$ in figure 2.12) where two fermions annihilate to form a weak gauge boson. If the initial fermions have enough energy, the emergent boson eventually will emit a Higgs boson.

The associated production with a top or bottom quark pair and the associated production with a single top quark (figure 2.11d-f and $pp \rightarrow bbH, pp \rightarrow t\bar{t}H, pp \rightarrow tH$ in figure 2.12) have a smaller cross section than the main three mechanisms above,

808 but they provide a good opportunity to test the Higgs-top coupling. The analysis
 809 reported in this thesis is developed using these production mechanisms. A detailed
 810 description of the tH mechanism will be given in section 2.4.

811 2.3.7 Higgs boson decay channels

812 When a particle can decay through several modes, also known as channels, the
 813 probability of decaying through a given channel is quantified by the “branching ratio
 814 (BR)” of the decay channel; thus, the BR is defined as the ratio of number of decays
 815 going through that given channel to the total number of decays. In regard to the
 816 Higgs boson decay, the BR can be predicted with accuracy once the Higgs mass is
 817 known [37, 38]. In figure 2.12 right, a plot of the BR as a function of the Higgs mass
 818 is presented. The largest predicted BR corresponds to the $b\bar{b}$ pair decay channel (see
 819 table 2.9).

Decay channel	Branching ratio	Rel. uncertainty
$H \rightarrow b\bar{b}$	5.84×10^{-1}	$+3.2\% - 3.3\%$
$H \rightarrow W^+W^-$	2.14×10^{-1}	$+4.3\% - 4.2\%$
$H \rightarrow \tau^+\tau^-$	6.27×10^{-2}	$+5.7\% - 5.7\%$
$H \rightarrow ZZ$	2.62×10^{-2}	$+4.3\% - 4.1\%$
$H \rightarrow \gamma\gamma$	2.27×10^{-3}	$+5.0\% - 4.9\%$
$H \rightarrow Z\gamma$	1.53×10^{-3}	$+9.0\% - 8.9\%$
$H \rightarrow \mu^+\mu^-$	2.18×10^{-4}	$+6.0\% - 5.9\%$

Table 2.9: Predicted branching ratios and the relative uncertainty for a SM Higgs boson with $m_H = 125 GeV/c^2$. [9]

821 **2.4 Associated production of a Higgs boson and a
822 single Top quark.**

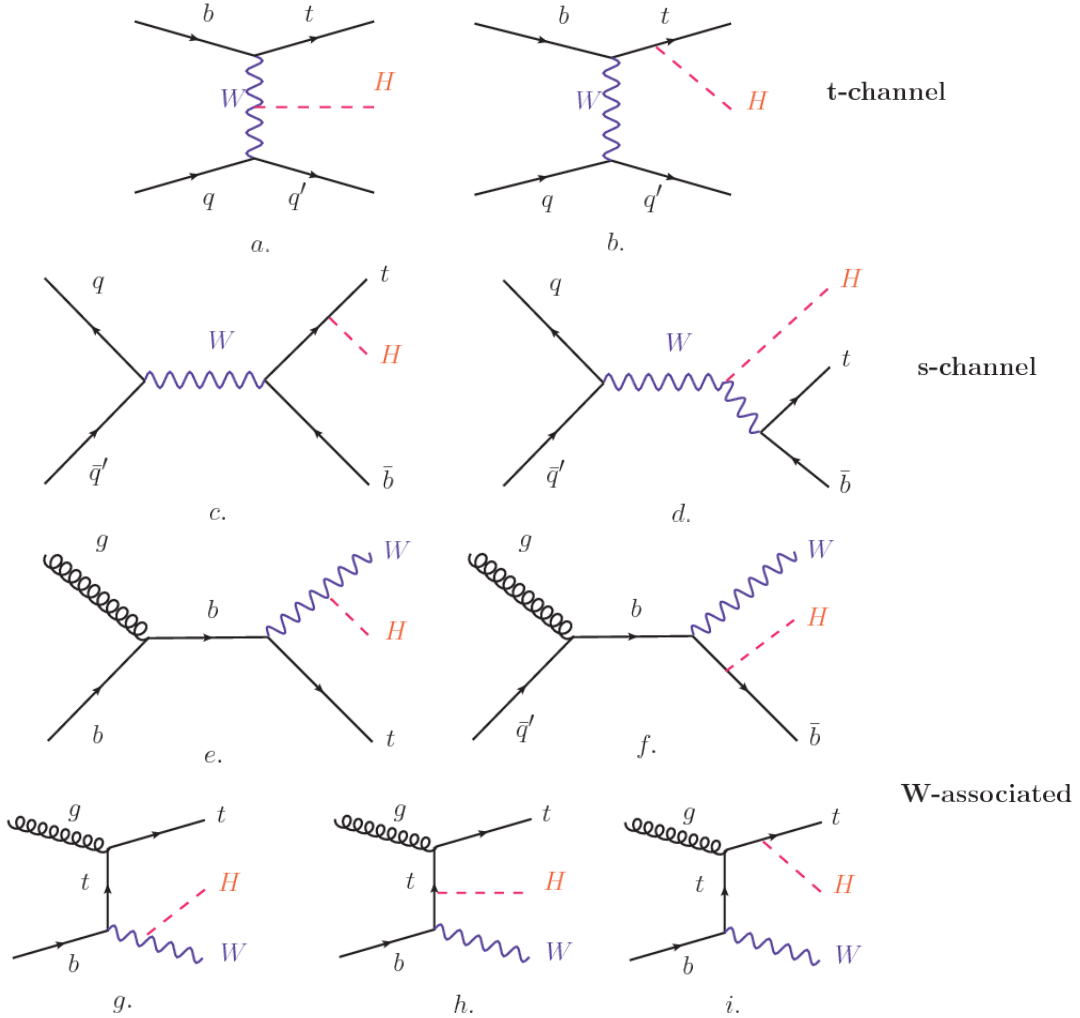


Figure 2.13: Associated Higgs boson production mechanism Feynman diagrams. a.,b. t-channel (tHq), c.,d. s-channel (tHb), e-i. W-associated.

823 Associated production of Higgs boson has been extensively studied [39–43]. While
824 measurements of the main Higgs production mechanisms rates are sensitive to the
825 strength of the Higgs coupling to W boson or top quark, they are not sensitive to the
826 relative sign between the two couplings. In this thesis, the Higgs boson production

mechanism explored is the associated production with a single top quark (*th*) which offers sensitiveness to the relative sign of the Higgs couplings to W boson and to top quark. The description given here is based on the reference [41]

830

831 A process where two incoming particles interact and produce a final state with two
 832 particles can proceed in three ways also called channels (see, for instance, figure 2.13
 833 ommiting the red line). The t-channel represents processes where an intermediate
 834 particle is emitted by one of the incoming particles and absorbed by the other. The
 835 s-channel represents processes where the two incoming particles merge into an inter-
 836 mediate particle which eventually will split into the particles in the final state. The
 837 third channel, u-channel, is similar to the t-channel but the two outgoing particles
 838 interchange their roles.

839

840 The *th* production, where Higgs boson can be radiated either from the top quark or
 841 from the W boson, is represented by the leading order Feynman diagrams in figure
 842 2.13. The cross section for the *th* process is calculated, as usual, summing over
 843 the contributions from the different feynman diagrams; therefore it depends on the
 844 interference between the contributions. In the SM, the interference for t-channel (tHq
 845 process) and W-associated (tHW process) production is destructive [39] resulting in
 846 the small cross sections presented in table 2.10.

tH production channel	Cross section (fb)
t-channel ($pp \rightarrow tHq$)	$70.79^{+2.99}_{-4.80}$
W-associated ($pp \rightarrow tHW$)	$15.61^{+0.83}_{-1.04}$
s-channel($pp \rightarrow tHb$)	$2.87^{+0.09}_{-0.08}$

Table 2.10: Predicted SM cross sections for *tH* production at $\sqrt{s} = 13$ TeV [44, 45].

847

848 While the s-channel contribution can be neglected, it will be shown that a deviation
 849 from the SM destructive interference would result in an enhancement of the th cross
 850 section compared to that in SM, which could be used to get information about the
 851 sign of the Higgs-top coupling [41, 42]. In order to describe th production processes,
 852 Feynman diagram 2.13b will be considered; there, the W boson is radiated by a
 853 quark in the proton and eventually it will interact with the b quark. In the high
 854 energy regime, the effective W approximation [46] allows to describe the process as
 855 the emmision of an approximately on-shell W and its hard scattering with the b
 856 quark; i.e. $Wb \rightarrow th$. The scattering amplitude for the process is given by

$$\mathcal{A} = \frac{g}{\sqrt{2}} \left[(\kappa_t - \kappa_V) \frac{m_t \sqrt{s}}{m_W v} A \left(\frac{t}{s}, \varphi; \xi_t, \xi_b \right) + \left(\kappa_V \frac{2m_W s}{v} \frac{1}{t} + (2\kappa_t - \kappa_V) \frac{m_t^2}{m_W v} \right) B \left(\frac{t}{s}, \varphi; \xi_t, \xi_b \right) \right], \quad (2.57)$$

857 where $\kappa_V \equiv g_{HVV}/g_{HVV}^{SM}$ and $\kappa_t \equiv g_{Ht}/g_{Ht}^{SM} = y_t/y_t^{SM}$ are scaling factors that quan-
 858 tify possible deviations of the couplings, Higgs-Vector boson (H-W) and Higgs-top
 859 (H-t) respectively, from the SM couplings; $s = (p_W + p_b)^2$, $t = (p_W - p_H)^2$, φ is the
 860 Higgs azimuthal angle around the z axis taken parallel to the direction of motion of
 861 the incoming W; A and B are funtions describing the weak interaction in terms of
 862 the chiral states of the quarks b and t . Terms that vanish in the high energy limit
 863 have been neglected as well as the Higgs and b quark masses⁸.

864

865 The scattering amplitude grows with energy like \sqrt{s} for $\kappa_V \neq \kappa_t$, in contrast to
 866 the SM ($\kappa_t = \kappa_V = 1$), where the first term in 2.57 cancels out and the amplitude
 867 is constant for large s ; therefore, a deviation from the SM predictions represents an
 868 enhancement in the tHq cross section. In particular, for a SM H-W coupling and a H-t

⁸ A detailed explanation of the structure and approximations used to derive \mathcal{A} can be found in reference [41]

869 coupling of inverted sign with respect to the SM ($\kappa_V = -\kappa_t = 1$) the tHq cross section
 870 is enhanced by a factor greater 10 as seen in the figure 2.14 taken from reference [41];
 871 reference [47] has reported similar enhancement results.

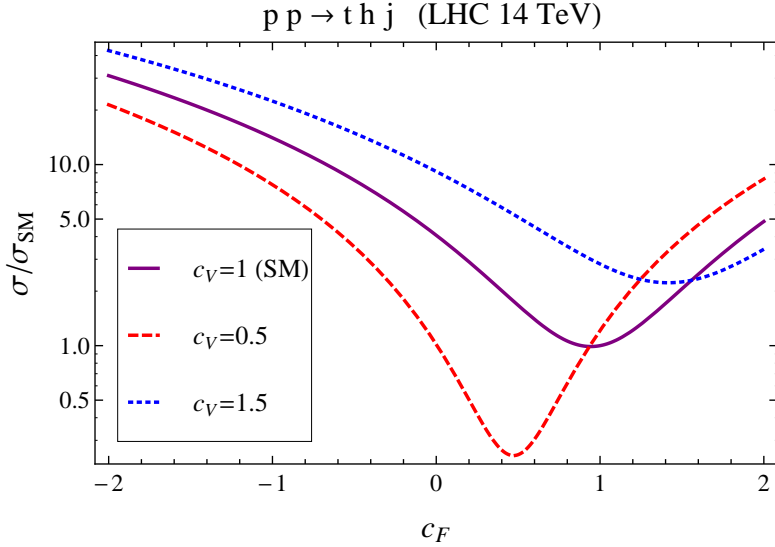


Figure 2.14: Cross section for tHq process as a function of κ_t , normalized to the SM, for three values of κ_V . In the plot c_f refers to the Higgs-fermion coupling which is dominated by the H-t coupling and represented here by κ_t . Solid, dashed and dotted lines correspond to $c_V \rightarrow \kappa_V = 1, 0.5, 1.5$ respectively. Note that for the SM ($\kappa_V = \kappa_t = 1$), the destructive effect of the interference is maximal.

872 A similar analysis is valid for the W-associated channel but, in that case, the inter-
 873 ference is more complicated since there are more than two contributions and an ad-
 874 ditional interference with the production of Higgs boson and a top pair process($t\bar{t}H$).
 875 The calculations are made using the so-called Diagram Removal (DR) technique where
 876 interfering diagrams are removed (or added) from the calculations in order to evaluate
 877 the impact of the removed contributions. DR1 was defined to neglect $t\bar{t}H$ interference
 878 while DR2 was defined to take $t\bar{t}H$ interference into account [48]. As shown in figure
 879 2.15, the tHW cross section is enhanced from about 15 fb (SM: $\kappa_{Htt} = 1$) to about
 880 150 fb ($\kappa_{Htt} = -1$). Differences between curves for DR1 and DR2 help to gauge the
 881 impact of the interference with $t\bar{t}H$.

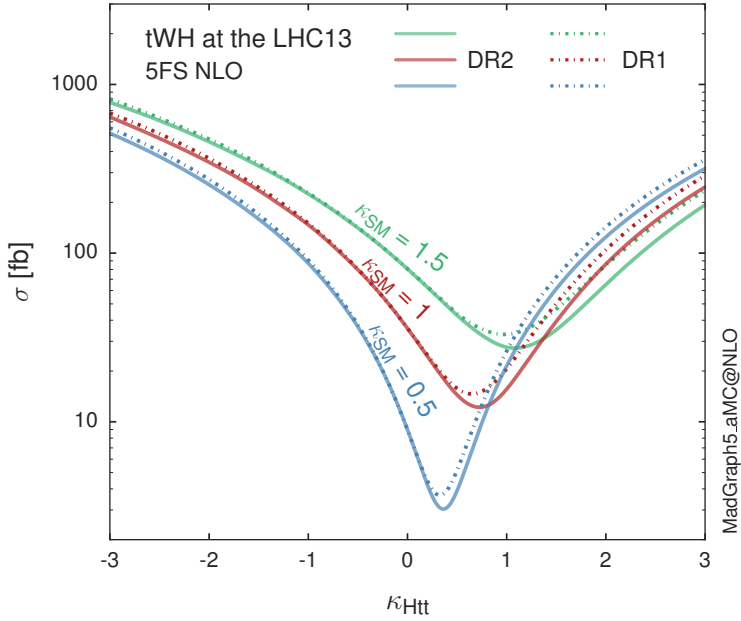


Figure 2.15: Cross section for tHW process as a function of κ_{Htt} , for three values of κ_{SM} at $\sqrt{s} = 13$ TeV. $\kappa_{Htt}^2 = \sigma_{Htt}/\sigma_{Htt}^{SM}$ is a simple rescaling of the SM Higgs interactions.

882 Results of the calculations of the tHq and tHW cross sections at $\sqrt{s} = 13$ TeV can be
 883 found in reference [49] and a summary of the results is presented in table 2.11.

884

885 2.5 The CP-mixing in tH processes

886 In addition to the sensitivity to sign of the H-t coupling, tHq and tHW processes have
 887 been proposed as a tool to investigate the possibility of a H-t coupling that does not
 888 conserve CP [43, 48, 50]. Current experimental results are consistent with SM H-V
 889 and H-t couplings; however, negative H-t coupling is not excluded completely [53].

890

891 In this thesis, the sensitivity of th processes to CP-mixing is also studied in the
 892 effective field theory framework and based in references [43, 48]; a generic particle

	\sqrt{s} TeV	$\kappa_t = 1$	$\kappa_t = -1$
$\sigma^{LO}(tHq)(fb)$ [41]	8	≈ 17.4	≈ 252.7
	14	≈ 80.4	≈ 1042
$\sigma^{NLO}(tHq)(fb)$ [41]	8	$18.28^{+0.42}_{-0.38}$	$233.8^{+4.6}_{-0.0}$
	14	$88.2^{+1.7}_{-0.0}$	$982.8^{+28}_{-0.0}$
$\sigma^{LO}(tHq)(fb)$ [47]	14	≈ 71.8	≈ 893
$\sigma^{LO}(tHW)(fb)$ [47]	14	≈ 16.0	≈ 139
$\sigma^{NLO}(tHq)(fb)$ [49]	8	$18.69^{+8.62\%}_{-17.13\%}$	-
	13	$74.25^{+7.48\%}_{-15.35\%}$	$848^{+7.37\%}_{-13.70\%}$
	14	$90.10^{+7.34\%}_{-15.13\%}$	$1011^{+7.24\%}_{-13.39\%}$
$\sigma^{LO}(tHW)(fb)$ [48]	13	$15.77^{+15.91\%}_{-15.76\%}$	-
$\sigma^{NLO}DR1(tHW)(fb)$ [48]	13	$21.72^{+6.52\%}_{-5.24\%}$	≈ 150
$\sigma^{NLO}DR2(tHW)(fb)$ [48]	13	$16.28^{+7.34\%}_{-15.13\%}$	≈ 150

Table 2.11: Predicted enhancement of the tHq and tHW cross sections at LHC for $\kappa_V = 1$ and $\kappa_t = \pm 1$ at LO and NLO; the cross section enhancement of more than a factor of 10 is due to the flippling in the sign of the H-t coupling with respect to the SM one.

893 (X_0) of spin-0 and a general CP violating interaction with the top quark, can couple
 894 to scalar and pseudoscalar fermionic densities. The H-W interaction is assumed to
 895 be SM-like. The Lagrangian modeling the H-t interaction is given by

$$\mathcal{L}_0^t = -\bar{\psi}_t (c_\alpha \kappa_{Htt} g_{Htt} + i s_\alpha \kappa_{Att} g_{Att} \gamma_5) \psi_t X_0, \quad (2.58)$$

896 where α is the CP-mixing phase, $c_\alpha \equiv \cos \alpha$ and $s_\alpha \equiv \sin \alpha$, κ_{Htt} and κ_{Att} are real
 897 dimensionless rescaling parameters⁹, $g_{Htt} = g_{Att} = m_t/v = y_t/\sqrt{2}$ and $v \sim 246$ GeV is
 898 the Higgs vacuum expectation value. In this parametrization, it is easy to recover
 899 three special cases

900 • CP-even coupling $\rightarrow \alpha = 0^\circ$

901 • CP-odd coupling $\rightarrow \alpha = 90^\circ$

902 • SM coupling $\rightarrow \alpha = 0^\circ$ and $\kappa_{Htt} = 1$

⁹ analog to κ_t and κ_V

903 The loop induced X_0 coupling to gluons can also be described in terms of the
 904 parametrization above, according to

$$\mathcal{L}_0^g = -\frac{1}{4} \left(c_\alpha \kappa_{Hgg} g_{Hgg} G_{\mu\nu}^a G^{a,\mu\nu} + s_\alpha \kappa_{Agg} g_{Agg} G_{\mu\nu}^a \tilde{G}^{a,\mu\nu} \right) X_0. \quad (2.59)$$

905 where $g_{Hgg} = -\alpha_s/3\pi v$ and $g_{Agg} = \alpha_s/2\pi v$. Under the assumption that the top quark
 906 dominates the gluon-fusion process at LHC energies, $\kappa_{Hgg} \rightarrow \kappa_{Htt}$ and $\kappa_{Agg} \rightarrow \kappa_{Att}$,
 907 so that the ratio between the gluon-gluon fusion cross section for X_0 and for the SM
 908 Higgs prediction can be written as

$$\frac{\sigma_{NLO}^{gg \rightarrow X_0}}{\sigma_{NLO,SM}^{gg \rightarrow H}} = c_\alpha^2 \kappa_{Htt}^2 + s_\alpha^2 \left(\kappa_{Att} \frac{g_{Agg}}{g_{Hgg}} \right)^2. \quad (2.60)$$

909 If the rescaling parameters are set to

$$\kappa_{Htt} = 1, \quad \kappa_{Att} = \left| \frac{g_{Hgg}}{g_{Agg}} \right| = \frac{2}{3}. \quad (2.61)$$

910 the gluon-fusion SM cross section is reproduced for every value of the CP-mixing
 911 angle α ; therefore, by imposing that condition to the Lagrangian density 2.58, the
 912 CP-mixing angle is not constrained by current data. Figure 2.16 shows the NLO cross
 913 sections for t-channel tX_0 (blue) and $t\bar{t}X_0$ (red) associated production processes as
 914 a function of the CP-mixing angle α . X_0 is a generic spin-0 particle with top quark
 915 CP-violating coupling. Rescaling factors κ_{Htt} and κ_{Att} have been set to reproduce
 916 the SM gluon-fusion cross sections.

917 It is interesting to notice that the tX_0 cross section is enhanced, by a factor of
 918 about 10, when a continuous rotation in the scalar-pseudoscalar plane is applied; this
 919 enhancement is similar to the enhancement produced when the H-t coupling is flipped
 920 in sign with respect to the SM ($y_t = -y_{t,SM}$ in the plot), as showed in section 2.4. In

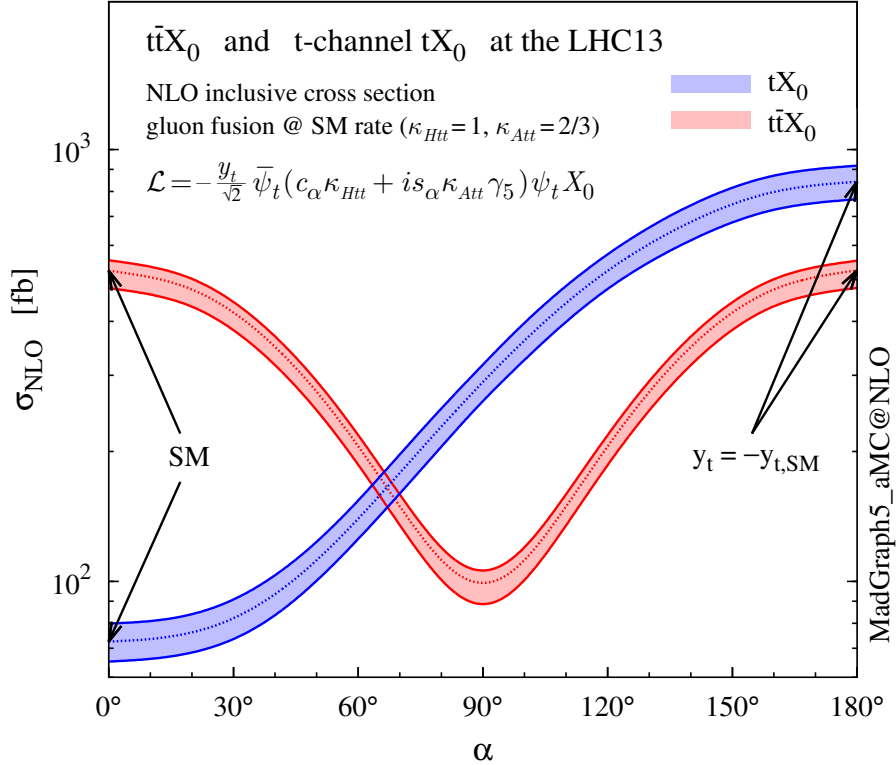


Figure 2.16: NLO cross sections for t-channel tX_0 (blue) and $t\bar{t}X_0$ (red) associated production processeses as a function of the CP-mixing angle α . X_0 is a generic spin-0 particle with top quark CP-violating coupling [43].

contrast, the degeneracy in the $t\bar{t}X_0$ cross section is still present given that it depends quadratically on the H-t coupling, but more interesting is to notice that $t\bar{t}X_0$ cross section is exceeded by tX_0 cross section after $\alpha \sim 60^\circ$.

A similar parametrization can be used to investigate the tHW process sensitivity to CP-violating H-t coupling. As said in 2.4, the interference in the W-associated channel is more complicated because there are more than two contributions and also there is interference with the $t\bar{t}H$ production process.

928

929 Figure 2.17 shows the NLO cross sections for t-channel tX_0 (blue), $t\bar{t}X_0$ (red) asso-
930 ciated production and for the combined $tWX_0 + t\bar{t}X_0 +$ interference (orange) as a

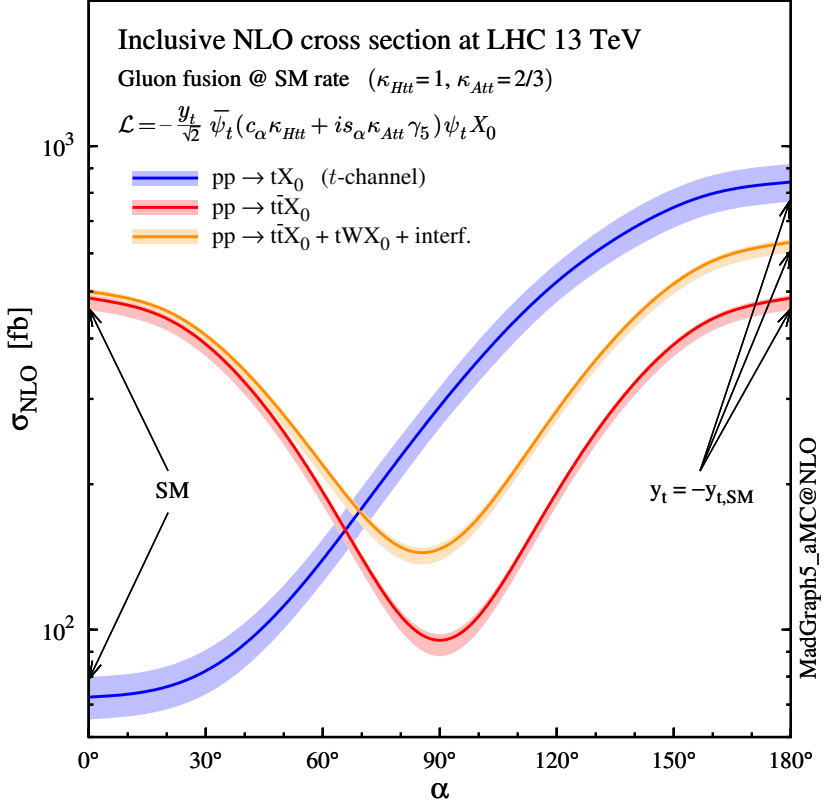


Figure 2.17: NLO cross sections for t-channel tX_0 (blue), $t\bar{t}X_0$ (red) associated production processes and combined $tWX_0 + t\bar{t}X_0$ (including interference) production as a function of the CP-mixing angle α [43].

function of the CP-mixing angle. It is clear that the effect of the interference in the combined case is the lifting of the degeneracy present in the $t\bar{t}X_0$ production. The constructive interference enhances the cross section from about 500 fb at SM ($\alpha = 0$) to about 600 fb ($\alpha = 180^\circ \rightarrow y_t = -y_{t,SM}$).
An analysis combining tHq and tHW processes will be made in this thesis taking advantage of the sensitivity improvement.

937 **2.6 Experimantal status of the anomalous**
 938 **Higg-fermion coupling.**

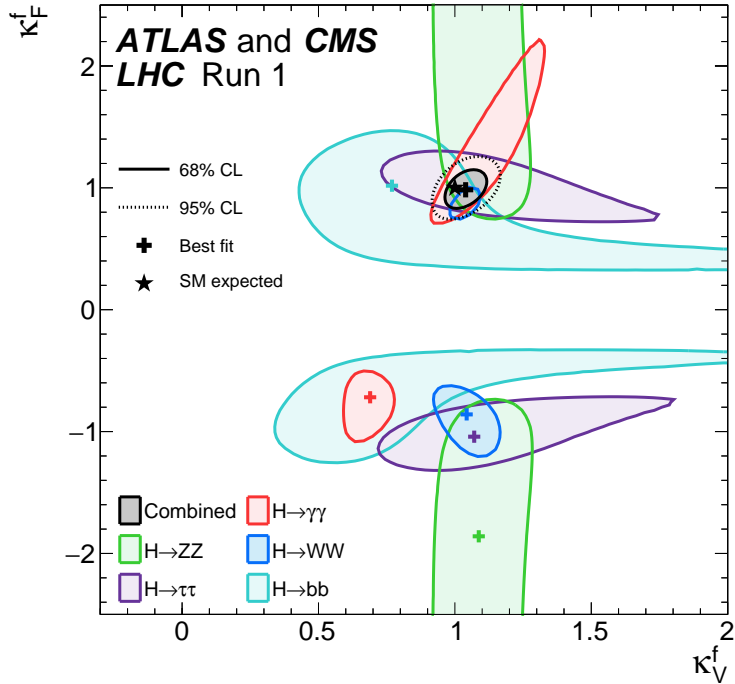


Figure 2.18: Combination of the ATLAS and CMS fits for coupling modifiers κ_t - κ_V ; also shown the individual decay channels combination and their global combination. No assumptions have been made on the sign of the coupling modifiers [53].

939 ATLAS and CMS have performed analysis of the anomalous H-f coupling by making
 940 likelihood scans for the two coupling modifiers, κ_t and κ_V , under the assumption that
 941 $\kappa_Z = \kappa_W = \kappa_V$ and $\kappa_t = \kappa_\tau = \kappa_b = \kappa_f$. Figure 2.18 shows the result of the combination
 942 of ATLAS and CMS fits; also the individual decay channels combination and the
 943 global combination results are shown.

944 While all the channels are compatible for positive values of the modifiers, for negative
 945 values of κ_t there is no compatibility. The best fit for individual channels is compatible
 946 with negative values of κ_t except for the $H \rightarrow bb$ channel which is expected to be the

947 most sensitive channel; therefore, the best fit for the global fit yields $\kappa_t \geq 0$. Thus,
948 the anomalous H-t coupling cannot be excluded completely.

949 **Chapter 3**

950 **The CMS experiment at the LHC**

951 **3.1 Introduction**

952 Located on the Swiss-French border, the European Council for Nuclear Research
953 (CERN) is the largest scientific organization leading the particle physics research.
954 About 13000 people in a broad range of fields including users, students, scientists,
955 engineers, among others, contribute to the data taking and analysis, with the goal
956 of unveiling the secrets of nature and revealing the fundamental structure of the
957 universe. CERN is also the home of the Large Hadron Collider (LHC), the largest
958 circular particle accelerator around the world, where protons (or heavy ions) traveling
959 close to the speed of light, are made to collide. These collisions open a window
960 to investigate how particles (and their constituents if they are composite) interact
961 with each other, providing clues about the laws of nature. This chapter presents an
962 overview of the LHC structure and operation. A detailed description of the CMS
963 detector is offered, given that the data used in this thesis have been taken with this
964 detector.

965 3.2 The LHC

966 With 27 km of circumference, the LHC is currently the largest and most powerful
 967 circular accelerator in the world. It is installed in the same tunnel where the Large
 968 Electron-Positron (LEP) collider was located, taking advantage of the existing infras-
 969 tructure. The LHC is also the larger accelerator in the CERN's accelerator complex
 970 and is assisted by several successive accelerating stages before the particles are in-
 971 jected into the LHC ring where they reach their maximum energy (see figure 3.1).

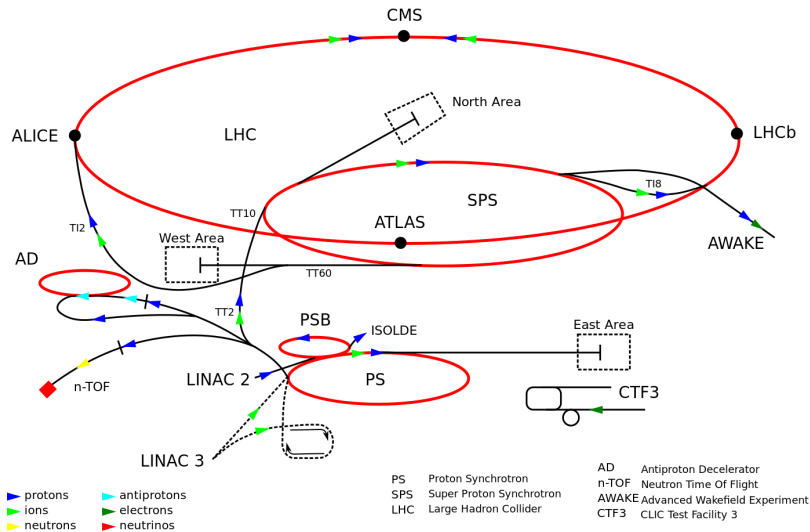


Figure 3.1: CERN accelerator complex. Blue arrows show the path followed by protons along the acceleration process [54].

972 LHC runs in three modes depending on the particles being accelerated

- 973 • Proton-Proton collisions (pp) for multiple physics experiments.
- 974 • Lead-Lead collisions ($Pb-Pb$) for heavy ion experiments.
- 975 • Proton-Lead collisions ($p-Pb$) for quark-gluon plasma experiments.

976 In this thesis only pp collisions will be considered.

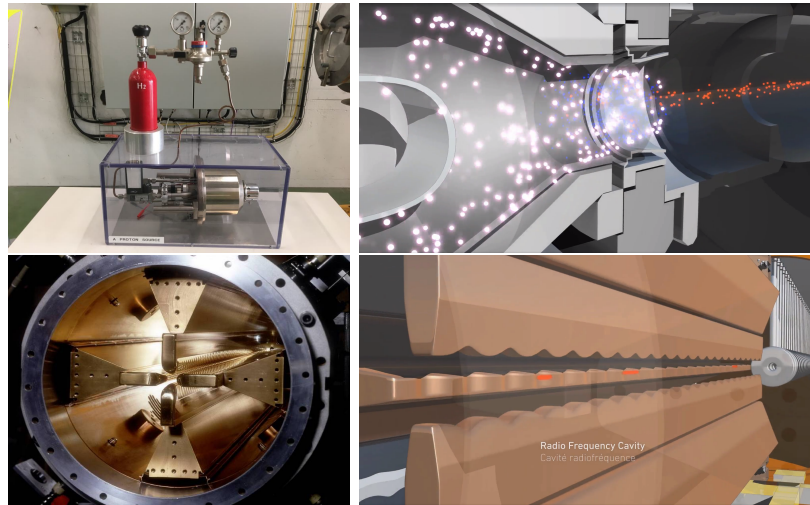


Figure 3.2: LHC protons source and the first acceleration stage. Top: the bottle contains hydrogen gas (white dots) which is injected into the metal cylinder to be broken down into electrons(blue dots) and protons(red dots); Bottom: the obtained protons are directed towards the radio frequency quadrupole which perform the first acceleration, focus the beam and create the bunches of protons. [58, 59]

978 Collection of protons starts with hydrogen atoms taken from a bottle, containing hy-
 979 drogen gas, and injecting them in a metal cylinder; hydrogen atoms are broken down
 980 into electrons and protons by an intense electric field (see figure3.2 top). The result-
 981 ing protons leave the metal cylinder towards a radio frequency quadrupole (RFQ)
 982 that focus the beam, accelerates the protons and creates the packets of protons called
 983 bunches. In the RFQ, an electric field is generated by a RF wave at a frequency that
 984 matches the resonance frequency of the cavity where the electrodes are contained.
 985 The beam of protons traveling on the RFQ axis experiences an alternating electric
 986 field gradient that generates the focusing forces.

987

988 In order to accelerate the protons, a longitudinal time-varying electric field component
 989 is added to the system; it is done by giving the electrodes a sinus-like profile as shown
 990 in figure 3.2 bottom. By matching the speed and phase of the protons with the
 991 longitudinal electric field the bunching is performed; protons synchronized with the

992 RFQ (synchronous proton) do not feel an accelerating force, but those protons in the
 993 beam that have more (or less) energy than the synchronous proton (asynchronous
 994 protons) will feel a decelerating (accelerating) force; therefore, asynchronous protons
 995 will oscillate around the synchronous ones forming bunches of protons [56]. From the
 996 RFQ protons emerge with energy 750 keV in bunches of about 1.15×10^{11} protons [57].

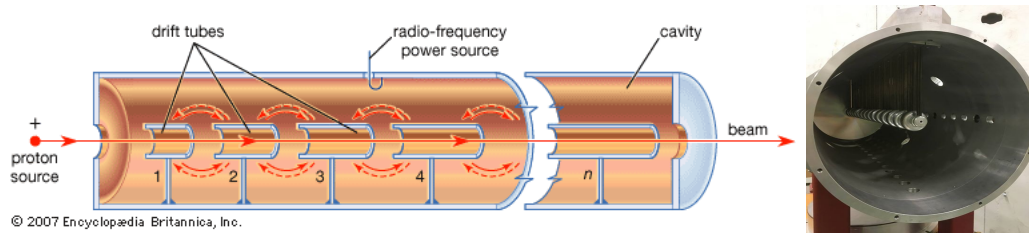


Figure 3.3: The LINAC2 accelerating system at CERN. Electric fields generated by radio frequency (RF) create acceleration and deceleration zones inside the cavity; deceleration zones are blocked by drift tubes where quadrupole magnets focus the proton beam. [60]

997 Proton bunches coming from the RFQ go to the linear accelerator 2 (LINAC2) where
 998 they are accelerated to reach 50 MeV energy. In the LINAC2 stage, acceleration
 999 is performed using electric fields generated by radio frequency which create zones
 1000 of acceleration and deceleration as shown in figure 3.3. In the deceleration zones,
 1001 the electric field is blocked using drift tubes where protons are free to drift while
 1002 quadrupole magnets focus the beam.

1003

1004 The beam coming from LINAC2 is injected into the proton synchrotron booster
 1005 (PSB) to reach 1.4 GeV in energy. The next acceleration is provided at the pro-
 1006 ton synchrotron (PS) up to 26 GeV, followed by the injection into the super proton
 1007 synchrotron (SPS) where protons are accelerated to 450 GeV. Finally, protons are
 1008 injected into the LHC where they are accelerated to the target energy of 6.5 TeV.
 1009 PSB, PS, SPS and LHC accelerate protons using the same RF acceleration technique
 1010 described before.

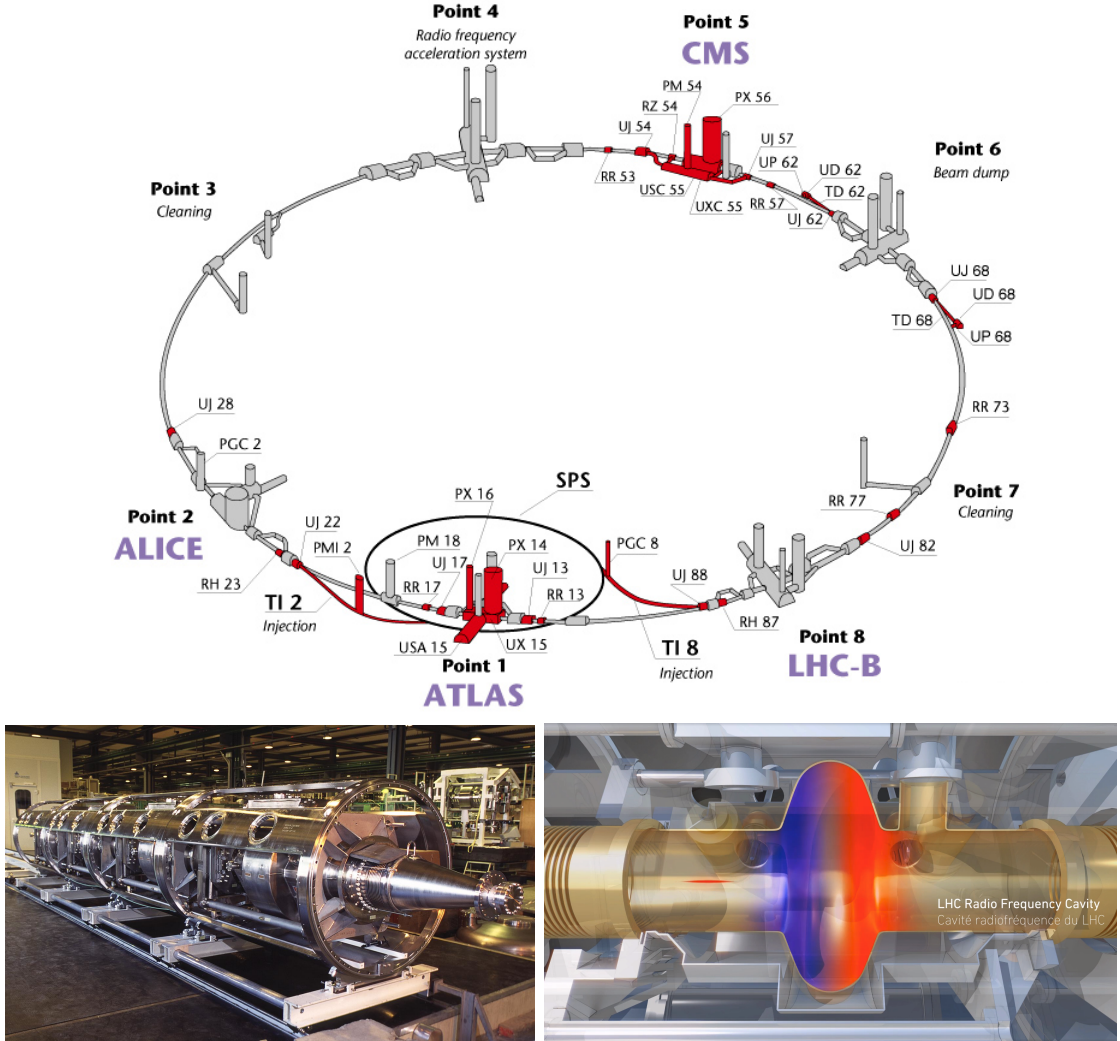


Figure 3.4: Top: LHC layout. The red zones indicate the infrastructure additions to the LEP installations, built to accommodate the ATLAS and CMS experiments which exceed the size of the former experiments located there [55]. Bottom: LHC RF cavities. A module accommodates 4 cavities that accelerate protons and preserve the bunch structure of the beam. [59, 61]

1011 LHC has a system of 16 RF cavities located in the so-called point 4, as shown in
 1012 figure 3.4 top, tuned at a frequency of 400 MHz and the protons are carefully timed,
 1013 so in addition to the acceleration effect the bunch structure of the beam is preserved.
 1014 Bottom side of figure 3.4 shows a picture of a RF module composed of 4 RF cavities
 1015 working in a superconducting state at 4.5 K; also is showed a representation of the

1016 accelerating electric field that accelerates the protons in the bunch.

1017

1018 While protons are accelerated in one section of the LHC ring, where the RF cavities
 1019 are located, in the rest of their path they have to be kept in the curved trajectory
 1020 defined by the LHC ring. Technically, LHC is not a perfect circle; RF, injection, beam
 1021 dumping, beam cleaning and sections before and after the experimental points where
 1022 protons collide are all straight sections. In total, there are 8 arcs 2.45 Km long each
 1023 and 8 straight sections 545 m long each. In order to curve the proton's trajectory in
 1024 the arc sections, superconducting dipole magnets are used.

1025

1026 Inside the LHC ring, there are two proton beams traveling in opposite directions in
 1027 two separated beam pipes; the beam pipes are kept at ultra-high vacuum ($\sim 10^{-9}$
 1028 Pa) to ensure that there are no particles that interact with the proton beams. The
 1029 superconducting dipole magnets used in LHC are made of a NbTi alloy, capable of
 1030 transporting currents of about 12000 A when cooled at a temperature below 2K using
 1031 liquid helium (see figure 3.5).

1032

1033 Protons in the arc sections of LHC feel a centripetal force exerted by the dipole
 1034 magnets which is perpendicular to the beam trajectory; The magnitude of magnetic
 1035 field needed can be found assuming that protons travel at $v \approx c$, using the standard
 1036 values for proton mass and charge and the LHC radius, as

$$F_m = \frac{mv^2}{r} = qBv \quad \rightarrow B = 8.33T \quad (3.1)$$

1037 which is about 100000 times the Earth's magnetic field. A representation of the mag-
 1038 netic field generated by the dipole magnets is shown on the bottom left side of figure

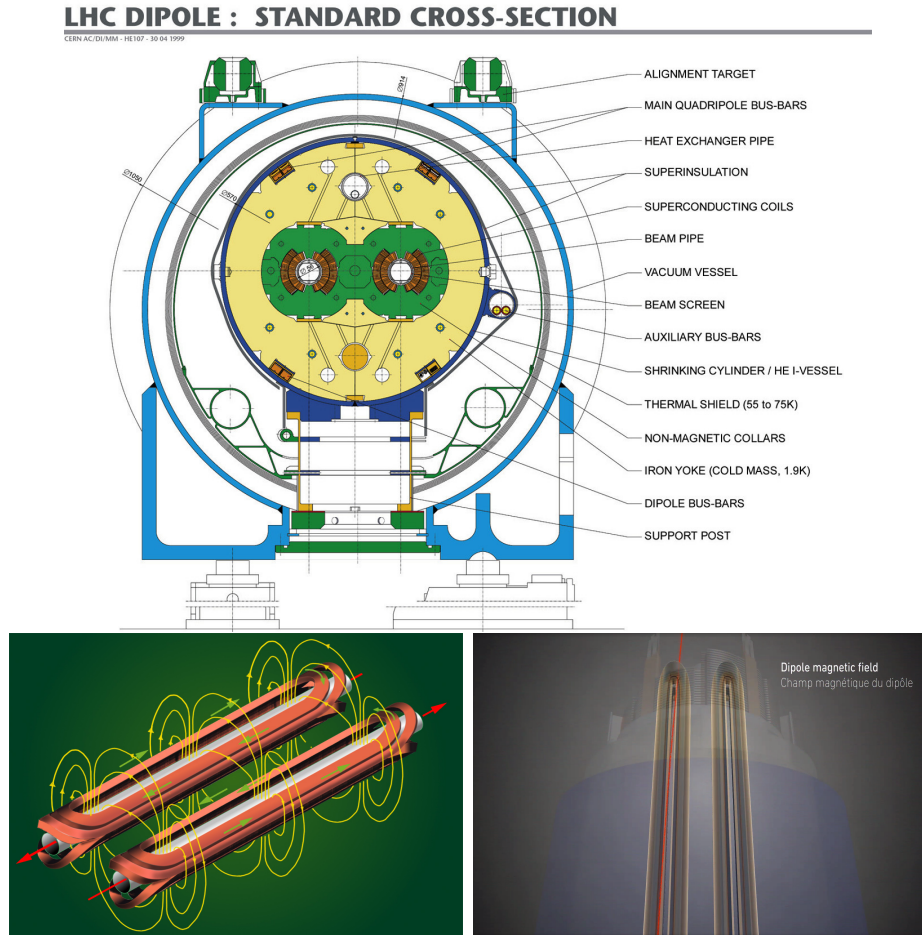


Figure 3.5: Top: LHC dipole magnet transverse view; cooling, shielding and mechanical support are indicated. Bottom left: Magnetic field generated by the dipole magnets; note that the direction of the field inside one beam pipe is opposite with respect to the other beam pipe which guarantee that both proton beams are curved in the same direction towards the center of the ring. The effect of the dipole magnetic field on the proton beam is represented on the bottom right side [59, 62, 63].

1039 3.5. The bending effect of the magnetic field on the proton beam is shown on the
 1040 bottom right side of figure 3.5. Note that the dipole magnets are not curved; the arc
 1041 section of the LHC ring is composed of straight dipole magnets of about 15 m. In
 1042 total there are 1232 dipole magnets along the LHC ring.

1043

1044 In addition to bending the beam trajectory, the beam has to be focused so it stays

1045 inside the beam pipe. The focusing is performed by quadrupole magnets installed in
 1046 a different straight section; in total 858 quadrupole magnets are installed along the
 1047 LHC ring. Other effects like electromagnetic interaction among bunches, interaction
 1048 with electron clouds from the beam pipe, the gravitational force on the protons, dif-
 1049 ferences in energy among protons in the same bunch, among others, are corrected
 1050 using sextupole and other magnetic multipoles.

1051

1052 The two proton beams inside the LHC ring are made of bunches with a cylindrical
 1053 shape of about 7.5 cm long and about 1 mm in diameter; when bunches are close
 1054 to the collision point (CP), the beam is focused up to a diameter of about 16 μm in
 1055 order to maximize the number of collisions per unit area and per second, known as
 1056 luminosity (L). Luminosity can be calculated using

$$L = fn \frac{N_1 N_2}{4\pi\sigma_x\sigma_y} \quad (3.2)$$

1057 where f is the revolution frequency, n is the number of bunches per beam, N_1 and
 1058 N_2 are the numbers of protons per bunch (1.5×10^{11}), σ_x and σ_y are the gaussian
 1059 transverse sizes of the bunches. The expected luminosity is about

$$f = \frac{v}{2\pi r_{LHC}} \approx \frac{3 \times 10^8 \text{ m/s}}{27 \text{ km}} \approx 11.1 \text{ kHz},$$

$$n = 2808$$

$$N_1 = N_2 = 1.5 \times 10^{11}$$

$$\sigma_x = \sigma_y = 16 \mu\text{m}$$

1060

$$L = 1.28 \times 10^{34} \text{ cm}^{-2} \text{ s}^{-1} = 1.28 \times 10^{-5} \text{ fb}^{-1} \text{ s}^{-1} \quad (3.3)$$

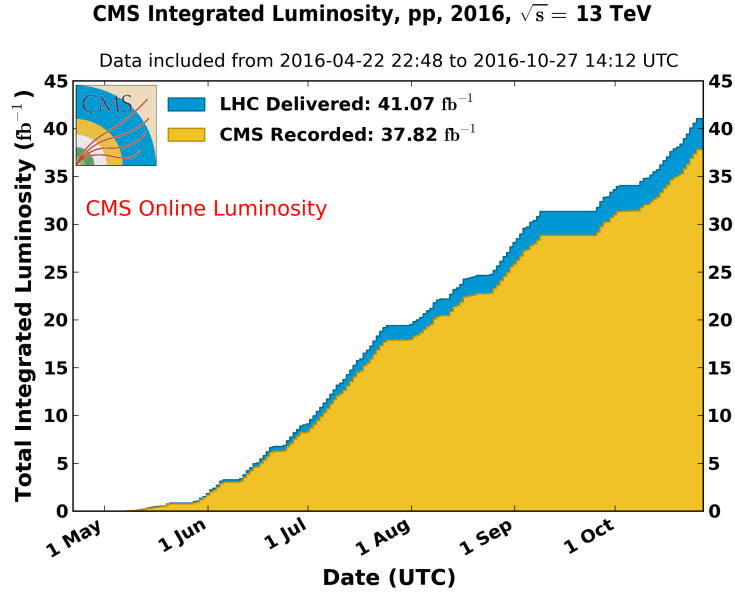


Figure 3.6: Integrated luminosity delivered by LHC and recorded by CMS during 2016. The difference between the delivered and the recorded luminosity is due to fails and issues occurred during the data taking in the CMS experiment [64].

1061 Luminosity is a fundamental aspect of LHC given that the bigger luminosity the
 1062 bigger number of collisions, which means that for processes with a very small cross
 1063 section the number of expected occurrences is increased and so the chances of being
 1064 detected. The integrated luminosity, i.e., the total luminosity, collected by the CMS
 1065 experiment during 2016 is shown in figure 3.6; the data analyzed in this thesis corre-
 1066 sponds to an integrated luminosity of 35.9 fb^{-1} at a center of mass-energy $\sqrt{s} = 13$
 1067 TeV.

1068

1069 A way to increase L is increasing the number of bunches in the beam. Currently, the
 1070 separation between two consecutive bunches in the beam is 7.5 m which corresponds
 1071 to a time separation of 25 ns. In the full LHC ring the allowed number of bunches is
 1072 $n = 27\text{km}/7.5\text{m} = 3600$; however, there are some gaps in the bunch pattern intended
 1073 for preparing the dumping and injection of the beam, thus, the proton beams are

1074 composed of 2808 bunches.

1075

1076 Once the proton beams reach the desired energy, they are brought to cross each other
 1077 producing proton-proton collisions. The bunch crossing happens in precise places
 1078 where the four LHC experiments are located, as seen in the top of figure 3.7. In 2008,
 1079 the first set of collisions involved protons with $\sqrt{s} = 7$ TeV; the energy was increased
 1080 to 8 TeV in 2012 and to 13 TeV in 2015.

1081

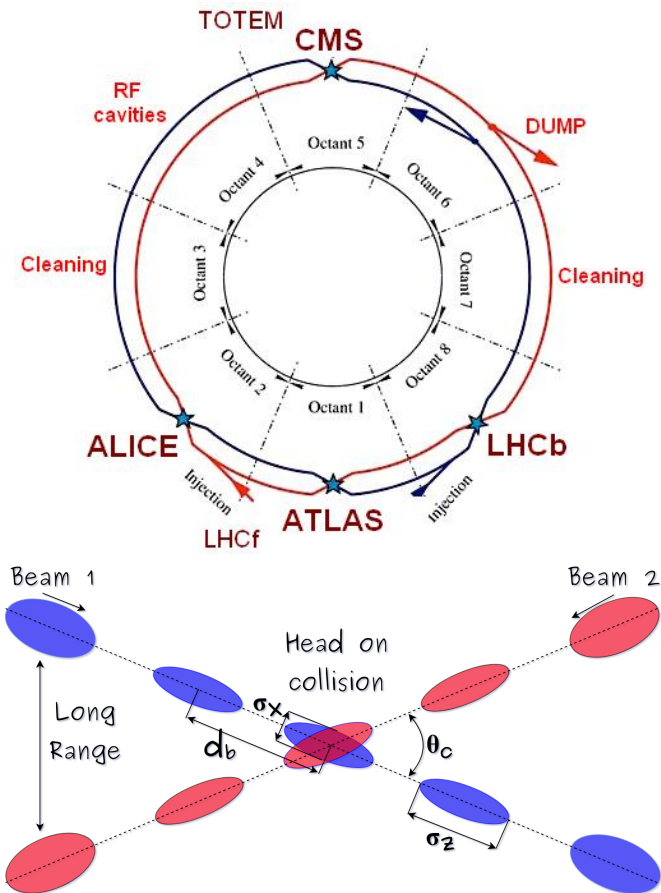


Figure 3.7: Top: LHC interaction points. Bunch crossing occurs where the LHC experiments are located [65]. Sections indicated as cleaning are dedicated to collimate the beam in order to protect the LHC ring from collisions with protons in very spreaded bunches. Bottom: bunch crossing scheme. Since the bunch crossing is not perfectly head-on, the luminosity is reduced in a factor of 17%; adapted from reference [77].

1082 CMS and ATLAS experiments, which are multi-purpose experiments, are enabled
 1083 to explore physics in any of the collision modes. LHCb experiment is optimized
 1084 to explore bottom quark physics, while ALICE is optimized for heavy ion collisions
 1085 searches; TOTEM and LHCf are dedicated to forward physics studies; MoEDAL (not
 1086 indicated in the figure) is intended for monopoles or massive pseudo stable particles
 1087 searches.

1088

1089 At the CP there are two interesting details that need to be addressed. The first one
 1090 is that the bunch crossing does not occur head-on but at a small crossing angle “ θ_c ”
 1091 (280 μ rad in CMS and ATLAS) as shown in the bottom side of figure 3.7, affecting
 1092 the overlapping between bunches; the consequence is a reduction of about 17% in
 1093 the luminosity (represented by a factor not included in eqn: 3.2). The second one
 1094 is the occurrence of multiple pp collisions in the same bunch crossing; this effect is
 1095 called pile-up (PU). A fairly simple estimation of the PU follows from estimating the
 1096 probability of collision between two protons, one from each of the bunches in course
 1097 of collision; it depends roughly on the ratio of proton size and the cross section of the
 1098 bunch in the interaction point, i.e.,

$$P(pp\text{-}collision) \sim \frac{d_{proton}^2}{\sigma_x \sigma_y} = \frac{(1\text{fm})^2}{(16\mu\text{m})^2} \sim 4 \times 10^{-21} \quad (3.4)$$

1099 however, there are $N = 1.15 \times 10^{11}$ protons in a bunch, thus the estimated number of
 1100 collisions in a bunch crossing is

$$PU = N^2 * P(pp\text{-}collision) \sim 50 \text{ } pp\text{-}collision \text{ per bunch crossing}, \quad (3.5)$$

1101 about 20 of those pp collisions are inelastic. Each collision generates a vertex, but
 1102 only the most energetic is considered as a primary vertex; the rest are considered as

1103 PU vertices. A multiple pp collision event in a bunch crossing at CMS is showed in
 1104 figure3.8. Unstable particles outgoing from the primary vertex will eventually decay;
 1105 this decay vertex is known as a secondary vertex.

1106

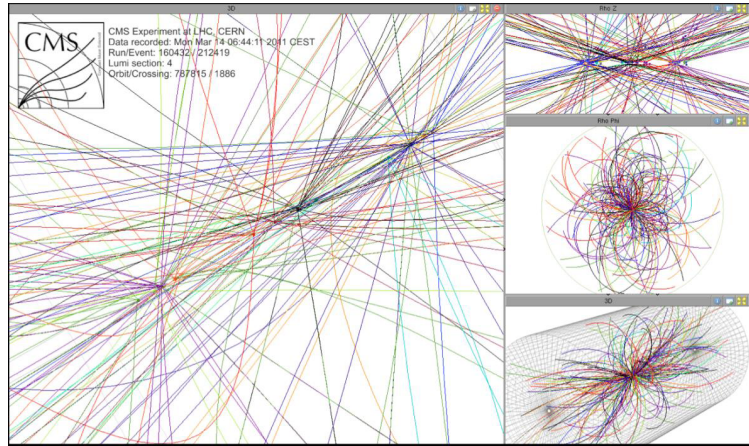


Figure 3.8: Multiple pp collision bunch crossing at CMS. Only the most energetic vertex is considered and the rest are catalogued as PU vertices [66].

1107 Next section presents a description of the CMS detector which it is the detector used
 1108 to collect the data used in this thesis.

1109 **3.3 The CMS experiment**

1110 CMS is a general-purpose detector designed to conduct research in a wide range
 1111 of physics from the standard model to new physics like extra dimensions and dark
 1112 matter. Located at the point 5 in the LHC layout as shown in figure 3.4, CMS is
 1113 composed of several detection systems distributed in a cylindrical structure; in total,
 1114 CMS weights about 12500 tons in a very compact 21.6 m long and 14.6 m diameter
 1115 cylinder. It was built in 15 separate sections at the ground level and lowered to the
 1116 cavern individually to be assembled. A complete and detailed description of the CMS

1117 detector and its components is given in reference [67] on which this section is based on.

1118

1119 Figure 3.9 shows the layout of the CMS detector. The design is driven by the require-
 1120 ments on the identification, momentum resolution and unambiguous charge determi-
 1121 nation of the muons; therefore, a large bending power is provided by the solenoid
 1122 magnet made of superconducting cable capable to generate a 3.8 T magnetic field.
 1123 The detection system is composed of (from the innermost to the outermost)

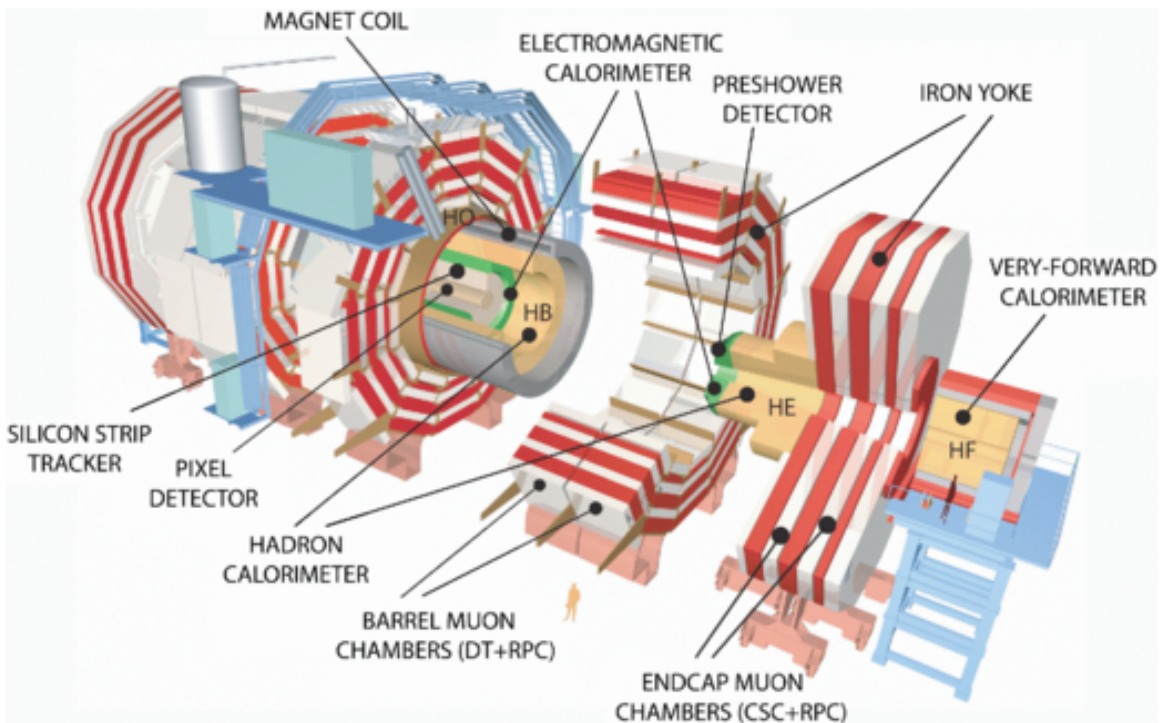


Figure 3.9: Layout of the CMS detector. The several subdetectors are indicated. The central region of the detector is referred as the Barrel section while the endcaps are referred as the forward sections. [68].

1124 • Pixel detector.

1125 • Silicon strip tracker.

1126 • Preshower detector.

1127 • Electromagnetic calorimeter.

1128 • Hadronic calorimeter.

1129 • Muon chambers (Barrel and endcap)

1130 The central region of the detector is commonly referred as the barrel section while the
 1131 endcaps are referred as the forward sections of the detector; thus, each subdetector
 1132 is composed of a barrel section and a forward section.

1133 3.3.1 Coordinate system

1134 The coordinate system used by CMS is centered in the geometrical center of the
 1135 detector which is the same as the CP as shown in figure 3.10. The z -axis is parallel
 1136 to the beam direction, while the Y -axis pointing vertically upward, and the X -axis
 1137 pointing radially inward toward the center of the LHC.

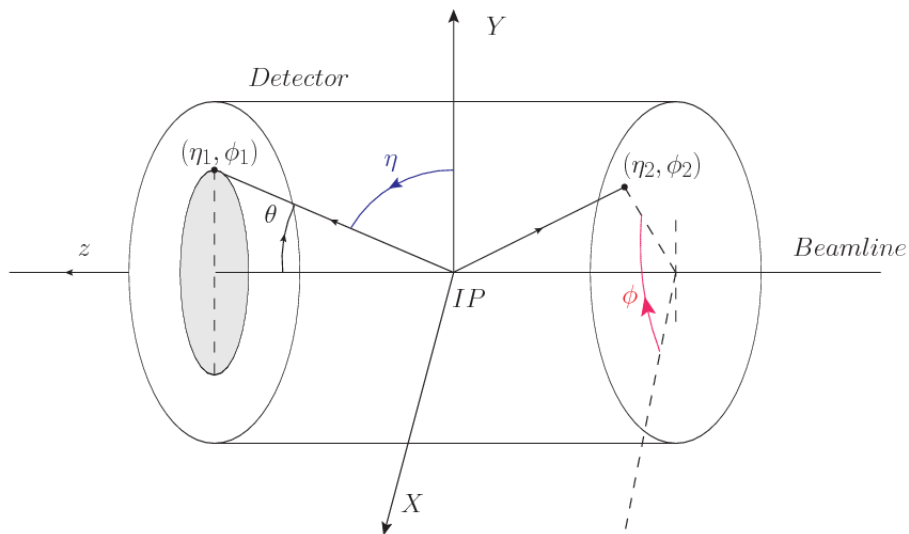


Figure 3.10: CMS detector coordinate system.

1138 In addition to the common cartesian and cylindrical coordinate systems, two coordi-
 1139 nates are of particular utility in particle physics: rapidity(y) and pseudorapidity(η),

1140 defined in connection to the polar angle θ , energy and longitudinal momentum com-
 1141 ponent (momentum along the z -axis) according to

$$y = \frac{1}{2} \ln \frac{E + p_z}{E - p_z} \quad \eta = -\ln \left(\tan \frac{\theta}{2} \right) \quad (3.6)$$

1142 Rapidity is related to the angle between the XY -plane and the direction in which the
 1143 products of a collision are emitted; it has the nice property that the difference between
 1144 the rapidities of two particles is invariant with respect to Lorentz boosts along the z -
 1145 axis. Thus, data analysis becomes more simple when based on rapidity; however, it is
 1146 not simple to measure the rapidity of highly relativistic particles, as those produced
 1147 after pp collisions. Under the highly relativistic motion approximation, y can be
 1148 rewritten in terms of the polar angle, concluding that rapidity is approximately equal
 1149 to the pseudorapidity defined above, i.e., $y \approx \eta$. Note that η is easier to measure than y
 1150 given the direct relationship between the former and the polar angle. Angular distance
 1151 between two objects in the detector (ΔR) is defined in terms of their coordinates
 1152 $(\eta_1, \phi_1), (\eta_2, \phi_2)$ as

$$\Delta R = \sqrt{(\Delta\eta)^2 - (\Delta\phi)^2} \quad (3.7)$$

1153 3.3.2 Pixels detector

1154 The CMS tracking system is designed to provide a precise measurement of the tra-
 1155 jectory (*track*) followed by the charged particles created after the pp collisions; also,
 1156 the precise reconstruction of the primary and secondary origins (*vertices*) is expected
 1157 in an environment where, each 25 ns, the bunch crossing produce about 20 inelastic
 1158 collisions and about 1000 particles. An increment in the luminosity is ongoing which
 1159 implies that the PU will increase accordingly.

1161 The pixel detector was replaced during the 2016-2017 extended year-end technical
 1162 stop, due to the increasingly challenging operating conditions like the higher particle
 1163 flow and more radiation harsh environment, among others. The new one is respond-
 1164 ing as expected, reinforcing its crucial role in the successful way to fulfill the new
 1165 LHC physics objectives after the discovery of the Higgs boson. The last chapter of
 1166 this thesis is dedicated to describe my contribution to the “Forward Pixel Phase 1
 1167 upgrade”.

1168

1169 The current pixel detector is composed of 1856 silicon pixel detector modules orga-
 1170 nized in four-barrel layers in the central region and three disks in the forward region;
 1171 it is designed to record efficiently and with high precision, up to $10\mu\text{m}$ in the XY -
 1172 plane and $20\mu\text{m}$ in the z -direction, the first four space-points (*hits*) near to the CP
 1173 region (see figure 3.11 left side) in the range $|\eta| \leq 2.5$. The first barrel layer is located
 1174 at a radius of 30 mm from the beamline, while the fourth layer is located at a radius
 1175 of 160 mm closer to the strip tracker inner barrel layer (see section 3.3.3) in order to
 1176 reduce the rate of fake tracks. The high granularity of the detector is represented in
 1177 its about 123 Mpixels, each of size $100 \times 150\mu\text{m}^2$, which is almost twice the channels
 1178 of the old detector. The transverse momentum resolution of tracks can be measured
 1179 with a resolution of 1-2% for muons of $p_T = 100$ GeV.

1180

1181 Some of the improvements with respect to the previous pixel detector include a higher
 1182 average tracking efficiency and lower average fake rate as well as higher track impact
 1183 parameter resolution which is fundamental in order to increase the efficiency in the
 1184 identification of jets originating from b quarks (b-tagging). A significant source of
 1185 improvement comes from the overall reduction in the material budget of the detector
 1186 which results in fewer photon conversions and less multiple scattering from charged

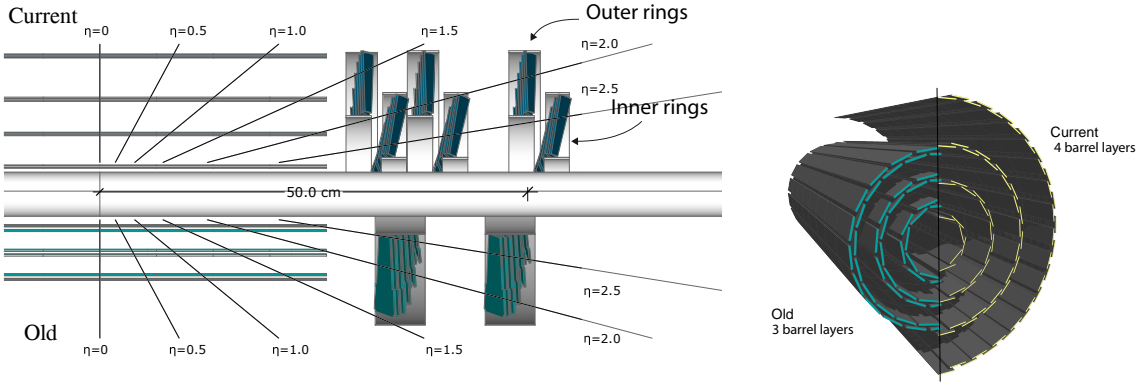


Figure 3.11: CMS pixel detector schematic view. Left: layout comparing the layers and disks in the old and current pixel detectors. Right: Transverse-oblique view comparing the pixel barrel layers in the two [70].

1187 particles.

1188 3.3.3 Silicon strip tracker

1189 The silicon strip tracker (SST) is the second stage in the CMS tracking system. The
 1190 top side of figure 3.12 shows a schematic of the SST. The inner tracker region is com-
 1191 posed of the tracker inner barrel (TIB) and the tracker inner disks (TID) covering the
 1192 region $r < 55$ cm and $|z| < 118$ cm. The TIB is composed of 4 layers while the TID
 1193 is composed of 3 disks at each end. The silicon sensors in the inner tracker are 320
 1194 μm thick, providing a resolution of about 13-38 μm in the $r\phi$ position measurement.
 1195

1196 The modules indicated in blue in the schematic view of figure 3.12 are two modules
 1197 mounted back-to-back and rotated in the plane of the module by a “stereo” angle of
 1198 100 mrad; the hits from these two modules, known as “stereo hits”, are combined to
 1199 provide a measurement of the second coordinate (z in the barrel and r on the disks)
 1200 allowing the reconstruction of hit positions in 3-D.

1201

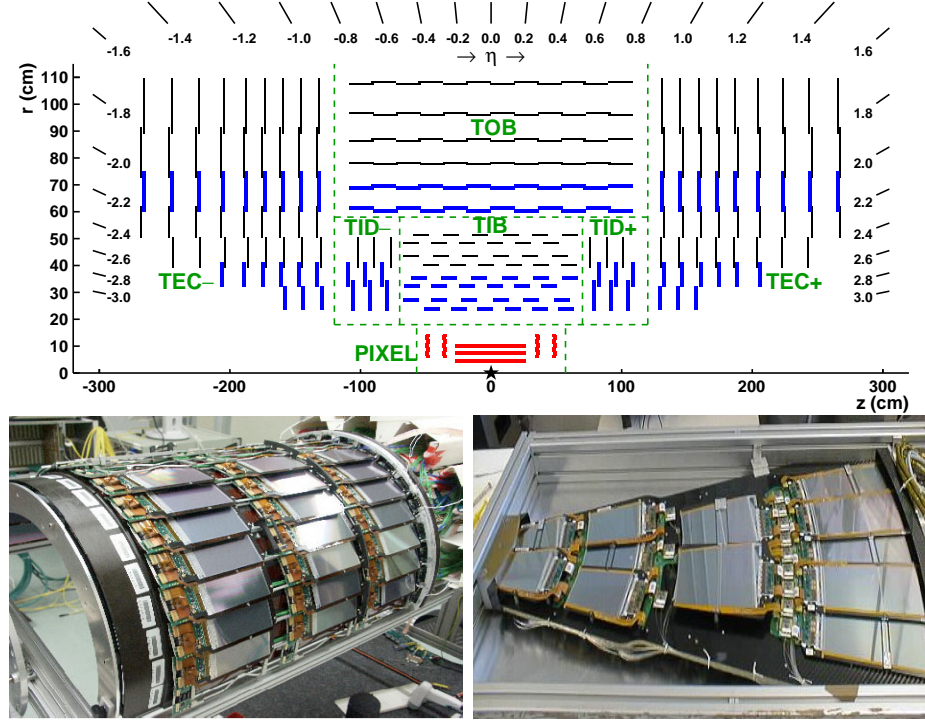


Figure 3.12: Top: CMS Silicon Strip Tracker (SST) schematic view. The SST is composed of the tracker inner barrel (TIB), the tracker inner disks (TID), the tracker outer barrel (TOB) and the tracker endcaps (TEC). Each part is made of silicon strip modules; the modules in blue represent two modules mounted back-to-back and rotated in the plane of the module by a stereo angle of 120 mrad in order to provide a 3-D reconstruction of the hit positions. Bottom: pictures of the TIB (left) and TEC (right) modules [71–73].

1202 The outer tracker region is composed of the tracker outer barrel (TOB) and the
 1203 tracker endcaps (TEC). The six layers of the TOB offer coverage in the region $r > 55$
 1204 cm and $|z| < 118$ cm, while the 9 disks of the TEC cover the region $124 < |z| < 282$
 1205 cm. The resolution offered by the outer tracker is about $13\text{--}38 \mu\text{m}$ in the $r\phi$ position
 1206 measurement. The inner four TEC disks use silicon sensors $320 \mu\text{m}$ thick; those in
 1207 the TOB and the outer three TEC disks use silicon sensors of $500 \mu\text{m}$ thickness. The
 1208 silicon strips run parallel to the z -axis and the distance between strips varies from 80
 1209 μm in the inner TIB layers to $183 \mu\text{m}$ in the inner TOB layers; in the endcaps the
 1210 wedge-shaped sensors with radial strips, whose pitch range between $81 \mu\text{m}$ at small
 1211 radii and $205 \mu\text{m}$ at large radii.

1212

1213 The whole SST has 15148 silicon modules, 9.3 million silicon strips and cover a total
 1214 active area of about 198 m^2 .

1215 **3.3.4 Electromagnetic calorimeter**

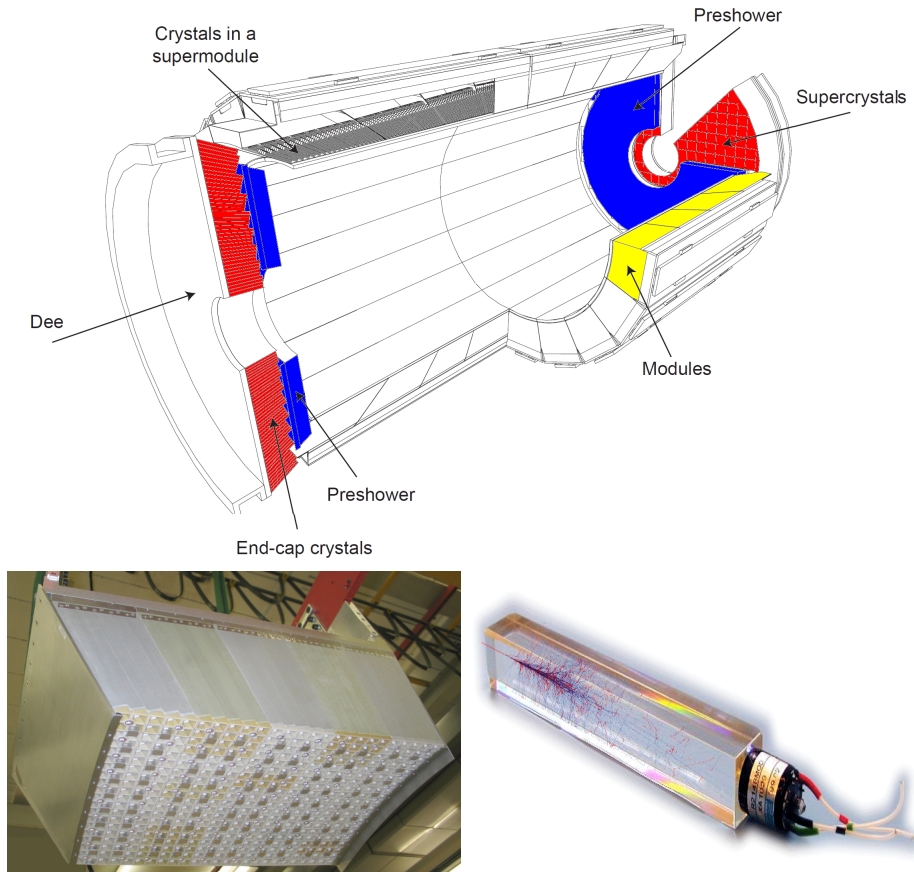


Figure 3.13: Top: CMS ECAL schematic view. Bottom: Module equipped with the crystals (left); ECAL crystal(right).

1216 The CMS electromagnetic calorimeter (ECAL) is designed to measure the energy of
 1217 electrons and photons. It is composed of 75848 lead tungstate crystals which have a
 1218 short radiation length (0.89 cm) and fast response, since 80% of the light is emitted
 1219 within 25 ns; however, they are combined with Avalanche photodiodes (APDs) as

1220 photodetectors given that crystals themselves have a low light yield ($30\gamma/\text{MeV}$). A
 1221 schematic view of the ECAL is shown in figure 3.13.

1222

1223 Energy is measured when electrons and photons are absorbed by the crystals which
 1224 generates an electromagnetic “shower”, as seen in bottom right picture of the fig-
 1225 ure3.13; the shower is seen as a *cluster* of energy which depending on the amount
 1226 of energy deposited can involve several crystals. The ECAL barrel (EB) covers the
 1227 region $|\eta| < 1.479$, using crystals of depth of 23 cm and $2.2 \times 2.2 \text{ cm}^2$ transverse
 1228 section; the ECAL endcap (EE) covers the region $1.479 < |\eta| < 3.0$ using crystals
 1229 of depth 22 cm and transverse section of $2.86 \times 2.86 \text{ cm}^2$; the photodetectors used
 1230 are vacuum phototriodes (VPTs). Each EE is divided in two structures called “Dees”.

1231

1232 In front of the EE, it is installed the preshower detector (ES) which covers the region
 1233 $1.653 < |\eta| < 2.6$. The ES provides a precise measurement of the position of electro-
 1234 magnetic showers, which allows to distinguish electrons and photons signals from π^0
 1235 decay signals. The ES is composed of a layer of lead absorber followed by a layer of
 1236 plastic scintillators

1237 3.3.5 Hadronic calorimeter

1238 Hadrons are not absorbed by the ECAL but by the hadron calorimeter (HCAL),
 1239 which is made of a combination of alternating brass absorber layers and silicon photo-
 1240 multiplier(SiPM) layers; therefore, particles passing through the scintillator material
 1241 produce showers, as in the ECAL, as a result of the inelastic scattering of the hadrons
 1242 with the detector material. Since the particles are not absorbed in the scintillator,
 1243 their energy is sampled; therefore the total energy is not measured but estimated from

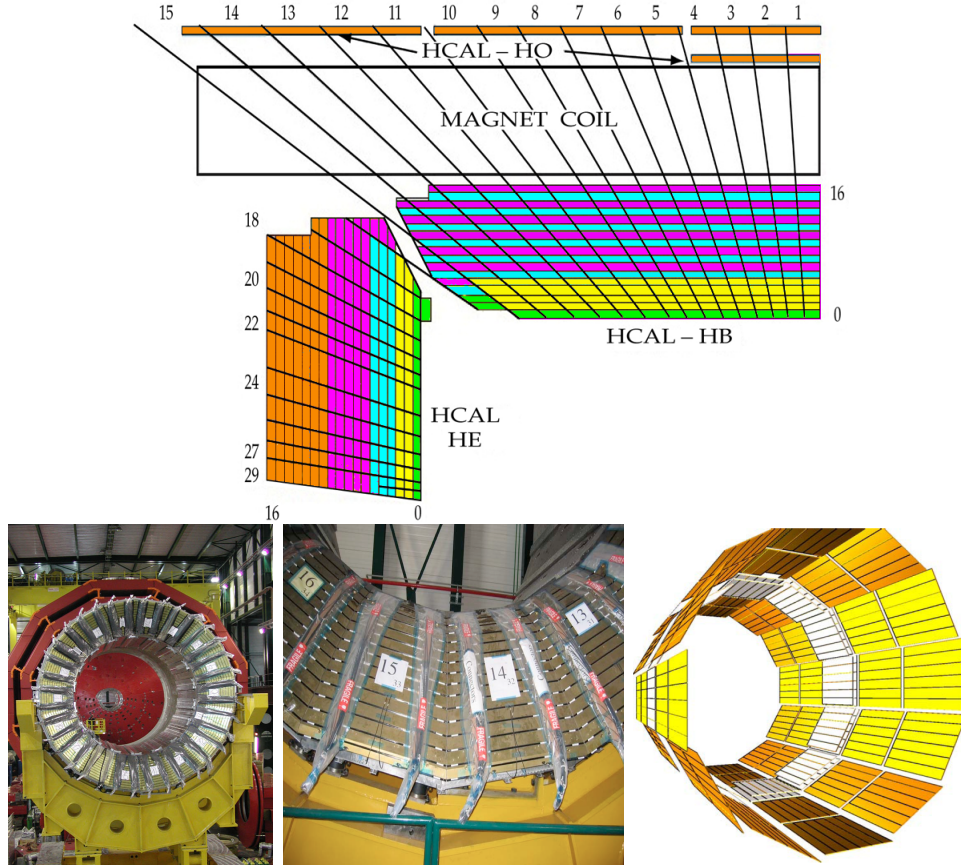


Figure 3.14: Top: CMS HCAL schematic view, the colors indicate the layers that are grouped into the same readout channels. Bottom: picture of a section of the HB; the absorber material is the golden region and scintillators are placed in between the absorber material (left and center). Schematic view of the HO (right). [74,75]

1244 the energy clusters, which reduce the resolution of the detector. Brass was chosen
 1245 as the absorber material due to its short interaction length ($\lambda_I = 16.42\text{cm}$) and its
 1246 non-magnetivity. Figure 3.14 shows a schematic view of the CMS HCAL.

1247

1248 The HCAL is divided into four sections; the Hadron Barrel (HB), the Hadron Outer
 1249 (HO), the Hadron Endcap (HE) and the Hadron Forward (HF) sections. The HB
 1250 covers the region $0 < |\eta| < 1.4$, while the HE covers the region $1.3 < |\eta| < 3.0$. The HF,
 1251 made of quartz fiber scintillator and steel as absorption material, covers the forward

region $3.0 < |\eta| < 5.2$. Both the HB and HF are located inside the solenoid. The HO is placed outside the magnet as an additional layer of scintillators with the purpose of measure the energy tails of particles passing through the HB and the magnet (see figure 3.14 top and bottom right). The upgrades made to the HCAL during the technical stop 2016-2017 consisted in the replacement of the photo transducer, in order to improve the efficiency.

3.3.6 Superconducting solenoid magnet

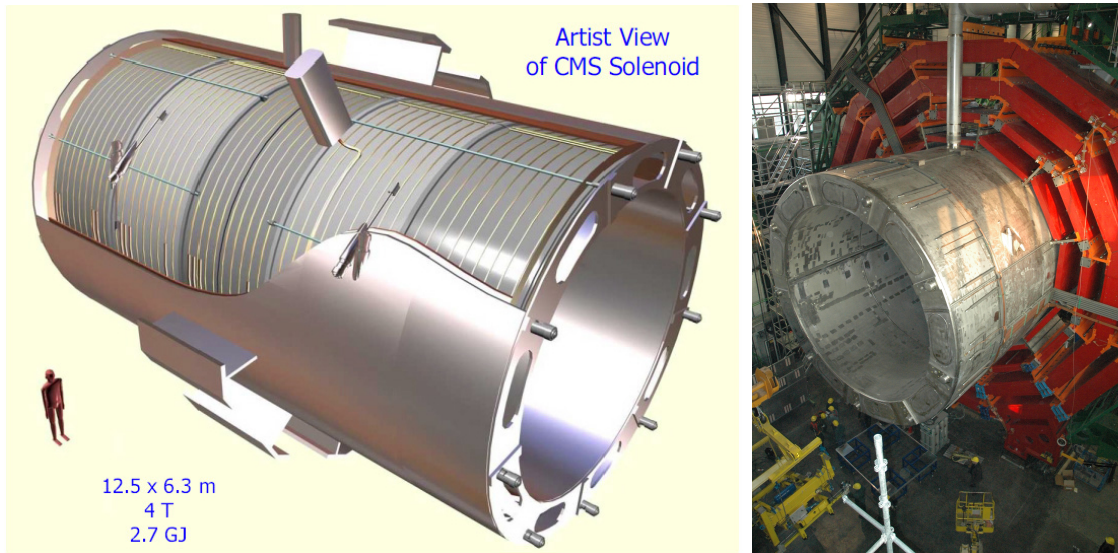


Figure 3.15: Artistic representation of the CMS solenoid magnet(left). The magnet is supported on an iron yoke (right) which also serves as the house of the muon detector and as mechanical support for the whole CMS detector [69].

The superconducting magnet installed in the CMS detector is designed to provide an intense and highly uniform magnetic field in the central part of the detector. In fact, the tracking system takes advantage of the bending power of the magnetic field to measure with precision the momentum of the particles that traverse it; the unambiguous determination of the sign for high momentum muons was a driven principle during the design of the magnet. The magnet has a diameter of 6.3 m, a length of 12.5

1265 m and a cold mass of 220 t; the generated magnetic field reaches a strength of 3.8T.
 1266 Since it is made of Ni-Tb superconducting cable it has to operate at a temperature
 1267 of 4.7 K by using a helium cryogenic system; the current circulating in the cables
 1268 reaches 18800 A under normal running conditions. The left side of figure 3.15 shows
 1269 an artistic view of the CMS magnet, while the right side shows a transverse view of
 1270 the cold mass where the winding structure is visible.

1271

1272 The yoke (see figure 3.15), composed of 5 barrel wheels and 6 endcap disks made
 1273 of iron, serves not only as the media for magnetic flux return but also provides the
 1274 house for the muon detector system and structural stability to the full detector.

1275 3.3.7 Muon system

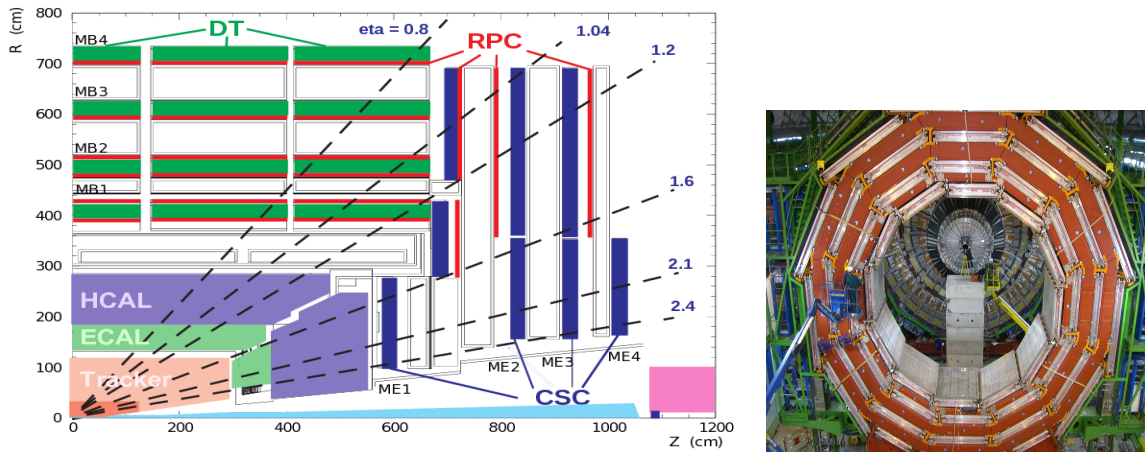


Figure 3.16: Left: CMS muon system schematic view; Right: one of the yoke rings with the muon DTs and RPCs installed; in the back it is possible to see the muon endcap [76].

1276 Muons are the only charged particles able to pass through all the CMS detector due
 1277 to their low ionization energy loss; thus, muons can be separated easily from the
 1278 high amount of particles produced in a pp collision. Also, muons are expected to be
 1279 produced in the decay of several new particles; therefore, a good detection of muons

1280 was on the leading principles when designing the CMS detector.

1281

1282 The CMS muon detection system (muon spectrometer) is embedded in the return
1283 yoke as seen in figure 3.16. It is composed of three different detector types, the drift
1284 tube chambers (DT), Cathode strip chambers (CSC), and resistive plate chambers
1285 (RPC); DT are located in the central region $\eta < 1.2$ arranged in four layers of drift
1286 chambers filled with an Ar/CO₂ gas mixture.

1287

1288 The muon endcaps are made of CSCs covering the region $\eta < 2.4$ and filled with a
1289 mixture of Ar/CO₂/CF₄. The reason behind using a different detector type lies on
1290 the different conditions in the forward region like the higher muon rate and higher
1291 residual magnetic field compared to the central region.

1292

1293 The third type of detector used in the muon system is a set of four disks of RPCs
1294 working in avalanche mode. The RPCs provide good spatial and time resolutions.
1295 The track of $high - p_T$ muon candidates is built combining information from the
1296 tracking system and the signal from up to six RPCs and four DT chambers.

1297 The muon tracks are reconstructed from the hits in the several layers of the muon
1298 system.

1299 **3.3.8 CMS trigger system**

1300 Under normal conditions, CMS expects pp collisions every 25 ns, i.e., an interaction
1301 rate of 40 MHz for which it is not possible to store the recorded data in full. In order
1302 to handle this high event rate data, an online event selection, known as triggering, is
1303 performed; triggering reduce the event rate to 100 Hz for storage and further offline

1304 analysis.

1305

1306 The trigger system starts with a reduction of the event rate to 100 kHz in the so-called
 1307 “level 1 trigger (L1)”. L1 is based on dedicated programmable hardware like Field
 1308 Programmable Gate Arrays (FPGAs) and Application Specific Integrated Circuits
 1309 (ASICs), partly located in the detector itself; another portion is located in the CMS
 1310 under-ground cavern. Hit patterns information from the muon chambers and the en-
 1311 ergy deposits in the calorimeter are used to decide if an event is accepted or rejected,
 1312 according to selection requirements previously defined, which reflect the interesting
 1313 physics processes. Figure 3.17 shows the L1 trigger architecture.

1314

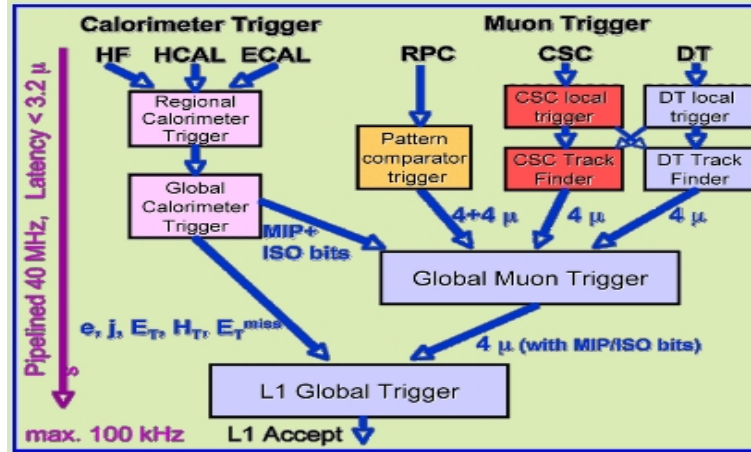


Figure 3.17: CMS Level-1 trigger architecture [77].

1315 The second stage in the trigger system is called “high-level trigger (HLT)”; events
 1316 accepted by L1 are passed to HLT in order to make an initial reconstruction of them.
 1317 HLT is software based and runs on a dedicated server farm, using selection algo-
 1318 rithms and high-level object definitions; the event rate at HLT is reduced to 100 Hz.
 1319 The first HLT stage takes information from the muon detectors and the calorimeters
 1320 to make the initial object reconstruction; in the next HLT stage, information from

1321 the pixel and strip detectors is used to do first fast-tracking and then full tracking
1322 online. This initial object reconstruction is used in further steps of the trigger system.

1323

1324 Events and preliminary reconstructed physics objects from HLT are sent to be fully
1325 reconstructed at the CERN computing center. Again, the pixel detector information
1326 provides high-quality seeds for the track reconstruction algorithm offline, primary ver-
1327 tex reconstruction, electron and photon identification, muon reconstruction, τ iden-
1328 tification, and b-tagging. After full reconstruction, data sets are made available for
1329 offline analyses.

1330

1331 During the 2016-2017 technical stop, the L1 system was updated in order to improve
1332 the physics object identification by improving the algorithms and accounting for the
1333 increasing pile-up scenario.

1334 **3.3.9 CMS computing**

1335 After the data, coming from the experiment, are processed at several levels, they have
1336 to be stored and made available for further analysis; in order to cope all the tasks
1337 implied in the offline data processing, like transfer, simulation, reconstruction and
1338 reprocessing, among others, a big computing power is required. The CMS computing
1339 system is based on the distributed architecture concept, where users of the system
1340 and physical computer centers are distributed worldwide and interconnected by high-
1341 speed networks.

1342 The worldwide LHC computing grid (WLCG) is the mechanism used to provide that
1343 distributed environment. WLCG is a tiered structure connecting computing centers
1344 around the world, which provides the necessary storage and computing facilities. The

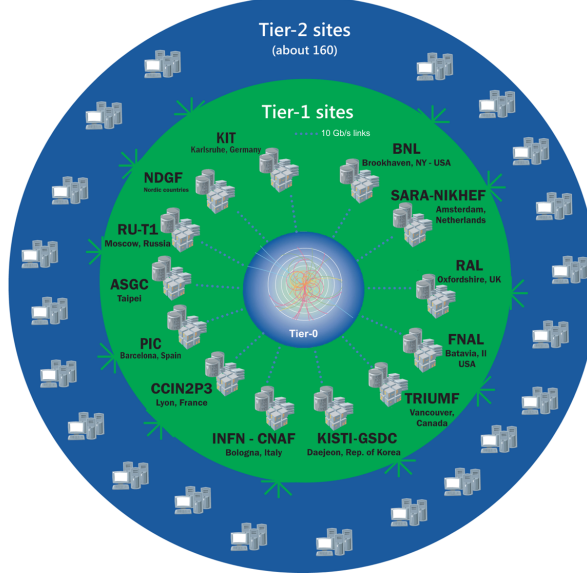


Figure 3.18: WLCG structure. The primary computer centers (Tier-0) are located at CERN (data center) and at the Wigner datacenter in Budapest. Tier-1 is composed of 13 centers and Tier-2 is composed of about 160 centers. [78].

1345 primary computing centers of the WLCG are located at the CERN and the Wigner
 1346 datacenter in Budapest and are known as Tier-0 as shown in figure 3.18. The main
 1347 responsibilities for each tier level are [78]

- 1348 • **Tier-0:** initial reconstruction of recorded events and storage of the resulting
 datasets, the distribution of raw data to the Tier-1 centers.
- 1350 • **Tier-1:** provide storage capacity, support for the Grid, safe-keeping of a pro-
 portional share of raw and reconstructed data, large-scale reprocessing and safe-
 keeping of corresponding output, generation of simulated events, distribution
 of data to Tier 2s, safe-keeping of a share of simulated data produced at these
 Tier 2s.
- 1355 • **Tier-2:** store sufficient data and provide adequate computing power for specific
 analysis tasks, provide analysis requirements and proportional share of simu-
 lated event production and reconstruction.

1358 Aside from the general computing strategy to manage the huge amount of data pro-
1359 duced by experiments, CMS uses a framework to perform a variety of processing,
1360 selection and analysis tasks. The central concept of the CMS data model referred to
1361 as “event data model” (EDM) is the “Event”; therefore, an event is the unit that con-
1362 tains the information from a single bunch crossing as well as any data derived from
1363 that information like the reconstructed objects, the details under which additional
1364 data are derived.

1365

1366 Events are passed as the input to the “physics modules” that obtain information from
1367 them and create new one; for instance, “event data producers” add new data into the
1368 events, “analyzers” produce an information summary from an event set, “filters” per-
1369 form selection and triggering.

1370

1371 CMS uses several event formats with different levels of detail and precision

1372 • **Raw format:** events in this format contain the full recorded information from
1373 the detector as well as trigger decision and other metadata. An extended version
1374 of raw data is used to store information from the CMS Monte Carlo simulation
1375 tools. Raw data are stored permanently, occupying about 2MB/event

1376 • **RECO format:** events in this format correspond to raw data that have been
1377 submitted to reconstruction algorithms like primary and secondary vertex re-
1378 construction, particle ID, track-finding. RECO events contain physical objects
1379 and all the information used to reconstruct them; average size is about 0.5
1380 MB/event.

1381 • **AOD format:** Analysis Object Data (AOD) is the data format used in the
1382 physics analyses given that it contains the parameters describing the high-level

1383 physics objects in addition to enough information to allow a kinematic refitting if
 1384 needed. AOD events are filtered versions of the RECO events to which skimming
 1385 or other kind processes have been applied. Requires about 100 kB/event.

1386 • **Non-event data** are data needed to interpret and reconstruct events. Some
 1387 of the non-event data used by CMS contains information about the detector
 1388 contraction and condition data like calibrations, alignment, and detector status.

1389 Figure 3.19 shows the data flow scheme between CMS detector and hardware tiers.

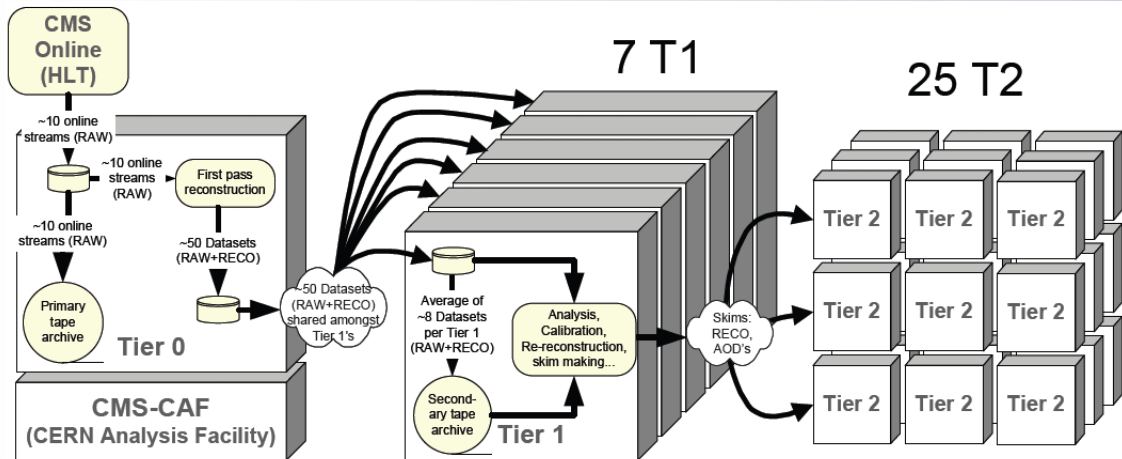


Figure 3.19: Data flow from CMS detector through hardware Tiers.

1390 The whole collection of software built as a framework is referred to as “CMSSW”. This
 1391 framework provides the services needed by the simulation, calibration and alignment,
 1392 and reconstruction modules that process event data, so that physicists can perform
 1393 analysis. The CMSSW event processing model is composed of one executable, called
 1394 cmsRun, and several plug-in modules which contains all the tools (calibration, recon-
 1395 struction algorithms) needed to process an event. The same executable is used for
 1396 both detector and Monte Carlo data [79].

1397 **Chapter 4**

1398 **Event generation, simulation and
1399 reconstruction**

1400 The process of analyzing the data recorded by the CMS experiment involves several
1401 stages where the data are processed in order to interpret the information provided by
1402 all the detection systems; in those stages, the particles produced after the pp collision
1403 are identified by reconstructing their trajectories and measuring their features. In
1404 addition, the SM provides a set of predictions that have to be compared with the
1405 experimental results; however, in most of the cases, theoretical predictions are not
1406 directly comparable to experimental results due to the diverse source of uncertainties
1407 introduced by the experimental setup and theoretical approximations among others.

1408

1409 The strategy to face these conditions consist in using statistical methods implemented
1410 in computational algorithms to produce numerical results that can be contrasted with
1411 the experimental results. These computational algorithms are commonly known as
1412 Monte Carlo (MC) methods and, in the case of particle physics, they are designed to
1413 apply the SM rules and produce predictions about the physical observables measured

in the experiments. Since particle physics is governed by quantum mechanics principles, predictions are not allowed for single events; therefore, a high number of events are “generated” and predictions are produced in the form of statistical distributions for the observables. Effects of the detector presence are included in the predictions by introducing simulations of the detector itself.

1419

1420 This chapter presents a description of the event generation strategy and the tools
 1421 used to perform the detector simulation and physics objects reconstruction. A comprehensive review of event generators for LHC physics can be found in reference [80]
 1422 on which this chapter is based.

1424 4.1 Event generation

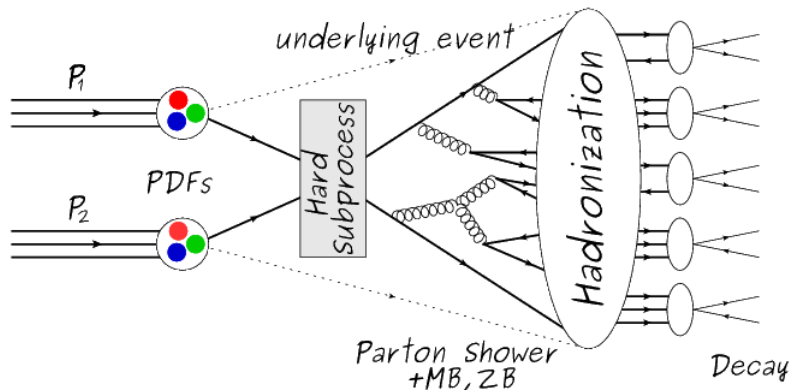


Figure 4.1: Event generation process. In the first step, the PDF of the colliding particles is considered so the specific interaction is described. The actual interaction is generated in the hard subprocess; the cross-section of the process is calculated from the matrix element connecting the initial and final states. The parton shower describes the evolution of the partons from the hard subprocess according to the DGLAP equations. At this step, the underlying event and PU effects are included in the generation. The resulting partons from the parton shower are recombined to form hadrons in the hadronization step; most of them are unstable, therefore, their decays are also generated in agreement to the known branching ratios. Modified from reference [81].

1425 The event generation is intended to create events that mimic the behavior of actual
 1426 events produced in the collisions; they obey a sequence of steps from the particles colli-
 1427 sion hard process to the decay process into the final state particles. Figure 4.1 shows
 1428 a schematic view of the event generation process; the fact that the full process can
 1429 be treated as several independent steps is based on the QCD factorization theorem.

1430

1431 Generation starts by taking into account the PDFs of the incoming particles. Event
 1432 generators offer the option to choose from several PDF sets depending on the partic-
 1433 ular process under simulation¹; in the following pp collisions will be considered. The
 1434 *hard subprocess* describes the actual interaction between partons from the incoming
 1435 protons; it is represented by the matrix element connecting the initial and final states
 1436 of the interaction. Normally, the matrix element can be written as a sum over Feyn-
 1437 man diagrams and consider interferences between terms in the summation. During
 1438 the generation of the hard subprocess, the production cross section is calculated.

1439

1440 The order to which the cross section is calculated depends on the order of the Feyn-
 1441 man diagrams involved in the calculation; therefore, radiative corrections are included
 1442 by considering a higher order Feynman diagrams where QCD radiation dominates.
 1443 Currently, cross sections calculated to LO do not offer a satisfactory description of the
 1444 processes, i.e., the results are only reliable for the shape of distributions; therefore,
 1445 NLO calculations have to be performed with the implication that the computing time
 1446 needed is highly increased.

1447

1448 The final parton content of the hard subprocess is subjected to the *parton shower*
 1449 which generates the gluon radiation. Parton shower evolves the partons; i.e., gluons

¹ Tool in Reference [82] allows to plot different PDF sets under customizable conditions.

1450 split into quark-antiquark pairs and quarks of enough energy radiate gluons giving rise
 1451 to further parton multiplication, following the DGLAP (Dokshitzer-Gribov-Lipatov-
 1452 Altarelli-Parisi) equations. Showering continues until the energy scale is low enough
 1453 to reach the non-perturbative limit.

1454

1455 In the simulation of LHC processes that involve b quarks like the single top quark or
 1456 Higgs associated production, it is needed to consider that the b quark is heavier than
 1457 the proton; in this sense, the QCD interaction description is made in two different
 1458 schemes [83]

1459 • four-flavor (4F) scheme. b quarks appear only in the final state because they
 1460 are heavier than the proton and therefore they can be produced only from the
 1461 splitting of a gluon into pairs or singly in association with a t quark in high
 1462 energy-scale interactions. During the simulation, the b -PDFs are set to zero
 1463 because it cannot be part of the proton. Calculations in this scheme are more
 1464 complicated due to the presence of the second b quark but the full kinematics is
 1465 considered already at LO and therefore the accuracy of the description is better.

1466 • five-flavor (5F) scheme. b quarks are considered massless, therefore they can
 1467 appear in both initial and final states since it can now be part of the proton; thus,
 1468 during the simulation b -PDFs are not set to zero. In this scheme, calculations
 1469 are simpler than in the 4F scheme and possible logarithmic divergences are
 1470 absorbed by the PDFs through the DGLAP evolution.

1471 In this thesis, the tHq events are generated using the 4F scheme in order to reduce
 1472 uncertainties, while the tHW events are generated using the 5F scheme to eliminate
 1473 LO interference with the $t\bar{t}H$ process [48].

1474

1475 Partons involved in the pp collision are the focus of the simulation, however, the rest
 1476 of the partons inside the incoming protons are also affected because the remnants are
 1477 colored objects; also, multiple parton interactions can occur. The hadronization of
 1478 the remnants and multiple parton interactions are known as “underlying event” and
 1479 it has to be included in the simulation. In addition, multiple pp collisions in the same
 1480 bunch crossing (pile-up mentioned in 3.2) occurs, actually in two forms

- 1481 • *in-time PU* which refers to multiple pp collision in the bunch crossing but that
 1482 are not considered as primary vertices.
- 1483 • *Out-of-time PU* which refers to overlapping pp collisions from consecutive bunch
 1484 crossings; this can occurs due to the time-delays in the detection systems where
 1485 information from one bunch crossing is assigned to the next or previous one.

1486 While the underlying event effects are included in generation using generator-specific
 1487 tools, PU effects are added to the generation by overlaying Minimum-bias (MB) and
 1488 Zero-bias (ZB) events to the generated events. MB events are inelastic events selected
 1489 by using a loose (minimum bias) trigger with as little bias as possible, therefore ac-
 1490 cepting a large fraction of the overall inelastic event; ZB events correspond to random
 1491 events recorded by the detector when collisions are likely. MB model in-time PU and
 1492 ZB model out-of-time PU.

1493

1494 The next step in the generation process is called “hadronization”. Since particles
 1495 with a net color charge are not allowed to exits isolated, they have to recombine
 1496 to form bound states. This is precisely the process by which the partons resulting
 1497 from the parton shower arrange themselves as color singlets to form hadrons. At
 1498 this step, the energy-scale is low and the strong coupling constant is large, there-
 1499 fore hadronization process is non-perturbative and the evolution of the partons is

1500 described using phenomenological models. Most of the baryons and mesons produced
 1501 in the hadronization are unstable and hence they will decay in the detector.

1502

1503 The last step in the generation process corresponds to the decay of the unstable
 1504 particles generated during hadronization; it is also simulated in the hadronization
 1505 step, based on the known branching ratios.

1506 4.2 Monte Carlo Event Generators.

1507 The event generation described in the previous section has been implemented in
 1508 several software packages for which a brief description is given.

- 1509 • **PYTHIA 8.** It is a program designed to perform the generation of high en-
 1510 ergy physics events which describe the collisions between particles such as elec-
 1511 trons, protons. Several theories and models are implemented in it, in order to
 1512 describe physical aspects like hard and soft interaction, parton distributions,
 1513 initial and final-state parton showers, multiple parton interactions, beam rem-
 1514 nants, hadronization² and particle decay. Thanks to extensive testing, several
 1515 optimized parametrizations, known as “tunings”, have been defined in order
 1516 to improve the description of actual collisions to a high degree of precision; for
 1517 analysis at $\sqrt{s} = 13$ TeV, the underline event CUETP8M1 tune is employed [85].
 1518 The calculation of the matrix element is performed at LO which is not enough
 1519 for the current required level of precision; therefore, pythia is often used for
 1520 parton shower, hadronization and decays, while other event generators are used
 1521 to generate the matrix element at NLO.

² based in the Lund string model [84]

1522 • **MadGraph5_aMC@NLO.** MadGraph is a matrix element generator which
 1523 calculates the amplitudes for all contributing Feynman diagrams of a given pro-
 1524 cess but does not provide a parton shower while MC@NLO incorporate NLO
 1525 QCD matrix elements consistently into a parton shower framework; thus, Mad-
 1526 Graph5_aMC@NLO, as a merger of the two event generators MadGraph5 and
 1527 aMC@NLO, is an event generator capable to calculate tree-level and NLO cross
 1528 sections and perform the matching of those with the parton shower. It is one of
 1529 the most frequently used matrix element generators; however, it has the partic-
 1530 ular feature of the presence of negative event weights which reduce the number
 1531 of events used to reproduce the properties of the objects generated [86].

1532

1533 • **POWHEG.** It is an NLO matrix element generator where the hardest emis-
 1534 sion of color charged particles is generated in such a way that the negative event
 1535 weights issue of MadGraph5_aMC@NLO is overcome; however, the method re-
 1536 quires an interface with p_T -ordered parton shower or a parton shower generator
 1537 where this highest emission can be vetoed in order to avoid double counting of
 1538 this highest-energetic emission. PYTHIA is a commonly matched to POWHEG
 1539 event generator [87].

1540 Events resulting from the whole generation process are known as MC events.

1541 4.3 CMS detector simulation.

1542 After generation, MC events contain the physics of the collisions but they are not
 1543 ready to be compared to the events recorded by the experiment since these recorded
 1544 events correspond to the response of the detection systems to the interaction with

1545 the particles traversing them. The simulation of the CMS detector has to be applied
1546 on top of the event generation; it is simulated with a MC toolkit for the simulation
1547 of particles passing through matter called Geant4 which is also able to simulate the
1548 electronic signals that would be measured by all detectors inside CMS.

1549

1550 The simulation takes the generated particles contained in the MC events as input,
1551 makes them pass through the simulated geometry, and models physics processes that
1552 particles experience during their passage through matter. The full set of results from
1553 particle-matter interactions correspond to the simulated hit which contains informa-
1554 tion about the energy loss, momentum, position. Particles of the input event are
1555 called “primary”, while the particles originating from GEANT4-modeled interactions
1556 of a primary particle with matter are called a “secondary”. Simulated hits are the in-
1557 put of subsequent modules that emulate the response of the detector readout system
1558 and triggers. The output from the emulated detection systems and triggers is known
1559 as digitization [88, 89].

1560

1561 The modeling of the CMS detector corresponds to the accurate modeling of the
1562 interaction among particles, the detector material, and the magnetic field. This
1563 simulation procedure includes the following standard steps

- 1564 • Modeling of the Interaction Region.
- 1565 • Modeling of the particle passage through the hierarchy of volumes that compose
1566 CMS detector and of the accompanying physics processes.
- 1567 • Modeling of the effect of multiple interactions per beam crossing and/or the
1568 effect of events overlay (Pile-Up simulation).

1569 • Modeling of the detector’s electronics response, signal shape, noise, calibration
 1570 constants (digitization).

1571 In addition to the full simulation, i.e. a detailed detector simulation, a faster simula-
 1572 tion (FastSim) have been developed, that may be used where much larger statistics
 1573 are required. In FastSim, detector material effects are parametrized and included in
 1574 the hits; those hits are used as input of the same higher-level algorithms³ used to an-
 1575 alyze the recorded events. In this way, comparisons between fast and full simulations
 1576 can be performed [91].

1577

1578 After the full detector simulation, the output events can be directly compared with
 1579 events actually recorded in the CMS detector. The collection of MC events that
 1580 reproduce the expected physics for a given process are known as MC samples.

1581 **4.4 Event reconstruction.**

1582 In contrast to MC samples for which all the particles’ information is available from
 1583 it’s identity to its mass and energy, recorded events contain the electronic signals,
 1584 provided by the CMS detection systems, encoding the interaction of physical parti-
 1585 cles with the detector matter; these electronic signals have to be combined in order
 1586 to identify these particles and measure their features i.e., particles have to be “recon-
 1587 structed” using the signals provided by the detection systems. The CMS experiment
 1588 use the “particle-flow event reconstruction algorithm (PF)” to do the reconstruction
 1589 of particles produced in pp collisions. Next sections will present a basic description

³ track fitting, calorimeter clustering, b tagging, electron identification, jet reconstruction and calibration, trigger algorithms which will be considered in the next sections

1590 of the *Elements* used by PF (tracker tracks, energy clusters, and muon tracks), based
 1591 in the references [92, 93] where more detailed descriptions can be found.

1592 **4.4.1 Particle-Flow Algorithm.**

1593 Each of the several sub detection systems of the CMS detector is dedicated to identi-
 1594 fying a specific type of particles, i.e., photons and electrons are absorbed by the ECAL
 1595 and their reconstruction is based on ECAL information; hadrons are reconstructed
 1596 from clusters in the HCAL while muons are reconstructed from hits in the muon
 1597 chambers. PF is designed to correlate signals from all the detector layers (tracks and
 1598 energy clusters) in order to reconstruct and identify each final state particle and its
 1599 properties as sketched in figure 4.2.

1600

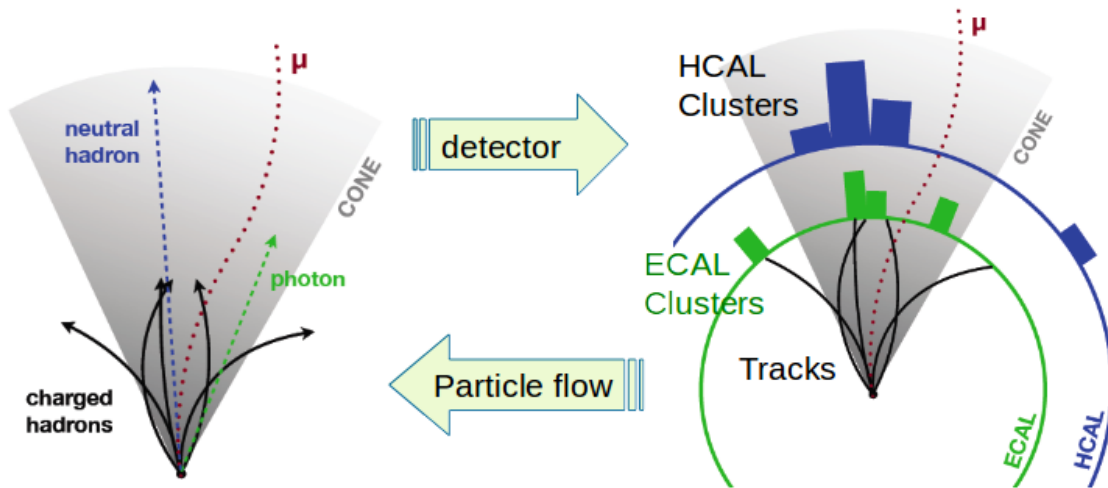


Figure 4.2: Particle flow algorithm. Information from the several CMS detection systems if provided as input to the algorithm which then combine it to identify and reconstruct all the particles in the final state and their properties. Reconstruction of simulated events is also performed by providing information from MC samples, detector and trigger simulation [94].

1601 For instance, a charged hadron is identified by a geometrical connection, know as *link*
 1602 between one or more calorimeter clusters and a track in the tracker provided there

1603 are no hits in the muon system; combining several measurements allows a better
 1604 determination of the energy and charge sign of the charged hadron.

1605 **Charged-particle track reconstruction.**

1606 The strategy used by PF in order to reconstruct tracks is called “Iterative Tracking”
 1607 which occurs in four steps

- 1608 • Seed generation where initial track candidates are found by looking for a combi-
 1609 nation of hits in the pixel detector, strip tracker, and muon chambers. In total
 1610 ten iterations are performed, each one with a different seeding requirement.
 1611 Seeds are used to estimate the trajectory parameters and uncertainties at the
 1612 time of the full track reconstruction. Seeds are also considered track candidates.

- 1613 • Track finding using a tracking software known as Combinatorial Track Finder
 1614 (CTF) [95]. The seed trajectories are extrapolated along the expected flight
 1615 path of a charged particle, in agreement to the trajectory parameters obtained
 1616 in the first step, in an attempt to find additional hits that can be assigned to
 1617 the track candidates.

- 1618 • Track-fitting where the found tracks are passed as input to a module which
 1619 provides the best estimate of the parameters of each trajectory.

- 1620 • Track selection where track candidates are submitted to a selection which dis-
 1621 cards those that fail a set of defined quality criteria.

1622 Iterations differ in the seeding configuration and the final track selection as elaborated
 1623 in references [92, 93]. In the first iteration, high p_T tracks and tracks produced near
 1624 to the interaction region are identified and those hits are masked thereby reducing
 1625 the combinatorial complexity. Next iterations search for more complicated tracks,

1626 like low p_T tracks and tracks from b hadron decays, which tend to be displaced from
 1627 the interaction region.

1628 **Vertex reconstruction.**

1629 During the track reconstruction, an extrapolation toward to the calorimeters is per-
 1630 formed in order to match energy deposits; that extrapolation is performed also toward
 1631 the beamline in order to find the origin of the track known as *vertex*. The vertex re-
 1632 construction is performed by selecting from the available reconstructed tracks, those
 1633 that are consistent with being originated in the interaction region where pp collisions
 1634 are produced. The selection involves a requirement on the number of tracker (pixel
 1635 and strip) hits and the goodness of the track fit.

1636

1637 Selected tracks are clustered using a “deterministic annealing algorithm (DA)”⁴. A
 1638 set of candidate vertices and their associated tracks, resulting from the DA, are then
 1639 fitted with an “adaptive vertex fitter (AVF)” to produce the best estimate of the
 1640 vertices locations.

1641

1642 The p_T of the several tracks associated to a reconstructed vertex is added, squared and
 1643 used to organize the vertices; the vertex with the highest squared sum is designated
 1644 as the *primary vertex (PV)* while the rest are designated as PU vertices.

1645 **Calorimeter clustering.**

1646 After traversing the CMS tracker system, electrons, photons and hadrons deposit their
 1647 energy in the ECAL and HCAL cells. The PF clustering algorithm aims to provide
 1648 a high detection efficiency even for low-energy particles and an efficient distinction

⁴ DA algorithm and AVF are described in detail in references [97,98]

1649 between close energy deposits. The clustering runs independently in the ECAL barrel
 1650 and endcaps, HCAL barrel and endcaps, and the two preshower layers, following two
 1651 steps

- 1652 • cells with an energy larger than a given seed threshold and larger than the energy
 1653 of the neighboring cells are identified as cluster seeds. The neighbor cells are
 1654 those that either share a side with the cluster seed candidate, or the eight closest
 1655 cells including cells that only share a corner with the seed candidate.
- 1656 • cells with at least a corner in common with a cell already in the cluster seed
 1657 and with an energy above a cell threshold are grouped into topological clusters.

1658 Clusters formed in this way are known as *particle-flow clusters*. With this clustering
 1659 strategy, it is possible to detect and measure the energy and direction of photons and
 1660 neutral hadrons as well as differentiate these neutral particles from the charged hadron
 1661 energy deposits. In cases involving charged hadrons for which the track parameters
 1662 are not determined accurately, for instance, low-quality and high- p_T tracks, clustering
 1663 helps in the energy measurements.

1664 **Electron track reconstruction.**

1665 Although the charged-particle track reconstruction described above works for elec-
 1666 trons, they lose a significant fraction of their energy via bremsstrahlung photon radi-
 1667 ation before reaching the ECAL; thus, the reconstruction performance depends on the
 1668 ability to measure also the radiated energy. The reconstruction strategy, in this case,
 1669 requires information from the tracking system and from the ECAL. Bremsstrahlung
 1670 photons are emitted at similar η values to that of the electron but at different values
 1671 of ϕ ; therefore, the radiated energy can be recovered by grouping ECAL clusters in a
 1672 η window over a range of ϕ around the electron direction. The group is called ECAL

1673 supercluster.

1674

1675 Electron candidates from the track-seeding and ECAL super clustering are merged
 1676 into a single collection which is submitted to a full electron tracking fit with a
 1677 Gaussian-sum filter (GSF) [96]. The electron track and its associated ECAL su-
 1678 percluster form a *particle-flow electron*.

1679 **Muon track reconstruction.**

1680 Given that the CMS detector is equipped with a muon spectrometer capable to iden-
 1681 tify and measure the momentum of the muons traversing it, the muon reconstruction
 1682 is not specific to PF; therefore, three different muon types are defined

- 1683 • *Standalone muon.* A clustering on the DTs or CSCs hits is performed to form
 1684 track segments; those segments are used as seeds for the reconstruction in the
 1685 muon spectrometer. All DTs, CSCs, and RPCs hits along the muon trajectory
 1686 are combined and fitted to form the full track. The fitting output is called a
 1687 *standalone-muon track*.
- 1688 • *tracker muon.* Each track in the inner tracker with p_T larger than 0.5 GeV and
 1689 a total momentum p larger than 2.5 GeV is extrapolated to the muon system. A
 1690 *tracker muon track* corresponds to the extrapolated tracks that match at least
 1691 one muon segment.
- 1692 • *Global muon.* When tracks in the inner tracker (inner tracks) and standalone-
 1693 muon tracks are matched and turn out being compatibles, their hits are com-
 1694 bined and fitted to form a *global-muon track*.

1695 Global muons sharing the same inner track with tracker muons are merged into a
 1696 single candidate. PF muon identification uses the muon energy deposits in ECAL,
 1697 HCAL, and HO associated with the muon track to improve the muon identification.

1698 **Particle identification and reconstruction.**

1699 PF elements are connected by a linker algorithm that tests the connection between any
 1700 pair of elements; if they are found to be linked, a geometrical distance that quantifies
 1701 the quality of the link is assigned. Two elements may be linked indirectly through
 1702 common elements. Linked elements form *PF blocks* and a PF block may contain
 1703 elements originating in one or more particles. Links can be established between
 1704 tracks, between calorimeter clusters, and between tracks and calorimeter clusters.
 1705 The identification and reconstruction start with a PF block and proceeds as follows

1706 • Muons. An “isolated global muon” is identified by evaluating the presence of
 1707 inner track and energy deposits close to the global muon track in the (η, ϕ)
 1708 plane, i.e., in a particular point of the global muon track, inner tracks and
 1709 energy deposits are sought within a radius of $\Delta R = 0.3$ (see eqn. 3.7) from the
 1710 muon track; if they exist and the p_T of the found track added to the E_T of the
 1711 found energy deposit does not exceed 10% of the muon p_T then the global muon
 1712 is an isolated global muon. This isolation condition is stringent enough to reject
 1713 hadrons misidentified as muons.

1714 “Non-isolated global muons” are identified using additional selection require-
 1715 ments on the number of track segments in the muon system and energy deposits
 1716 along the muon track. Muons inside jets are identified with more stringent crite-
 1717 ria in isolation and momentum as described in reference [99]. The PF elements
 1718 associated with an identified muon are masked from the PF block.

- 1719 ● Electrons are identified and reconstructed as described above plus some addi-
 1720 tional requirements on fourteen variables like the amount of energy radiated,
 1721 the distance between the extrapolated track position at the ECAL and the po-
 1722 sition of the associated ECAL supercluster among others, which are combined
 1723 in a specialized multivariate analysis strategy that improves the electron iden-
 1724 tification. Tracks and clusters used to identify and reconstruct electrons are
 1725 masked in the PF block.

- 1726 ● Isolated photons are identified from ECAL superclusters with E_T larger than 10
 1727 GeV, for which the energy deposited at a distance of 0.15, from the supercluster
 1728 position on the (η, ϕ) plane, does not exceed 10% of the supercluster energy;
 1729 note that this is an isolation requirement. In addition, there must not be links
 1730 to tracks. Clusters involved in the identification and reconstruction are masked
 1731 in the PF block.

- 1732 ● Bremsstrahlung photons and prompt photons tend to convert to electron-positron
 1733 pairs inside the tracker, therefore, a dedicated finder algorithm is used to link
 1734 tracks that seem to originate from a photon conversion; in case those two tracks
 1735 are compatible with the direction of a bremsstrahlung photon, they are also
 1736 linked to the original electron track. Photon conversion tracks are also masked
 1737 in the PF block.

- 1738 ● The remaining elements in the PF block are used to identify hadrons. In the
 1739 region $|\eta| \leq 2.5$, neutral hadrons are identified with HCAL clusters not linked
 1740 to any track while photons from neutral pion decays are identified with ECAL
 1741 clusters without links to tracks. In the region $|\eta| > 2.5$ ECAL clusters linked to
 1742 HCAL clusters are identified with a charged or neutral hadron shower; ECAL
 1743 clusters with no links are identified with photons. HCAL clusters not used yet,

1744 are linked to one or more unlinked tracks and to an unlinked ECAL in order to
 1745 reconstruct charged-hadrons or a combination of photons and neutral hadrons
 1746 according to certain conditions on the calibrated calorimetric energy.

- 1747 • Charged-particle tracks may be liked together when they converge to a “sec-
 1748 ondary vertex (SV) ” displaced from the interaction point where the PV and
 1749 PU vertices are reconstructed; at least three tracks are needed in that case,
 1750 of which at most one has to be an incoming track with hits in tracker region
 1751 between a PV and the SV.

1752

1753 The linker algorithm, as well as the whole PF algorithm, has been validated and
 1754 commissioned; results from that validation are presented in the references [92].

1755 **Jet reconstruction.**

1756 Quarks and gluons may be produced in the pp collisions, therefore, their hadronization
 1757 will be seen in the detector as a shower of hadrons and their decay products in the
 1758 form of a “jet”. The anti- k_t algorithm [100] is used to perform the jet reconstruction
 1759 by clustering those PF particles within a cone (see figure 4.3); previously, isolated
 1760 electrons, isolated muons, and charged particles associated with other interaction
 1761 vertices are excluded from the clustering.

1762 The anti- k_t algorithm proceeds in a sequential recombination of PF particles; the
 1763 distance between particles i and j (d_{ij}) and the distance between particles and the
 1764 beam are defined as

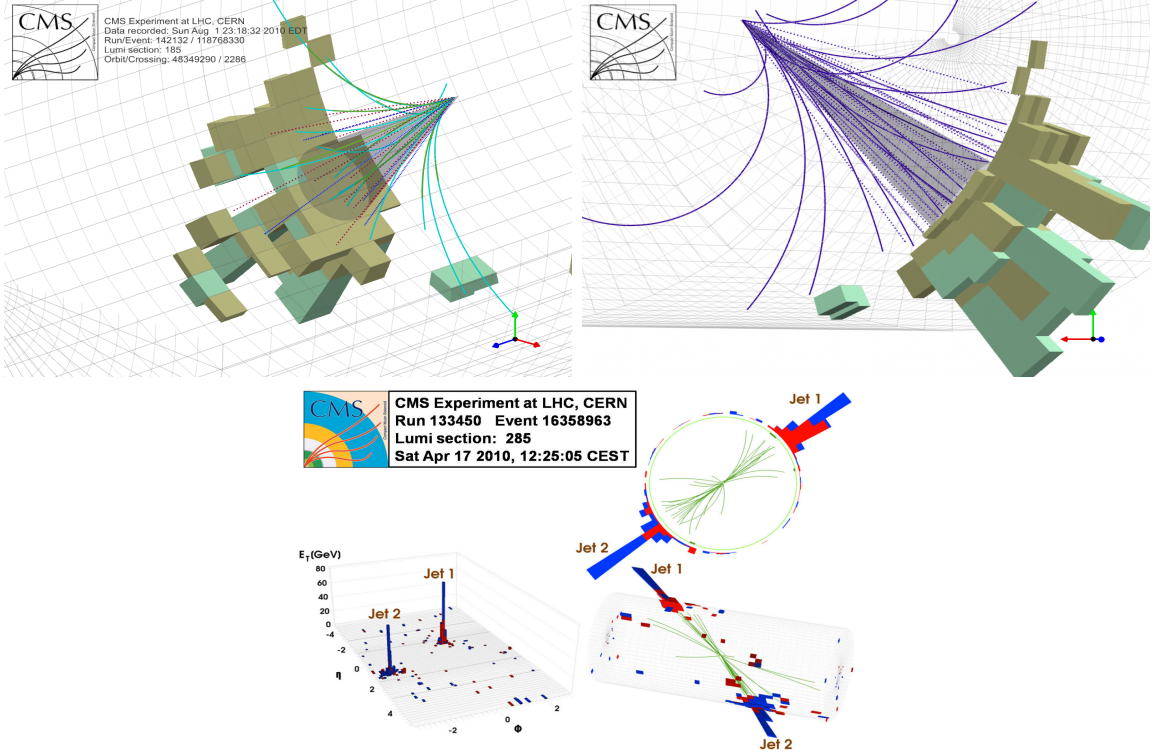


Figure 4.3: Jet reconstruction performed by the anti- k_t algorithm. Top: Two different views of a CMS recorded event are presented. Continuous lines correspond to the tracks left by charged particles in the tracker while dotted lines are the imaginary paths followed by neutral particles. The green cubes represent the ECAL cells while the blue ones represent the HCAL cells; in both cases, the height of the cube represent the amount of energy deposited in the cells [101]. Bottom: Reconstruction of a recorded event with two jets [102].

$$d_{ij} = \min\left(\frac{1}{k_{ti}^2}, \frac{1}{k_{tj}^2}\right) \frac{\Delta_{ij}^2}{R^2}$$

$$d_{iB} = \frac{1}{k_{ti}^2} \quad (4.1)$$

where $\Delta_{ij}^2 = (y_i - y_j)^2 + (\phi_i - \phi_j)^2$, k_{ti} , y_i and ϕ_i are the transverse momentum, rapidity and azimuth of particle i respectively and R is the called jet radius. For all the remaining PF particles, after removing the isolated ones, d_{ij} and d_{iB} are calcu-

1768 lated⁵ and the smallest is identified; if it is a d_{ij} , particles i and j are replaced with
 1769 a new object whose momentum is the vectorial sum of the combined particles. If the
 1770 smallest distance is a d_{iB} the clustering process ends, the object i (which at this stage
 1771 should be a combination of several PF particles) is declared as a *Particle-flow-jet* (PF
 1772 jet) and all the associated PF particles are removed from the detector. The clustering
 1773 process is repeated until no PF particles remain.

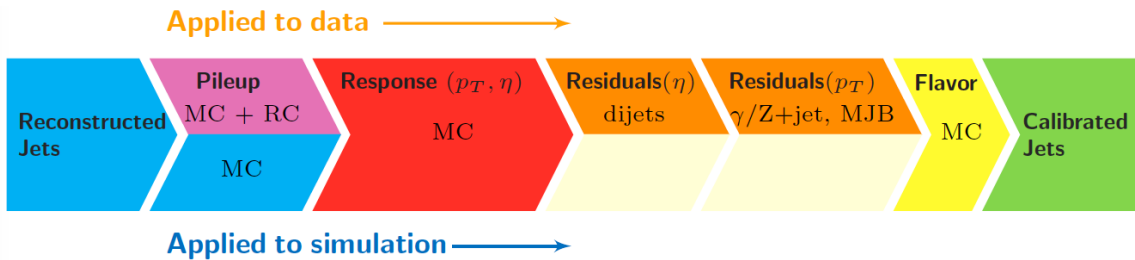


Figure 4.4: Jet energy correction diagram. Correction levels are applied sequentially in the indicated fixed order [104].

Even though jets can be reconstructed efficiently, there are some effects that are not included in the reconstruction and that lead to discrepancies between the reconstructed results and the predicted results; in order to overcome these discrepancies, a factorized model has been designed in the form of jet energy corrections (JEC) [103, 104] applied sequentially as shown in the diagram of figure 4.4.

At each level, the jet four-momentum is multiplied by a scaling factor based on jet properties, i.e., η , flavor, etc.

- 1781 • Level 1 correction removes the energy coming from pile-up. The scale factor is
1782 determined using a MC sample of QCD dijet events with and without pileup
1783 overlay; it is parametrized in terms of the offset energy density ρ , jet area A ,
1784 jet η and jet p_T . Different corrections are applied to data and MC due to the
1785 detector simulation.

⁵ Notice that this is a combinatorial calculation.

- 1786 • MC-truth correction accounts for differences between the reconstructed jet en-
- 1787 ergy and the MC particle-level energy. The correction is determined on a QCD
- 1788 dijet MC sample and is parametrized in terms of the jet p_T and η .
- 1789 • Residuals correct remaining small differences within jet response in data and
- 1790 MC. The Residuals η -dependent correction compares jets of similar p_T in the
- 1791 barrel reference region. The Residuals p_T -dependent correct the jet absolute
- 1792 scale (JES vs p_T).
- 1793 • Jet-flavor corrections are derived in the same way as MC-truth corrections but
- 1794 using QCD pure flavor samples.

1795 ***b*-tagging of jets.**

1796 A particular feature of the hadrons containing bottom quarks (b-hadrons) is that
 1797 they have a lifetime long enough to travel some distance before decaying, but it is
 1798 not as long as those of light quark hadrons; therefore, when looking at the hadrons
 1799 produced in pp collisions, b-hadrons decay typically inside the tracker rather than
 1800 reach the calorimeters as some light-hadrons do. As a result, a b-hadron decay gives
 1801 rise to a displaced vertex (secondary vertex) with respect to the primary vertex as
 1802 shown in figure 4.5; the SV displacement is in the order of a few millimeters. A jet
 1803 resulting from the decay of a b-hadron is called *b* jet; other jets are called light jets.

1804

1805 Several methods to identify *b*-jets (*b*-tagging) have been developed; the method used in
 1806 this thesis is known as “Combined Secondary Vertex” algorithm in its second version
 1807 (CSVv2) [105]. By using information of the impact parameter, the reconstructed
 1808 secondary vertices and the jet kinematics in a multivariate analysis that combines
 1809 the discrimination power of each variable in one global discriminator variable, three

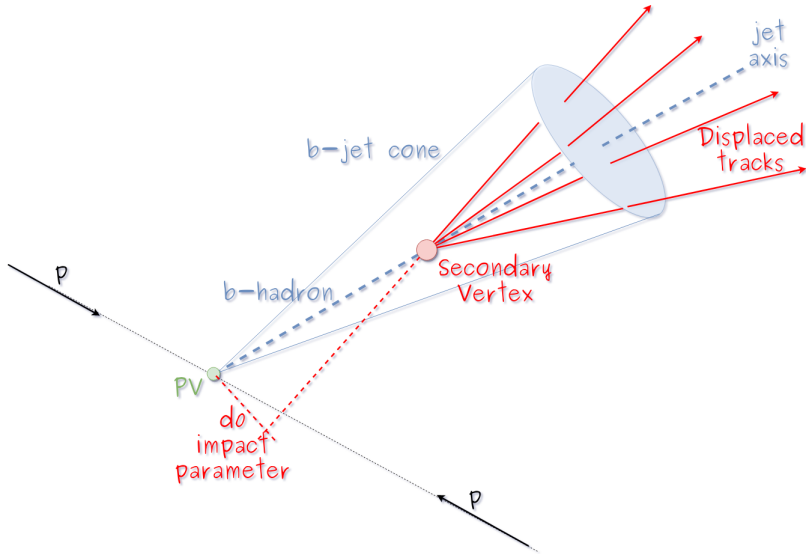


Figure 4.5: Secondary vertex in a b-hadron decay.

1810 working points (references): loose, medium and tight, are defined which quantify the
 1811 probabilities of mistag jets from light quarks as jets from b quarks; 10, 1 and 0.1 %
 1812 respectively. Although the mistagging probability decrease with the working point
 1813 strength, the efficiency to correctly tag b -jets also decrease as 83, 69 and 49 % for the
 1814 respective working point; therefore, a balance needs to be achieved according to the
 1815 specific requirements of the analysis.

1816 Missing transverse energy.

1817 The fact that proton bunches carry momentum along the z axis implies that for each
 1818 event, momentum balance in the transverse plane is expected. Imbalances are quan-
 1819 tified by the missing transverse energy (MET) and are attributed to several sources
 1820 including particles escaping undetected through the beam pipe, neutrinos produced in
 1821 weak interactions processes which do not interact with the detector and thus escaping
 1822 without leaving a sign, or even undiscovered particles predicted by models beyond
 1823 the SM.

1824

1825 The PF algorithm assign the negative sum of the momenta of all reconstructed PF
 1826 particles to the *particle-flow MET* according to

$$\vec{E}_T = - \sum_i \vec{p}_{T,i} \quad (4.2)$$

1827 JEC are propagated to the calculation of the \vec{E}_T as described in the reference [106].

1828

1829 4.4.2 Event reconstruction examples

1830 Figures 4.6-4.8 show the results of the reconstruction performed on 3 recorded events.
 1831 Descriptions are taken directly from the source.

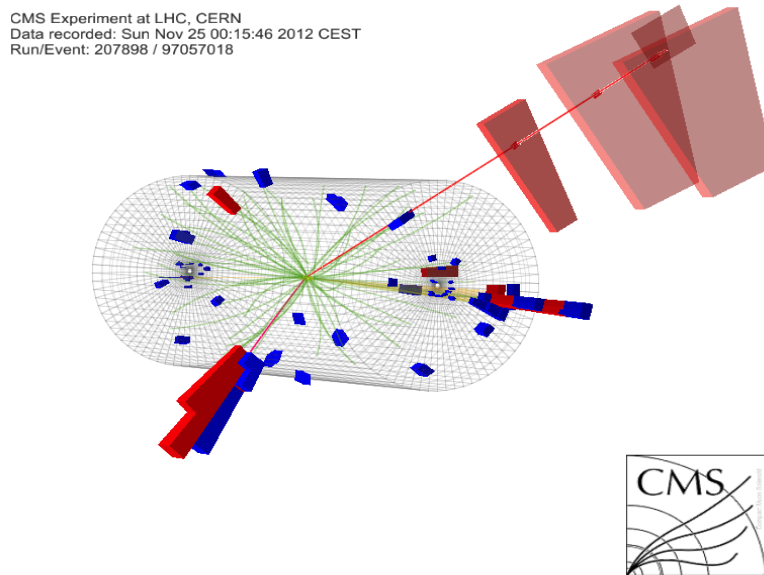


Figure 4.6: HIG-13-004 Event 1 reconstruction results; “HIG-13-004 Event 1: Event recorded with the CMS detector in 2012 at a proton-proton center-of-mass energy of 8 TeV. The event shows characteristics expected from the decay of the SM Higgs boson to a pair of τ leptons. Such an event is characterized by the production of two forward-going jets, seen here in opposite endcaps. One of the τ decays to a muon (red lines on the right) and neutrinos, while the other τ decays into a charged hadron and a neutrino.” [?].

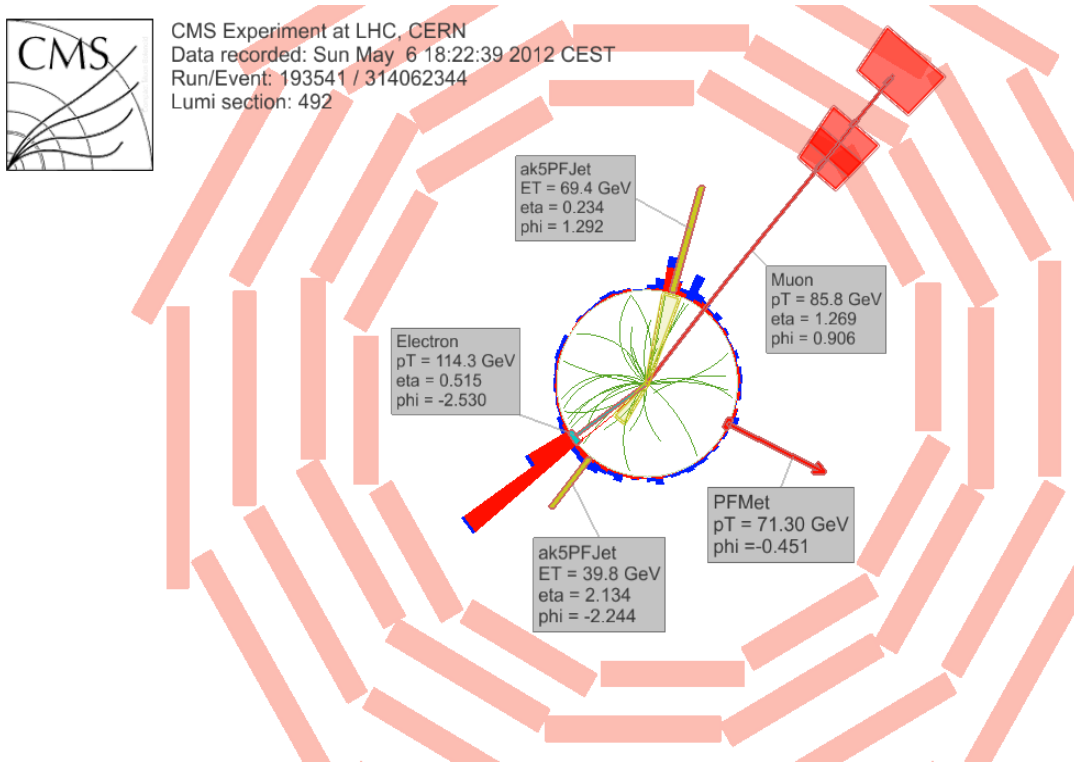


Figure 4.7: $e\mu$ event reconstruction results; “An $e\mu$ event candidate selected in 8 TeV data, as seen from the direction of the proton beams. The kinematics of the main objects used in the event selection are highlighted: two isolated leptons and two particle-flow jets. The reconstructed missing transverse energy is also displayed for reference” [?].

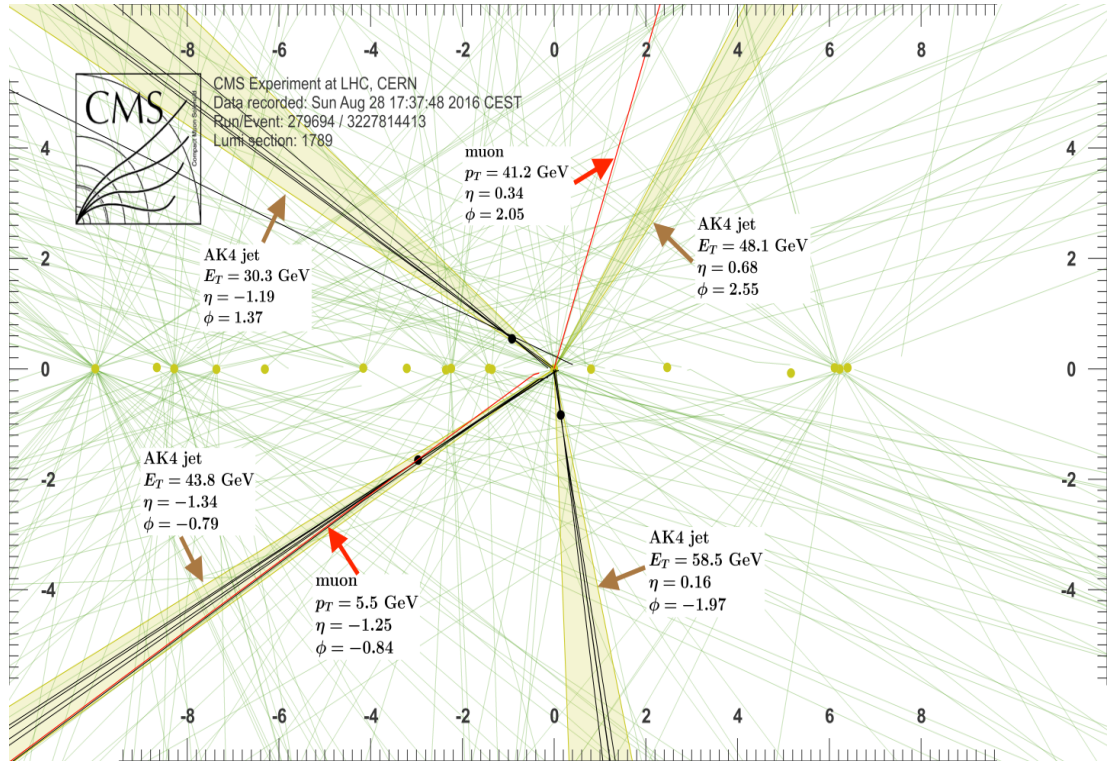


Figure 4.8: Recorded event reconstruction results; “Recorded event (ρ - z projection) with three jets with $p_T > 30$ GeV with one displaced muon track in 2016 data collected at 13 TeV. Each of the three jets has a displaced reconstructed vertex. The jet with $p_T(j) = 43.8$ GeV, $\eta(j) = -1.34$, $\phi(j) = -0.79$ contains muon with $p_T(\mu) = 5.5$ GeV, $\eta(\mu) = -1.25$, $\phi(\mu) = -0.84$. Event contains reconstructed isolated muon with $p_T(\mu) = 41.2$ GeV, $\eta(\mu) = 0.34$, $\phi(\mu) = 2.05$ and MET with $p_T = 72.5$ GeV, $\phi = -0.32$. Jet candidates for a b -jet from top quark leptonic and hadronic decays are tagged by CSVv2T algorithm. One of the other two jets is tagged by CharmT algorithm. Tracks with $p_T > 0.5$ GeV are shown. The number of reconstructed primary vertices is 18. Reconstructed $m_T(W)$ is 101.8 GeV. Beam spot position correction is applied. Reconstructed primary vertices are shown in yellow color, while reconstructed displaced vertices and associated tracks are presented in black color. Dimensions are given in cm” [107].

1832 **Chapter 5**

1833 **Statistical methods**

1834 In the course of analyzing the data sets provided by the CMS experiment and used in
1835 this thesis, several statistical tools have been employed; in this chapter, a description
1836 of these tools will be presented, starting with the general statement of the multivariate
1837 analysis method, followed by the particularities of the Boosted Decision Trees (BDT)
1838 method and its application to the classification problem. Statistical inference methods
1839 used will also be presented. This chapter is based mainly on the references [108, 109].

1840 **5.1 Multivariate analysis**

1841 Multivariate data analysis (MVA) makes reference to statistical techniques that an-
1842 alyze data containing information of more than one variable, commonly taking into
1843 account the effects of all variables on the response of the particular variable under
1844 investigation, i.e., considering all the correlations between variables. MVA is em-
1845 ployed in a variety of fields like consumer and market research, quality control and
1846 process optimization. From a MVA it is possible to identify the dominant patterns
1847 in the data, like groups, outliers and trends, and determine to which group a set of

1848 values belong; in the particle physics context, MVA methods are used to perform the
 1849 selection of certain type of events, from a large data set, using a potentially large
 1850 number of measurable properties for each event.

1851 Processes with small cross section, as the tHq process, normally are hidden behind
 1852 more common processes; therefore, the data set results in a subset of events with
 1853 characteristic features of interest (signal) mixed in randomly with a much larger
 1854 number of SM events that can mimic these features of interest (background) which
 1855 implies that it is not possible to say with certainty that a given event is signal or
 1856 background. In that sense, the problem can be formulated as one where a set of
 1857 events have to be classified according to some features; these features correspond to
 1858 the measurements of several parameters like energy or momentum, organized in a
 1859 set of *input variables*. The measurements for each event can be written in a vector
 1860 $\mathbf{x} = (x_1, \dots, x_n)$ for which

- 1861 • Signal hypotheses $\rightarrow f(\mathbf{x}|s)$ is the probability density (*likelihood function*) that
 1862 \mathbf{x} is the set of measured values given that the events is a signal event.
- 1863 • Background hypotheses $\rightarrow f(\mathbf{x}|b)$ is the probability density (*likelihood function*)
 1864 that \mathbf{x} is the set of measured values given that the event is a background event.

1865 Figure 5.1 shows three ways to perform a classification of events for which mea-
 1866 surements of two properties, two input variables, have been performed; blue circles
 1867 represent signal events while red triangles represent background events. The classi-
 1868 fication on (a) is *cut-based* requiring $x_1 < c_1$ and $x_2 < c_2$; usually the cut values are
 1869 chosen according to some knowledge about the event process. In (b), the classification
 1870 is performed by stating a cut involving a linear function of the input variables and
 1871 so the boundary, while in (c) the the relationship between the input variables is not
 1872 linear thus the boundary is not linear either.

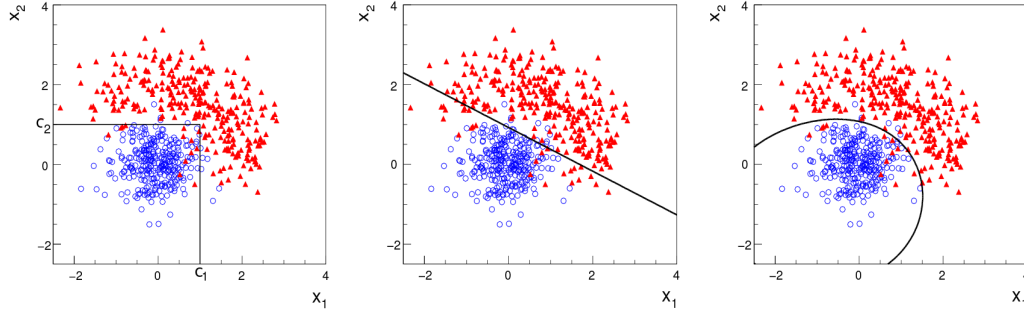


Figure 5.1: Scatter plots-MVA event classification. Distribution of two input variables x_1 and x_2 measured for a set of events; blue circles represent signal events and red triangles represent background events. The classification is based on (a) cuts, (b) linear boundary, and (c) nonlinear boundary [108]

1873 The boundary can be parametrized in terms of the input variables such that the
 1874 cut is set on the parametrization instead of on the variables, i.e., $y(\mathbf{x}) = y_{cut}$ with
 1875 y_{cut} a constant; thus, the acceptance or rejection of an event is based on what side
 1876 of the boundary is the event located. If $y(\mathbf{x})$ has functional form, it can be used to
 1877 determine the probability distribution functions $p(y|s)$ and $p(y|b)$ and then perform
 1878 a scalar test statistic with a single cut on the scalar variable y .

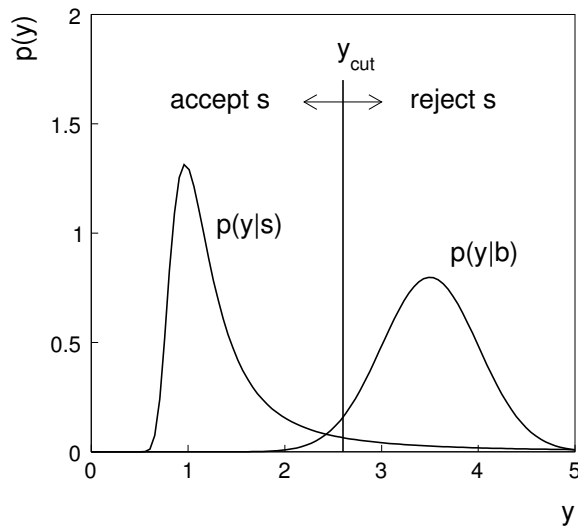


Figure 5.2: Distributions of the scalar test statistic $y(\mathbf{x})$ under the signal and background hypotheses. [108]

1879 Figure 5.2 illustrates what would be the probability distribution functions under
 1880 the signal and background hypotheses for a scalar test statistic with a cut on the
 1881 classifier y . Notice that the tails of the distributions indicate that some signal events
 1882 fall on the rejection region and some background events fall on the acceptance region;
 1883 therefore, it is convenient to define the *efficiency* with which events of a given type
 1884 are accepted, thus, the signal and background efficiencies are given by

$$\varepsilon_s = P(\text{accept event}|s) = \int_A f(\mathbf{x}|s) d\mathbf{x} = \int_{-\infty}^{y_{\text{cut}}} p(y|s) dy , \quad (5.1)$$

$$\varepsilon_b = P(\text{accept event}|b) = \int_A f(\mathbf{x}|b) d\mathbf{x} = \int_{-\infty}^{y_{\text{cut}}} p(y|b) dy , \quad (5.2)$$

1885 where A is the acceptance region. Under these conditions, the background hypothesis
 1886 corresponds to the *null hypothesis* (H_0), the signal hypothesis corresponds to the
 1887 *alternative hypothesis* (H_1), the background efficiency is the significance level of the
 1888 test, and signal efficiency is the power of the test; what is sought in an analysis is to
 1889 maximize the power of the test relative to the significance level.

1890 5.1.1 Decision trees

1891 For this thesis, the implementation of the MVA strategy, described above, is per-
 1892 formed through decision trees by using the TMVA software package [109] included in
 1893 the the ROOT analysis framework [110]. In a simple picture, a decision tree classifies
 1894 events according to their input variables values by setting a cut on each input variable
 1895 and checking which events are on which side of the cut, just as proposed in the MVA
 1896 strategy, but in addition, as a machine learning algorithm, decision trees offer the
 1897 possibility to be trained and then perform the classification efficiently.

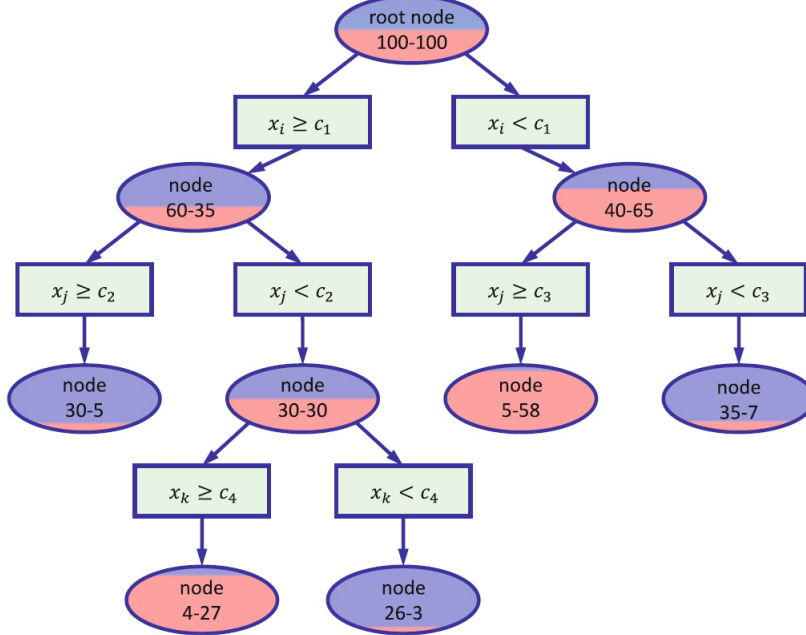


Figure 5.3: Example of a decision tree. Each node is fed with a MC sample mixing signal and background events (left-right numbers); nodes colors represent the relative amount of signal/background events [111].

1898 The training or growing of a decision tree is the process that defines the rules for
 1899 classifying events; this process is represented in figure5.3 and consist of several steps

1900 • take MC samples of signal and background events and split them into two parts
 1901 each; first parts form the training sample which will be used in the decision tree
 1902 training, while the second parts form the test sample which will be used for
 1903 testing the final classifier obtained from the training. Each event has associated
 1904 a set of input variables $\mathbf{x} = (x_1, \dots, x_n)$ which serve to distinguish between signal
 1905 and background events. The training sample is taken in at the root *node*.

1906 • pick one variable, say x_i
 1907 • pick one value of x_i , each event has its own value of x_i , and split the training
 1908 sample into two subsamples B_1 and B_2 ; B_1 contains events for which $x_i < c_1$

- 1909 while B_2 contains the rest of the training events;
- 1910 • scan all possible values of x_i and find the splitting value that provides the *best*
 1911 classification¹, i.e., B_1 is mostly made of signal events while B_2 is mostly made
 1912 of background events.
- 1913 • It is possible that variables other than the picked one produce a better classi-
 1914 fication, hence, all the variables have to be evaluated. Pick the next variable,
 1915 say x_j , and repeat the scan over its possible values.
- 1916 • At the end, all the variables and their values will have been scanned, the *best*
 1917 variable and splitting value will have been identified, say x_1, c_1 , and there will
 1918 be two nodes fed with the subsamples B_1 and B_2 .
- 1919 Nodes are further split by repeating the decision process until: a given number of
 1920 final nodes is obtained, nodes are largely dominated by either signal or background
 1921 events, or nodes has too few events to continue. Final nodes are called *leaves* and they
 1922 are classified as signal or background leaves according to the class of the majority of
 1923 events in them. Each *branch* in the tree corresponds to a sequence of cuts.
- 1924 The quality of the classification at each node is evaluated through a separation
 1925 criteria; there are several of them but the *Gini Index* (G) is the one used in the
 1926 decision trees trained for the analysis in this thesis. G is written in terms of the
 1927 purity (P), i.e. the fraction of signal events, of the samples after the separation is
 1928 made; it is given by

$$G = P(1 - P) \quad (5.3)$$

¹ Quality of the classification will be treated in the next paragraph.

1929 notice that $P=0.5$ at the root node while $G=0$ for pure leaves. For a node A split
 1930 into two nodes B_1 and B_2 the G gain is

$$\Delta G = G(A) - G(B_1) - G(B_2) \quad (5.4)$$

1931 the *best* classification corresponds to that for which the gain of G is maximized; hence,
 1932 the scanning over all event's variables and their values is of capital importance.

1933 In order to provide a numerical output for the classification, events in a sig-
 1934 nal(background) leaf are assigned an score of 1(-1) each, defining in this way the
 1935 decision tree *classifier or weak learner* as

$$f(\mathbf{x}) = \begin{cases} 1 & \mathbf{x} \text{ in signal region,} \\ -1 & \mathbf{x} \text{ in background region.} \end{cases}$$

1936 Figure 5.4 shows an example of the classification of a sample of events, containing
 1937 two variables, performed by a decision tree.

1938 5.1.2 Boosted decision trees (BDT).

1939 Event misclassification occurs when a training event ends up in the wrong leaf, i.e., a
 1940 signal event ends up in a background leaf or a background event ends up in a signal
 1941 leaf. A way to correct it is to assign a weight to the misclassified events and train
 1942 a second tree using the reweighted events; the event reweighting is performed by a
 1943 boosting algorithm, events with increased weight are known as *boosted* events, in such
 1944 a way that when used in the training of a new decision tree they get correctly classified.
 1945 The process is repeated iteratively adding a new tree to a forest and creating a set
 1946 of classifiers which are combined to create the next classifier; the final classifier offers

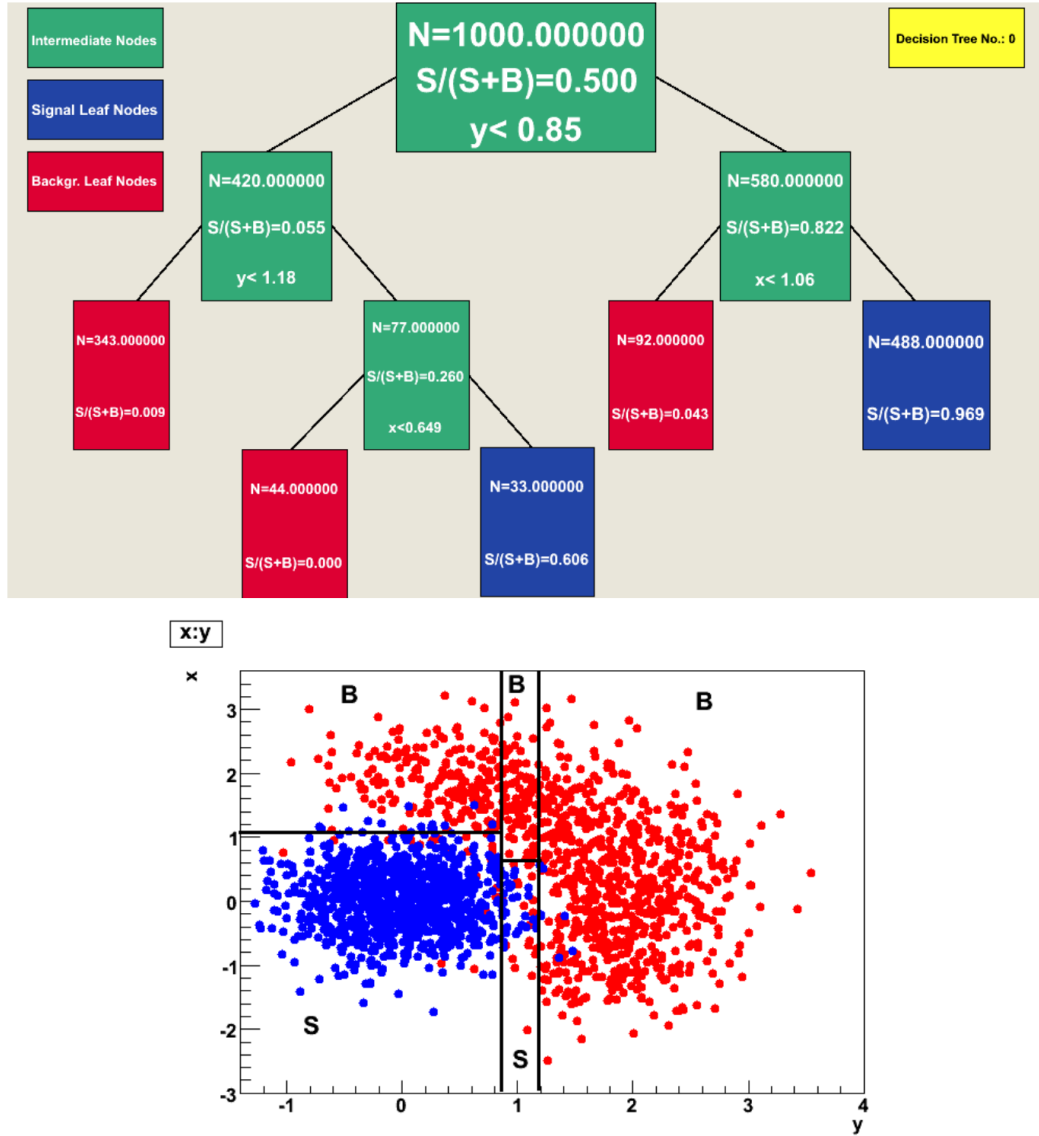


Figure 5.4: Example of a decision tree output. Each leaf, blue for signal events and red for background events, represent a region in the variables phase space [112].

1947 more stability² and has a smaller misclassification rate than any individual ones. The
 1948 resulting tree collection is known as a *boosted decision tree (BDT)*.
 1949 Thus, purity of the sample is generalized to

² Decision trees suffer from sensitivity to statistical fluctuations in the training sample which may leads to very different results with an small change in the training samples.

$$P = \frac{\sum_s w_s}{\sum_s w_s + \sum_b w_b} \quad (5.5)$$

1950 where w_s and w_b are the weights of the events; the Gini index is also generalized

$$G = \left(\sum_i^n w_i \right) P(1 - P) \quad (5.6)$$

1951 with n the number of events in the node. The final score of an event, after pass-
 1952 ing through the forest, is calculated as the renormalized sum of all the individual
 1953 (possibly weighted) scores; thus, high(low) score implies that the event is most likely
 1954 signal(background).

1955 The boosting procedure, implemented in the *Gradient boosting* algorithm used
 1956 in this thesis, produce a classifier $F(\mathbf{x})$ which is the weighted sum of the individual
 1957 classifiers obtained after each iteration,i.e.,

$$F(\mathbf{x}) = \sum_{m=1}^M \beta_m f(\mathbf{x}; a_m) \quad (5.7)$$

1958 where M is the number of trees in the forest. The *loss function* $L(F, y)$ represent the
 1959 deviation between the classifier $F(\mathbf{x})$ response and the true value y obtained from the
 1960 training sample (1 for signal events and -1 for background event), according to

$$L(F, y) = \ln(1 + e^{-2F(\mathbf{x})y}) \quad (5.8)$$

1961 thus, the reweighting is employed to ensure the minimization of the loss function;
 1962 a more detailed description of the minimization procedure can be found in reference
 1963 [113]. The final classifier output is later used as a final discrimination variable, labeled
 1964 as *BDT output/response*.

1965 **5.1.3 Overtraining.**

1966 Decision trees offer the possibility to have as many nodes as wished in order to
 1967 reduce the misclassification to zero (in theory); however, when a classifier is too much
 1968 adjusted to a particular training sample, the classifier response to a slightly different
 1969 sample may leads to a completely different classification results; this effect is know
 1970 as *overtraining*.

1971 An alternative to reduce the overtraining in BDTs consist in pruning the tree by
 1972 removing statistically insignificant nodes after the tree growing is completed but this
 1973 option is not available for BDTs with gradient boosting in the TMVA-toolkit, there-
 1974 fore, the overtraining has to be reduced by tuning the algorithm, number of nodes,
 1975 minimum number of events in the leaves, etc. The overtraining can be evaluated
 1976 by comparing the responses of the classifier when running over the training and test
 1977 samples.

1978 **5.1.4 Variable ranking.**

1979 BDTs have the couple of particular advantages related to the input variables; on one
 1980 side, they are relatively insensitive to the number of input variables used in the vector
 1981 \mathbf{x} . The ranking of the BDT input variables is determined by counting the number of
 1982 times a variable is used to split decision tree nodes; in addition, the separation gain-
 1983 squared achieved in the splitting and the number of events in the node are accounted
 1984 by applying a weighting to that number. Thus, those variables with small or no power
 1985 to separate signal and background events are rarely chosen to split the nodes,i.e., are
 1986 effectively ignored.

1987 On the other side, variables correlations play an important role for some MVA
 1988 methods like the Fisher discriminant algorithm in which the first step consist of

1989 performing a linear transformation to a phase space where the correlations between
 1990 variables are removed; in case of BDT algorithm, correlations do not affect the per-
 1991 formance.

1992 **5.1.5 BDT output example.**

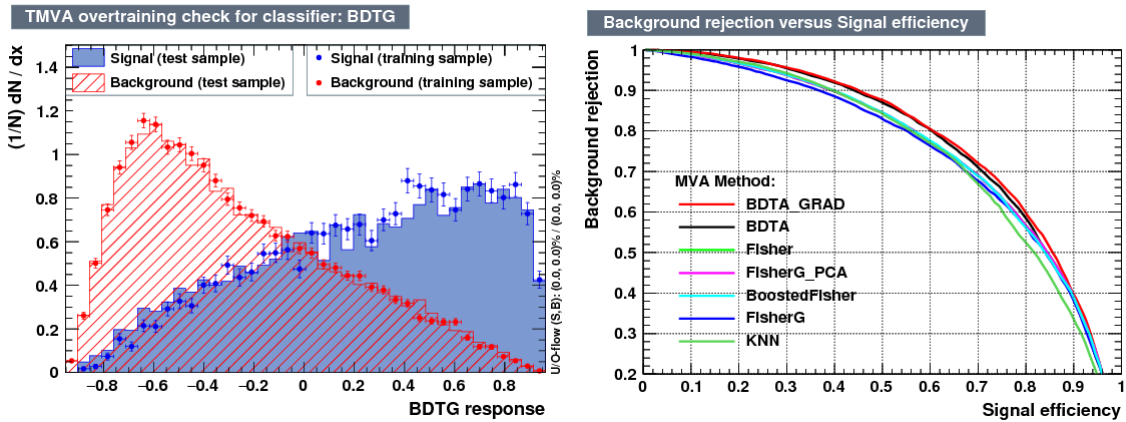


Figure 5.5: Left: Output distributions for the gradient boosted decision tree (BDTG) classifier using a sample of signal($pp \rightarrow tHq$) and background($pp \rightarrow t\bar{t}$) events. Right: Background rejection vs signal efficiency (ROC curves) for various MVA classifiers running over the same sample used to produce the plot on the left.

1993 Left side of figure 5.5 shows the BDT output distributions for signal($pp \rightarrow tHq$)
 1994 and background($pp \rightarrow t\bar{t}$) events; this plot is the equivalent to the one showed in
 1995 figure 5.2. A forest with 800 trees, maximum depth per tree = 3, and gradient
 1996 boosting have been used as training parameters. The BDTG classifier offers a good
 1997 separation power; while there is a small overtraining in the signal distribution, the
 1998 background distribution seems to be well predicted which might indicate that the
 1999 sample is composed of more background than signal events.

2000 Right side of figure 5.5 shows the background rejection vs signal efficiency curves
 2001 for several combinations of MVA classifiers-boosting algorithms; these curves are
 2002 known as ROC curves and give an indication of the performance of the classifier. The

2003 best performance is achieved with the BDTG classifier (BDTA_GRAD).

2004 5.2 Statistical inference.

2005 Once events are classified, the next step consists in finding the parameters that define
 2006 the likelihood functions $f(\mathbf{x}|s), f(\mathbf{x}|b)$ for signal and background events respectively.
 2007 In general, likelihood functions depend not only on the measurements but also on
 2008 parameters (θ_m) that define their shapes; the process of estimating these *unknown*
 2009 *parameters* and their uncertainties from the experimental data is called *inference*.
 2010 The likelihood function for N the events the in a sample is the combination of all the
 2011 likelihoods functions

$$L(\boldsymbol{\theta}) = \prod_{i=1}^N f(\mathbf{x}^i | \boldsymbol{\theta}) = \prod_{i=1}^N f(x_1^i, \dots, x_n^i; \theta_1, \dots, \theta_m) \quad (5.9)$$

2012 Thus, the estimation of the unknown parameters from experimental data samples
 2013 is written in terms of a central value using the notation

$$\theta = \hat{\theta} \pm \delta\theta \quad (5.10)$$

2014 where the interval $[\hat{\theta} + \delta\theta, \hat{\theta} - \delta\theta]$ is called *confidence interval*; it is usually inter-
 2015 preted, in the limit of infinite number of experiments, as the interval where the true
 2016 value of the unknown parameter θ is contained with a probability of 0.6827 (if no
 2017 other convention is stated).

2018 5.2.1 Nuisance parameters.

2019 The unknown parameter vector $\boldsymbol{\theta}$ is made of two types of parameters: on one side,
 2020 those parameters that provide information about the physical observables of interest

2021 for the experiment (*parameters of interest*); on the other side, the *nuisance parameters*
 2022 that are not of direct interest for the experiment but that needs to be included in
 2023 the analysis in order to achieve a satisfactory description of the data. They represent
 2024 effects of the detector response like the finite resolutions of the detection systems,
 2025 miscalibrations, and in general any source of uncertainty introduced in the analysis.

2026 In some cases the nuisance parameters are estimated using dedicated data samples,
 2027 for instance data from test beams for calibration purposes, when MC samples are
 2028 not suitable. The nuisance parameter uncertainties produce *systematic uncertainties*
 2029 while the uncertainties associated to fluctuations in data and related to the estimation
 2030 of the parameters of interest produce *statistical uncertainties*.

2031 5.2.2 Maximum likelihood estimation method

2032 The function that produce the estimate of a parameter is called *estimator*, there-
 2033 fore, estimators are usually constructed using mathematical procedures encoded in
 2034 algorithms. The estimation method used in this thesis is the *Maximum Likelihood*
 2035 *Estimation* method (MLE); it is based on the combined likelihood function defined
 2036 by eqn. 5.9 and the procedure seeks for the parameter set that corresponds to the
 2037 maximum value of the combined likelihood function, i.e., the *maximum likelihood*
 2038 *estimator* of the unknown parameter vector $\boldsymbol{\theta}$ is the function that produce the vec-
 2039 tor $\hat{\boldsymbol{\theta}}$ for which the likelihood function $L(\boldsymbol{\theta})$ evaluated at the measured sample \mathbf{x} is
 2040 maximum.

2041 Usually, the logarithm of the likelihood function is used in the numerical algo-
 2042 rithms implementations in order to avoid underflow the numerical precision of the
 2043 computers due to the product of low likelihoods. In addition, it is usual minimize the
 2044 negative logarithm of the likelihood function instead of maximizing the logarithm of

2045 it because in this way the procedure consist of differentiate a sum of therms and set
 2046 the sum to zero; therefore

$$F(\boldsymbol{\theta}) = -\ln L(\boldsymbol{\theta}) = -\sum_{i=1}^N f(\mathbf{x}^i | \boldsymbol{\theta}). \quad (5.11)$$

2047 The minimization process is performed by the software MINUIT [114] imple-
 2048 mented in the ROOT analysis framework. In case of large data samples the compu-
 2049 tational resources needed to calculate the likelihood function are too big; therefore,
 2050 the parameter estimation is performed using binned distributions of the variables of
 2051 interest for which the *binned likelihood function* is given by

$$L(data|\mu, \theta) = \prod_{i=1} \frac{(\mu s_i(\theta) + b_i(\theta))^{n_i}}{n_i!} e^{-\mu s_i(\theta) - b_i(\theta)}, \quad (5.12)$$

2052 with s_i and b_i the expected number of signal and background yields for bin i
 2053 respectively³, n_i is the observed number of events in the bin i and $\mu = \sigma/\sigma_{SM}$ is
 2054 the signal strength. Notice that the number of entries per bin follows a Poisson
 2055 distribution. The analysis presented in this thesis is based on the binned distribution
 2056 of the ratio signal/background obtained from the classification BDT outputs.

2057 ; it is achieved, according to the Neyman-Pearson lemma [115],
 2058 by defining the acceptance region such that, for \mathbf{x} inside the region, the likelihood
 2059 ratio, i.e., the ratio of probability distribution functions for signal and background,

2060 5.3 exclusion limits

2061 5.4 asymptotic limits

³ expected number of entries in each bin is determined from the theoretical distribution.

²⁰⁶² **Chapter 6**

²⁰⁶³ **Search for production of a Higgs**

²⁰⁶⁴ **boson and a single top quark in**

²⁰⁶⁵ **multilepton final states in pp**

²⁰⁶⁶ **collisions at $\sqrt{s} = 13$ TeV**

²⁰⁶⁷ **6.1 Introduction**

²⁰⁶⁸ Dont forget to mention previous constrains to ct check reference ?? and references

²⁰⁶⁹ <https://link.springer.com/content/pdf/10.1007%2FJHEP01>

²⁰⁷⁰ A. Azatov, R. Contino and J. Galloway, \rightarrow Model-Independent Bounds on a

²⁰⁷¹ Light Higgs, \rightarrow JHEP 1204 (2012) 127 [arXiv:1202.3415 [hep-ph]].

²⁰⁷² J. R. Espinosa, C. Grojean, M. Muhlleitner and M. Trott, \rightarrow Fingerprinting

²⁰⁷³ Higgs Suspects at the LHC, \rightarrow JHEP 1205 (2012) 097 [arXiv:1202.3697 [hep-ph]].

²⁰⁷⁴ This chapter present the search for the associated production of a Higgs boson and

²⁰⁷⁵ a single top quark events with three leptons in the final state, targeting Higgs decay

2076 modes to WW , ZZ , and $\tau\tau$. The analysis uses the 13 TeV dataset produced in 2016,
 2077 corresponding to an integrated luminosity of 35.9fb^{-1} . It is based on and expands
 2078 previous analyses at 8 TeV [?, ?] and searches for associated production of $t\bar{t}$ and
 2079 Higgs in the same channel [?], and complements searches in other decay channels
 2080 targeting $H \rightarrow b\bar{b}$ [?].

2081 As showed in section 2.4, the cross section of the associated production of a Higgs
 2082 boson and a single top quark (tHq) process is driven by a destructive interference of
 2083 two contributions (see Figure 6.1), where the Higgs couples to either the W boson or
 2084 the top quark. Any deviation from the standard model (SM) in the Higgs coupling
 2085 structure could therefore lead to a large enhancement of the cross section, making
 2086 this analysis sensitive to such deviations. A second process, where the Higgs and
 2087 top quark are accompanied by a W boson (tHW) has similar behavior, albeit with a
 2088 weaker interference pattern.

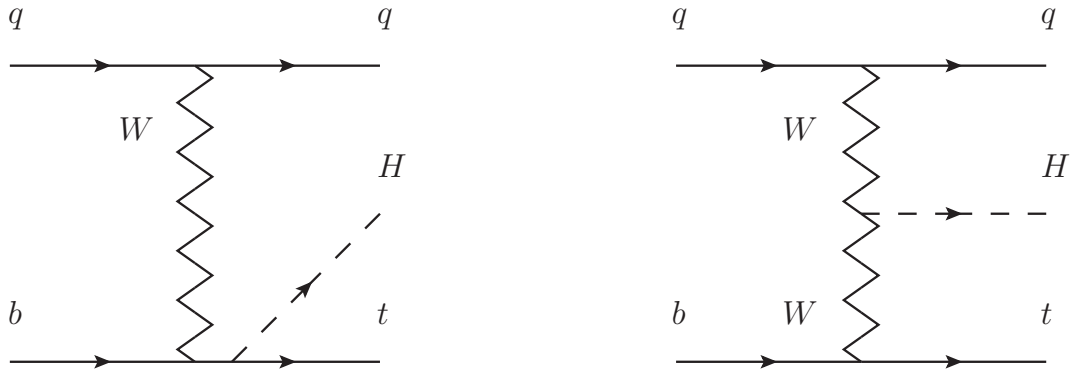


Figure 6.1: The two leading-order diagrams of tHq production.

2089 We selects events with three leptons and a b tagged jet in the final state. The tHq
 2090 signal contribution is then determined in a fit of the observed data to two multivariate
 2091 classifier outputs, each trained to discriminate against one of the two dominant back-
 2092 grounds of events with non-prompt leptons from $t\bar{t}$ and of associated production of $t\bar{t}$

2093 and vector bosons ($t\bar{t}W$, $t\bar{t}Z$). The fit result is then used to set an upper limit on the
 2094 combined $t\bar{t}H$, tHq and tHW production cross section, as a function of the relative
 2095 coupling strengths of Higgs and top quark and Higgs and W boson, respectively.

2096 6.2 Data and MC Samples

2097 The data considered in this analysis were collected by the CMS experiment dur-
 2098 ing 2016 and correspond to a total integrated luminosity of 35.9fb^{-1} . Only periods
 2099 when the CMS magnet was on were considered when selecting the data samples, that
 2100 corresponds to the 23 Sep 2016 (Run B to G) and PromptReco (Run H) versions
 2101 of the datasets. The MC samples used in this analysis correspond to the RunI-
 2102 ISummer16MiniAODv2 campaign produced with CMSSW 80X. The two signal sam-
 2103 ples (for tHq and tHW) were produced with MG5_aMC@NLO (version 5.222), in
 2104 leading-order mode, and are normalized to next-to-leading-order cross sections,
 2105 see Tab. 6.1. Each sample is generated with a set of event weights corresponding to
 2106 different values of κ_t and κ_V couplings as shown in Tab. 6.2.

2107 6.2.1 Full 2016 dataset and MC samples

Sample	σ [pb]	BF
/THQ_Hincl_13TeV-madgraph-pythia8_TuneCUETP8M1/	0.7927	0.324
/THW_Hincl_13TeV-madgraph-pythia8_TuneCUETP8M1/	0.1472	1.0

Table 6.1: Signal samples and their cross section and branching fraction used in this analysis. See Ref. [?] for more details.

2108 Different MC generators were used to generate the background processes. The
 2109 dominant sources ($t\bar{t}$, $t\bar{t}W$, $t\bar{t}Z$, $t\bar{t}H$) were produced using AMC@NLO interfaced
 2110 to PYTHIA8, and are scaled to NLO cross sections. Other processes are simulated

		<i>tHq</i>		<i>tHW</i>		
κ_V	κ_t	sum of weights	cross section [pb]	sum of weights	cross section [pb]	LHE weights
1.0	-3.0	35.700022	2.991	11.030445	0.6409	LHEweight_wgt[446]
1.0	-2.0	20.124298	1.706	5.967205	0.3458	LHEweight_wgt[447]
1.0	-1.5	14.043198	1.205	4.029093	0.2353	LHEweight_wgt[448]
1.0	-1.25	11.429338	0.9869	3.208415	0.1876	LHEweight_wgt[449]
1.0	-1.0		0.7927		0.1472	
1.0	-0.75	7.054998	0.6212	1.863811	0.1102	LHEweight_wgt[450]
1.0	-0.5	5.294518	0.4723	1.339886	0.07979	LHEweight_wgt[451]
1.0	-0.25	3.818499	0.3505	0.914880	0.05518	LHEweight_wgt[452]
1.0	0.0	2.627360	0.2482	0.588902	0.03881	LHEweight_wgt[453]
1.0	0.25	1.719841	0.1694	0.361621	0.02226	LHEweight_wgt[454]
1.0	0.5	1.097202	0.1133	0.233368	0.01444	LHEweight_wgt[455]
1.0	0.75	0.759024	0.08059	0.204034	0.01222	LHEweight_wgt[456]
1.0	1.0	0.705305	0.07096	0.273617	0.01561	LHEweight_wgt[457]
1.0	1.25	0.936047	0.0839	0.442119	0.02481	LHEweight_wgt[458]
1.0	1.5	1.451249	0.1199	0.709538	0.03935	LHEweight_wgt[459]
1.0	2.0	3.335034	0.2602	1.541132	0.08605	LHEweight_wgt[460]
1.0	3.0	10.516125	0.8210	4.391335	0.2465	LHEweight_wgt[461]
1.5	-3.0	45.281492	3.845	13.426212	0.7825	LHEweight_wgt[462]
1.5	-2.0	27.606715	2.371	7.809713	0.4574	LHEweight_wgt[463]
1.5	-1.5	20.476088	1.784	5.594971	0.3290	LHEweight_wgt[464]
1.5	-1.25	17.337465	1.518	4.635978	0.2749	LHEweight_wgt[465]
1.5	-1.0	14.483302	1.287	3.775902	0.2244	LHEweight_wgt[466]
1.5	-0.75	11.913599	1.067	3.014744	0.1799	LHEweight_wgt[467]
1.5	-0.5	9.628357	0.874	2.352505	0.1410	LHEweight_wgt[468]
1.5	-0.25	7.627574	0.702	1.789184	0.1081	LHEweight_wgt[469]
1.5	0.0	5.911882	0.5577	1.324946	0.08056	LHEweight_wgt[470]
1.5	0.25	4.479390	0.4365	0.959295	0.05893	LHEweight_wgt[471]
1.5	0.5	3.331988	0.3343	0.692727	0.04277	LHEweight_wgt[472]
1.5	0.75	2.469046	0.2558	0.525078	0.03263	LHEweight_wgt[473]
1.5	1.0	1.890565	0.2003	0.456347	0.02768	LHEweight_wgt[474]
1.5	1.25	1.596544	0.1689	0.486534	0.02864	LHEweight_wgt[475]
1.5	1.5	1.586983	0.1594	0.615638	0.03509	LHEweight_wgt[476]
1.5	2.0	2.421241	0.2105	1.170602	0.06515	LHEweight_wgt[477]
1.5	3.0	7.503280	0.5889	3.467546	0.1930	LHEweight_wgt[478]
0.5	-3.0	27.432685	2.260	8.929074	0.5136	LHEweight_wgt[479]
0.5	-2.0	13.956013	1.160	4.419093	0.2547	LHEweight_wgt[480]
0.5	-1.5	8.924438	0.7478	2.757611	0.1591	LHEweight_wgt[481]
0.5	-1.25	6.835341	0.5726	2.075247	0.1204	LHEweight_wgt[482]
0.5	-1.0	5.030704	0.4273	1.491801	0.08696	LHEweight_wgt[483]
0.5	-0.75	3.510528	0.2999	1.007273	0.05885	LHEweight_wgt[484]
0.5	-0.5	2.274811	0.1982	0.621663	0.03658	LHEweight_wgt[485]
0.5	-0.25	1.323555	0.1189	0.334972	0.01996	LHEweight_wgt[486]
0.5	0.0	0.656969	0.06223	0.147253	0.008986	LHEweight_wgt[487]
0.5	0.25	0.274423	0.02830	0.058342	0.003608	LHEweight_wgt[488]
0.5	0.5	0.176548	0.01778	0.068404	0.003902	LHEweight_wgt[489]
0.5	0.75	0.363132	0.03008	0.177385	0.009854	LHEweight_wgt[490]
0.5	1.0	0.834177	0.06550	0.385283	0.02145	LHEweight_wgt[491]
0.5	1.25	1.589682	0.1241	0.692099	0.03848	LHEweight_wgt[492]
0.5	1.5	2.629647	0.2047	1.097834	0.06136	LHEweight_wgt[493]
0.5	2.0	5.562958	0.4358	2.206057	0.1246	LHEweight_wgt[494]
0.5	3.0	14.843102	1.177	5.609519	0.3172	LHEweight_wgt[495]

Table 6.2: κ_V and κ_t combinations generated for the two signal samples and their NLO cross sections. The *tHq* cross section is multiplied by the branching fraction of the enforced leptonic decay of the top quark (0.324). See also Ref. [?].

Sample	σ [pb]
TTWJetsToLNu_TuneCUETP8M1_13TeV-amcatnloFXFX-madspin-pythia8	0.2043
TTZToLLNuNu_M-10_TuneCUETP8M1_13TeV-amcatnlo-pythia8	0.2529
tthJetToNonbb_M125_13TeV_amcatnloFXFX_madspin_pythia8_mWCutfix /store/cmst3/group/susy/gpetrucc/13TeV/u/TTLL_m1to10_L0_NoMS_for76X/	0.2151 0.0283
WGToLNuG_TuneCUETP8M1_13TeV-madgraphMLM-pythia8	585.8
ZGTo2LG_TuneCUETP8M1_13TeV-amcatnloFXFX-pythia8	131.3
TGJets_TuneCUETP8M1_13TeV_amcatnlo_madspin_pythia8	2.967
TGJets_TuneCUETP8M1_13TeV_amcatnlo_madspin_pythia8	2.967
TTGJets_TuneCUETP8M1_13TeV-amcatnloFXFX-madspin-pythia8	3.697
WpWpJJ_EWK_QCD_TuneCUETP8M1_13TeV-madgraph-pythia8	0.03711
ZZZ_TuneCUETP8M1_13TeV-amcatnlo-pythia8	0.01398
WWZ_TuneCUETP8M1_13TeV-amcatnlo-pythia8	0.1651
WZZ_TuneCUETP8M1_13TeV-amcatnlo-pythia8	0.05565
WW_DoubleScattering_13TeV-pythia8	1.64
tZq_ll_4f_13TeV-amcatnlo-pythia8_TuneCUETP8M1	0.0758
ST_tWll_5f_LO_13TeV-MadGraph-pythia8	0.01123
TTTT_TuneCUETP8M1_13TeV-amcatnlo-pythia8	0.009103
WZTo3LNu_TuneCUETP8M1_13TeV-powheg-pythia8	4.4296
ZZTo4L_13TeV_powheg_pythia8	1.256
TTJets_SingleLeptFromTbar_TuneCUETP8M1_13TeV-madgraphMLM-pythia8	182.1754
TTJets_SingleLeptFromT_TuneCUETP8M1_13TeV-madgraphMLM-pythia8	182.1754
TTJets_DiLept_TuneCUETP8M1_13TeV-madgraphMLM-pythia8	87.3
DYJetsToLL_M-10to50_TuneCUETP8M1_13TeV-amcatnloFXFX-pythia8	18610
DYJetsToLL_M-50_TuneCUETP8M1_13TeV-madgraphMLM-pythia8	6024
WJetsToLNu_TuneCUETP8M1_13TeV-amcatnloFXFX-pythia8	61526.7
ST_tW_top_5f_inclusiveDecays_13TeV-powheg-pythia8_TuneCUETP8M1	35.6
ST_tW_antitop_5f_inclusiveDecays_13TeV-powheg-pythia8_TuneCUETP8M1	35.6
ST_t-channel_4f_leptonDecays_13TeV-amcatnlo-pythia8_TuneCUETP8M1	70.3144
ST_t-channel_antitop_4f_leptonDecays_13TeV-powheg-pythia8_TuneCUETP8M1	26.2278
ST_s-channel_4f_leptonDecays_13TeV-amcatnlo-pythia8_TuneCUETP8M1	3.68064
WWTo2L2Nu_13TeV-powheg	10.481

Table 6.3: List of background samples used in this analysis (CMSSW 80X). In the first section of the table are listed the samples of the processes for which we use the simulation to extract the final yields and shapes, in the second section the samples of the processes we will estimate from data. The MC simulation is used to design the data driven methods and derive the associated systematics.

Sample	σ [pb]
ttWJets_13TeV_madgraphMLM	0.6105
ttZJets_13TeV_madgraphMLM	0.5297/0.692

Table 6.4: Leading-order $t\bar{t}W$ and $t\bar{t}Z$ samples used in the signal BDT training.

2111 using POWHEG interfaced to PYTHIA, or bare PYTHIA (see table 6.3 and [?] for
2112 more details).

Three lepton and Four lepton
HLT_DiMu9_Ele9_CaloIdL_TrackIdL_v*
HLT_Mu8_DiEle12_CaloIdL_TrackIdL_v*
HLT_TripleMu_12_10_5_v*
HLT_Ele16_Ele12_Ele8_CaloIdL_TrackIdL_v*
HLT_Mu23_TrkIsoVVL_Ele8_CaloIdL_TrackIdL_IsoVL_v*
HLT_Mu23_TrkIsoVVL_Ele8_CaloIdL_TrackIdL_IsoVL_DZ_v*
HLT_Mu8_TrkIsoVVL_Ele23_CaloIdL_TrackIdL_IsoVL_v*
HLT_Mu8_TrkIsoVVL_Ele23_CaloIdL_TrackIdL_IsoVL_DZ_v*
HLT_Ele23_Ele12_CaloIdL_TrackIdL_IsoVL_DZ_v*
HLT_Mu17_TrkIsoVVL_Mu8_TrkIsoVVL_DZ_v*
HLT_Mu17_TrkIsoVVL_TkMu8_TrkIsoVVL_DZ_v*
HLT_IsoMu22_v*
HLT_IsoTkMu22_v*
HLT_IsoMu22_eta2p1_v*
HLT_IsoTkMu22_eta2p1_v*
HLT_IsoMu24_v*
HLT_IsoTkMu24_v*
HLT_Ele27_WPTight_Gsf_v*
HLT_Ele25_eta2p1_WPTight_Gsf_v*
HLT_Ele27_eta2p1_WPLoose_Gsf_v*

Table 6.5: Table of high-level triggers that we consider in the analysis.

2113 6.2.2 Triggers

2114 We consider online-reconstructed events triggered by one, two, or three leptons.
 2115 Single-lepton triggers are included to boost the acceptance of events where the p_T of
 2116 the sub-leading lepton falls below the threshold of the double-lepton triggers. Ad-
 2117 ditionally, by including double-lepton triggers in the ≥ 3 lepton category, as well
 2118 as single-lepton triggers in all categories, we increase the efficiency, considering the
 2119 logical “or” of the trigger decisions of all the individual triggers in a given category.
 2120 Tab. 6.5 shows the lowest-threshold non-prescaled triggers present in the High-Level
 2121 Trigger (HLT) menus for both Monte-Carlo and data in 2016.

2122 6.2.2.1 Trigger efficiency scale factors

2123 The efficiency of events to pass the trigger is measured in simulation (trivially using
 2124 generator information) and in the data (using event collected by an uncorrelated

Category	Scale Factor
ee	1.01 ± 0.02
e μ	1.01 ± 0.01
$\mu\mu$	1.00 ± 0.01
3l	1.00 ± 0.03

Table 6.6: Trigger efficiency scale factors and associated uncertainties, shown here rounded to the nearest percent.

2125 MET trigger). Small differences between the data and MC efficiencies are corrected
 2126 by applying scale factors as shown in Tab. 6.6. The exact procedure and control plots
 2127 are documented in [?] for the current analysis.

2128 6.3 Object Identification and event selection

2129 6.3.1 Jets and b tagging

2130 The analysis uses anti- k_t (0.4) particle-flow (PF) jets, corrected for charged hadrons
 2131 not coming from the primary vertex (charged hadron subtraction), and having jet
 2132 energy corrections (`Summer16_23Sep2016V3`) applied as a function of the jet E_T and
 2133 η . Jets are only considered if they have a transverse energy above 25GeV.

2134 In addition, they are required to be separated from any lepton candidates passing
 2135 the fakeable object selections (see Tables 6.7 and 6.8) by $\Delta R > 0.4$.

2136 The loose and medium working points of the CSV b-tagging algorithm are used to
 2137 identify b jets. Data/simulation differences in the b tagging performance are corrected
 2138 by applying per-jet weights to the simulation, dependent on the jet p_T , eta, b tagging
 2139 discriminator, and flavor (from simulation truth) [?]. The per-event weight is taken
 2140 as the product of the per-jet weights, including those of the jets associated to the
 2141 leptons. More details can be found in the corresponding $t\bar{t}H$ documentation [?, ?].

2142 **6.3.2 Lepton selection**

Cut	Loose	Fakeable object	Tight
$ \eta < 2.4$	✓	✓	✓
p_T	$> 5\text{GeV}$	$> 15\text{GeV}$	$> 15\text{GeV}$
$ d_{xy} < 0.05 \text{ (cm)}$	✓	✓	✓
$ d_z < 0.1 \text{ (cm)}$	✓	✓	✓
$\text{SIP}_{3D} < 8$	✓	✓	✓
$I_{\text{mini}} < 0.4$	✓	✓	✓
is Loose Muon	✓	✓	✓
jet CSV	—	< 0.8484	< 0.8484
is Medium Muon	—	—	✓
tight-charge	—	—	✓
lepMVA > 0.90	—	—	✓

Table 6.7: Requirements on each of the three muon selections. In the cases where the cut values change between the selections, those values are listed in the table. Otherwise, whether the cut is applied is indicated. For the two p_T^{ratio} and CSV rows, the cuts marked with a † are applied to leptons that fail the lepton MVA cut, while the loose cut value is applied to those that pass the lepton MVA cut.

2143 The lepton reconstruction and selection is identical to that used in the $t\bar{t}H$ mul-
 2144 tilepton analysis, as documented in Refs. [?, ?]. For details on the reconstruction
 2145 algorithms, isolation, pileup mitigation, and a description of the lepton MVA dis-
 2146 criminator and validation plots thereof, we refer to that document since they are out
 2147 of the scope of this thesis. Three different selections are defined both for the electron
 2148 and muon object identification: the *Loose*, *Fakeable Object*, and *Tight* selection. As
 2149 described in more detail later, these are used for event level vetoes, the fake rate
 2150 estimation application region, and the final signal selection, respectively. The p_T of
 2151 fakeable objects is defined as $0.85 \times p_T(\text{jet})$, where the jet is the one associated to the
 2152 lepton object. This mitigates the dependence of the fake rate on the momentum of
 2153 the fakeable object and thereby improves the precision of the method.

2154 Tables 6.7 and 6.8 list the full criteria for the different selections of muons and
 2155 electrons.

Cut	Loose	Fakeable Object	Tight
$ \eta < 2.5$	✓	✓	✓
p_T	$> 7\text{GeV}$	$> 15\text{GeV}$	$> 15\text{GeV}$
$ d_{xy} < 0.05 \text{ (cm)}$	✓	✓	✓
$ d_z < 0.1 \text{ (cm)}$	✓	✓	✓
$\text{SIP}_{3D} < 8$	✓	✓	✓
$I_{\text{mini}} < 0.4$	✓	✓	✓
MVA ID $> (0.0, 0.0, 0.7)$	✓	✓	✓
$\sigma_{in\eta} < (0.011, 0.011, 0.030)$	—	✓	✓
$\text{H/E} < (0.10, 0.10, 0.07)$	—	✓	✓
$\Delta\eta_{in} < (0.01, 0.01, 0.008)$	—	✓	✓
$\Delta\phi_{in} < (0.04, 0.04, 0.07)$	—	✓	✓
$-0.05 < 1/E - 1/p < (0.010, 0.010, 0.005)$	—	✓	✓
p_T^{ratio}	—	$> 0.5^\dagger / -$	—
jet CSV	—	$< 0.3^\dagger / < 0.8484$	< 0.8484
tight-charge conversion rejection	—	—	✓
Number of missing hits	< 2	$== 0$	$== 0$
lepMVA > 0.90	—	—	✓

Table 6.8: Criteria for each of the three electron selections. In cases where the cut values change between selections, those values are listed in the table. Otherwise, whether the cut is applied is indicated. In some cases, the cut values change for different η ranges. These ranges are $0 < |\eta| < 0.8$, $0.8 < |\eta| < 1.479$, and $1.479 < |\eta| < 2.5$ and the respective cut values are given in the form (value₁, value₂, value₃).

2156 6.3.3 Lepton selection efficiency

2157 Efficiencies of reconstruction and selecting loose leptons are measured both for muons
 2158 and electrons using a tag and probe method on both data and MC, using $Z \rightarrow \ell^+ \ell^-$.
 2159 Corresponding scale factors are derived from the ratio of efficiencies and applied to the
 2160 selected These. Events are produced for the leptonic SUSY analyses using equivalent
 2161 lepton selections and recycled for the $t\bar{t}H$ analysis as well as for this analysis. The
 2162 efficiencies of applying the tight selection as defined in Tables 6.7 and 6.8, on the
 2163 loose leptons are determined again by using a tag and probe method on a sample of
 2164 DY-enriched events. They are documented for the $t\bar{t}H$ analysis in Ref. [?] and are
 2165 exactly equivalent for this analysis.

2166 6.4 Background predictions

2167 The modeling of reducible and irreducible backgrounds in this analysis uses the exact
 2168 methods, analysis code, and ROOT trees used for the $t\bar{t}H$ multilepton analysis. We
 2169 give a brief description of the methods and refer to the documentation of that analysis
 2170 in Refs. [?, ?] for any details.

2171 The backgrounds in three-lepton final states can be split in two broad categories:
 2172 irreducible backgrounds with genuine prompt leptons (i.e. from on-shell W and Z
 2173 boson decays); and reducible backgrounds where at least one of the leptons is “non-
 2174 prompt”, i.e. produced within a hadronic jet, either a genuine lepton from heavy
 2175 flavor decays, or simply mis-reconstructed jets.

2176 Irreducible backgrounds can be reliably estimated directly from Monte-Carlo sim-
 2177 ulated events, using higher-order cross sections or data control regions for the overall
 2178 normalization. This is done in this analysis for all backgrounds involving prompt lep-
 2179 tons: $t\bar{t}W$, $t\bar{t}Z$, $t\bar{t}H$, WZ , ZZ , $W^\pm W^\pm qq$, $t\bar{t}t\bar{t}$, tZq , tZW , WWW , WWZ , WZZ ,
 2180 ZZZ .

2181 Reducible backgrounds, on the other hand, are not well predicted by simulation,
 2182 and are estimated using data-driven methods. In the case of non-prompt leptons, a
 2183 fake rate method is used, where the contribution to the final selection is estimated by
 2184 extrapolating from a sideband (or “application region”) with a looser lepton definition
 2185 (the fakeable object definitions in Tabs. 6.7 and 6.8) to the signal selection. The tight-
 2186 to-loose ratios (or “fake rates”) are measured in several background dominated data
 2187 events with dedicated triggers, subtracting the residual prompt lepton contribution
 2188 using MC. Non-prompt leptons in our signal regions are predominantly produced in $t\bar{t}$
 2189 events, with a much smaller contribution, from Drell–Yan production. The systematic
 2190 uncertainty on the normalization of the non-prompt background estimation is on the

order of 50%, and thereby one of the dominant limitations on the performance of multilepton analyses in general and this analysis in particular. It consists of several individual sources, such as the result of closure tests of the method using simulated events, limited statistics in the data control regions due to necessary prescaling of lepton triggers, and the uncertainty in the subtraction of residual prompt leptons from the control region.

The fake background where the leptons pass the looser selection are weighted according to how many of them fail the tight criteria. Events with a single failing lepton are weighted with the factor $f/(1-f)$ for the estimate to the tight selection region, where f is the fake rate. Events with two failing leptons are given the negative weight $-f_i f_j / (1-f_i)(1-f_j)$, and for three leptons the weight is positive and equal to the product of $f/(1-f)$ factor evaluated for each failing lepton.

Figures 6.2 show the distributions of some relevant kinematic variables, normalized to the cross section of the respective processes and to the integrated luminosity.

6.5 Signal discrimination

The tHq signal is separated from the main backgrounds using a boosted decision tree (BDT) classifier, trained on simulated signal and background events. A set of discriminating variables are given as input to the BDT which produces a output distribution maximizing the discrimination power. Table 6.9 lists the input variables used while Figures 6.3 show their distributions for the relevant signal and background samples, for the three lepton channel. Two BDT classifiers are trained for the two main backgrounds expected in the analysis: events with prompt leptons from $t\bar{t}W$ and $t\bar{t}Z$ (also referred to as $t\bar{t}V$), and events with non-prompt leptons from $t\bar{t}$. The datasets used in the training are the tHq signal (see Tab. 6.1), and LO MADGRAPH samples

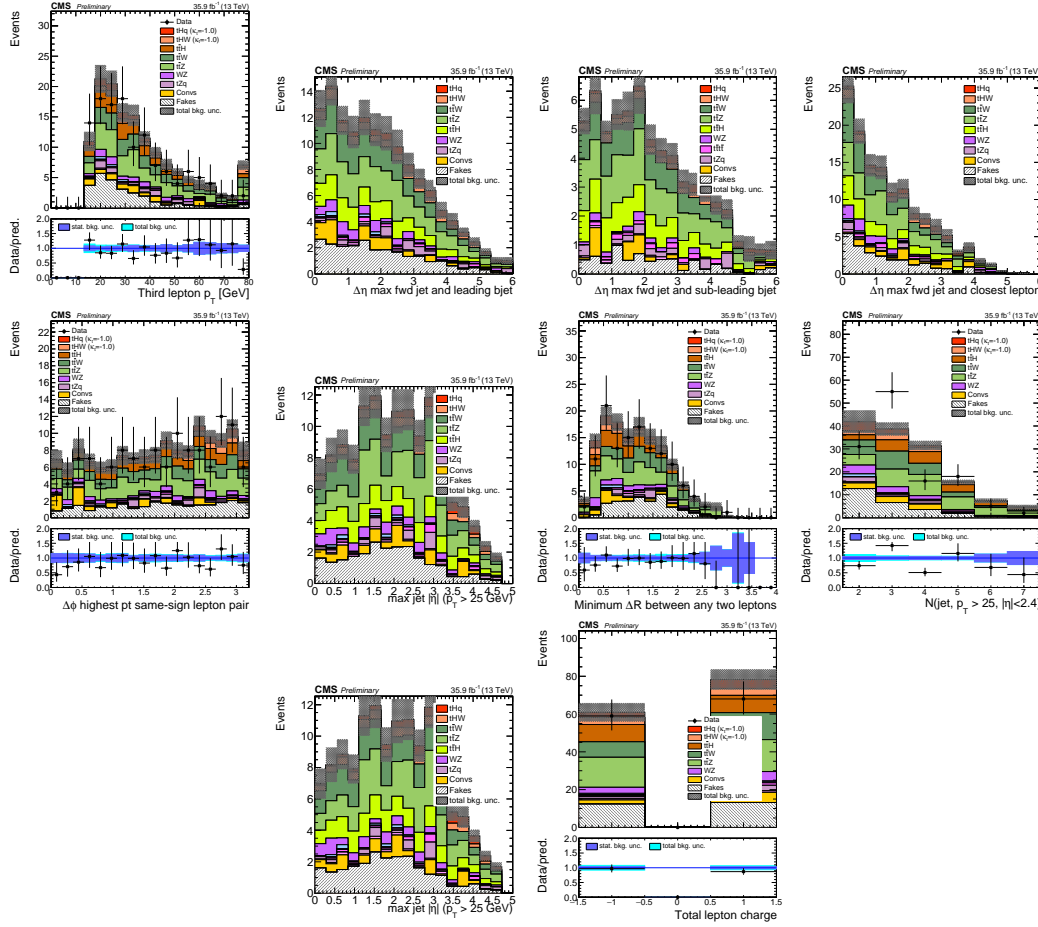


Figure 6.2: Distributions of input variables to the BDT for signal discrimination, three lepton channel, normalized to their cross section and to 35.9 fb^{-1} .

of $t\bar{t}W$ and $t\bar{t}Z$, in an admixture proportional to their respective cross sections (see Tab. 6.4).

The MVA analysis consist of two stages: first a “training” where the MVA method is trained to discriminate between simulated signal and background events, then a “test” stage where the trained algorithm is used to classify different events from the samples. The sample is obtained from a pre-selection (see Tab. ?? with pre-selection cuts). Figures 6.4 show the input variables distributions as seen by the MVA algorithm. Note that in contrast to the distributions in Fig. 6.3 only the main backgrounds ($t\bar{t}$ from simulation, $t\bar{t}V$) are included.

Variable name	Description
nJet25	Number of jets with $p_T > 25$ GeV, $ \eta < 2.4$
MaxEtaJet25	Maximum $ \eta $ of any (non-CSV-loose) jet with $p_T > 25$ GeV
totCharge	Sum of lepton charges
nJetEta1	Number of jets with $ \eta > 1.0$, non-CSV-loose
detaFwdJetBJet	$\Delta\eta$ between forward light jet and hardest CSV loose jet
detaFwdJet2BJet	$\Delta\eta$ between forward light jet and second hardest CSV loose jet (defaults to -1 in events with only one CSV loose jet)
detaFwdJetClosestLep	$\Delta\eta$ between forward light jet and closest lepton
dphiHighestPtSSPair	$\Delta\phi$ of highest p_T same-sign lepton pair
minDRll	minimum ΔR between any two leptons
Lep3Pt/Lep2Pt	p_T of the 3 rd lepton (2 nd for ss2l)

Table 6.9: MVA input discriminating variables

2224 Note that splitting the training in two groups reveals that some variables show
 2225 opposite behavior for the two background sources; potentially screening the discrimi-
 2226 nation power if they were to be used in a single discriminant. For some other variables
 2227 the distributions are similar in both background cases.

2228 From table 6.9, it is clear that the input variables are correlated to some extend.
 2229 These correlations play an important role for some MVA methods like the Fisher
 2230 discriminant method in which the first step consist of performing a linear transfor-
 2231 mation to an phase space where the correlations between variables are removed. In
 2232 case a boosted decision tree (BDT) method however, correlations do not affect the
 2233 performance. Figure 6.6 show the linear correlation coefficients for signal and back-
 2234 ground for the two training cases (the signal values are identical by construction). As
 2235 expected, strong correlations appears for variables related to the forward jet activity.
 2236 Same trend is seen in case of the same sign dilepton channel in Figure ??.

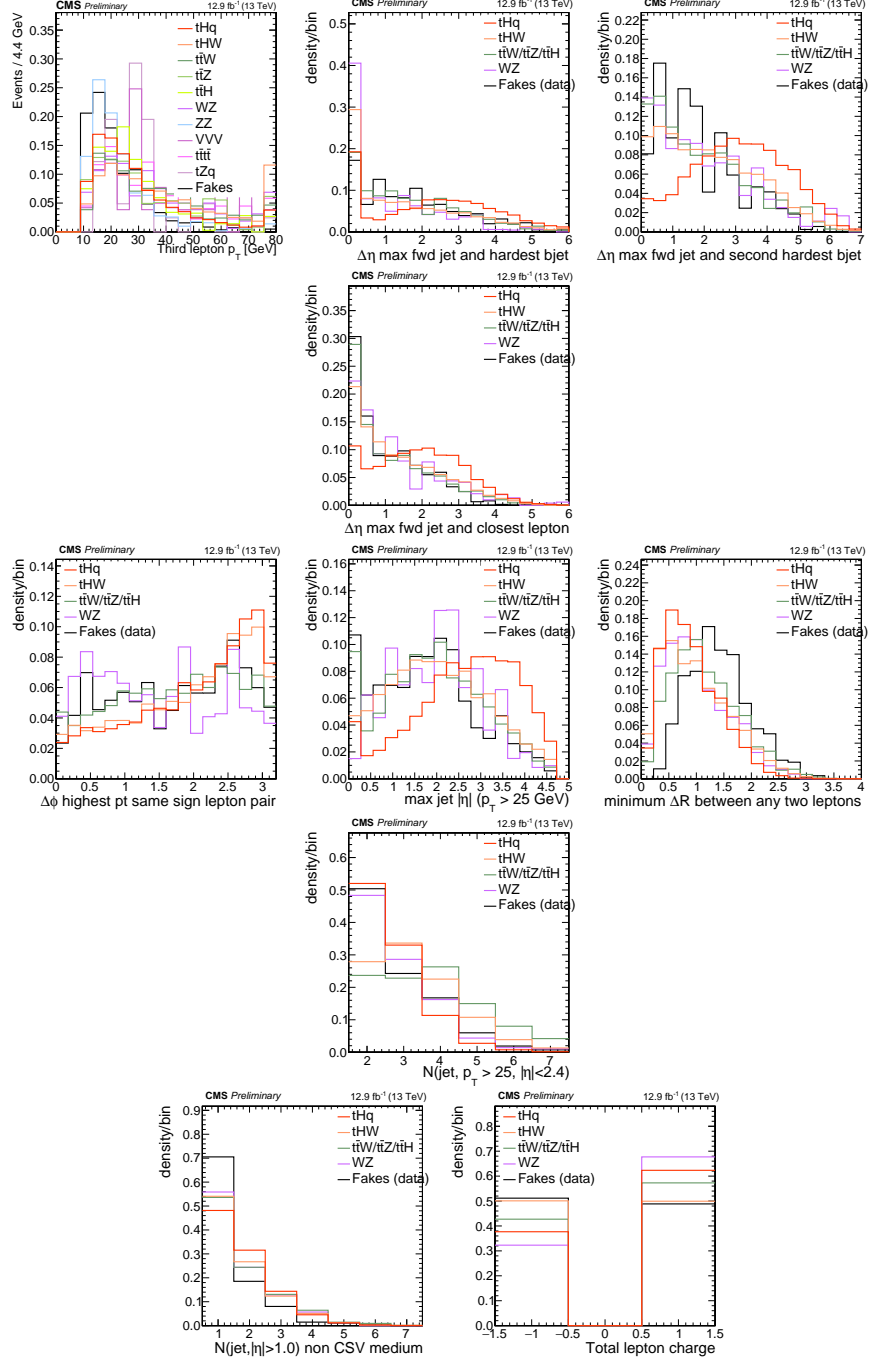


Figure 6.3: Distributions of input variables to the BDT for signal discrimination, three lepton channel.

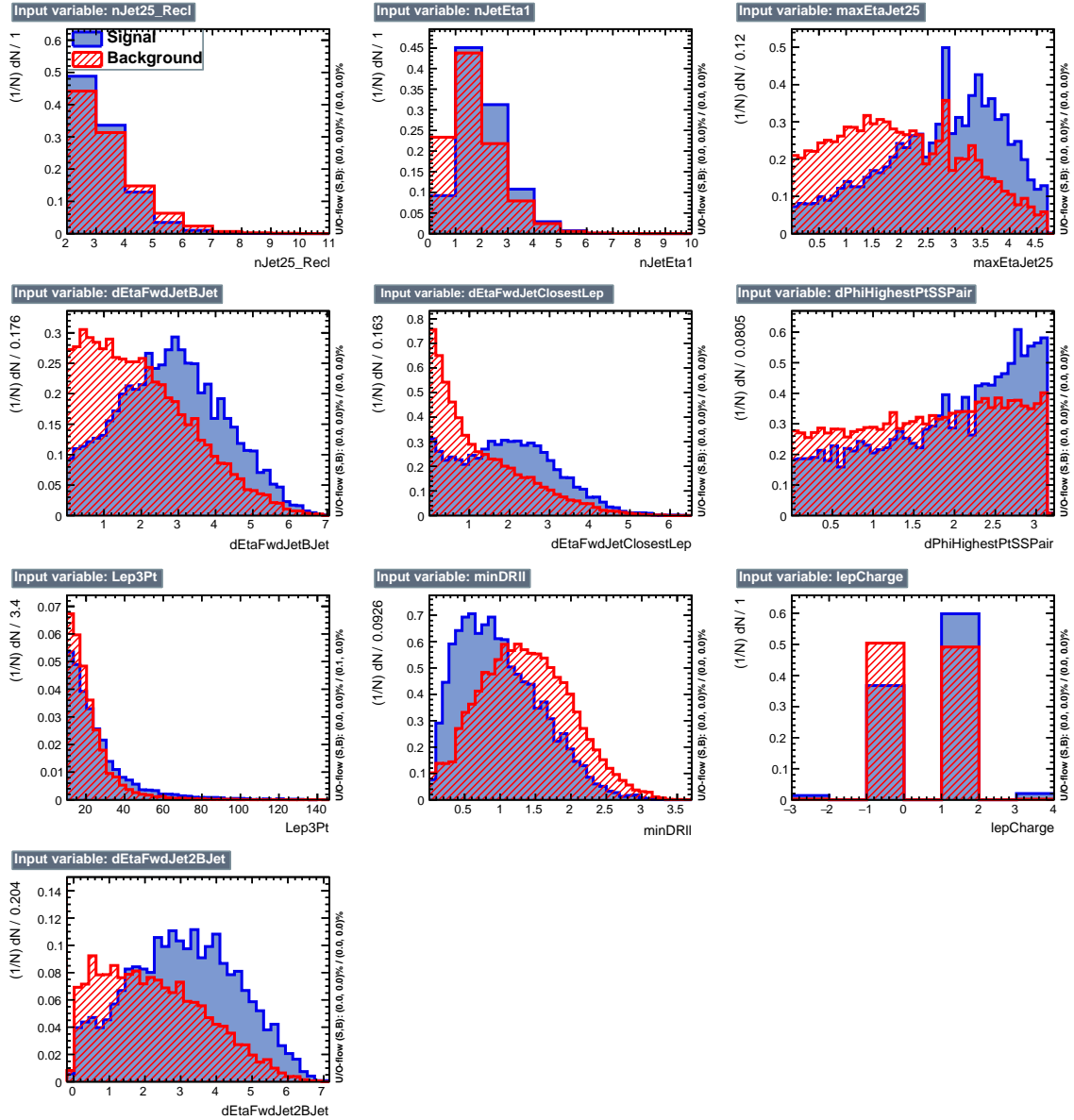


Figure 6.4: BDT inputs as seen by TMVA (signal, in blue, is tHq , background, in red, is $t\bar{t}$) for the three lepton channel, discriminated against $t\bar{t}$ (fakes) background.

2237 6.5.1 Classifiers response

2238 Several MVA algorithms were evaluated to determine the most appropriate method
 2239 for this analysis. The plots in Fig. 6.7 (top) show the background rejection as a
 2240 function of the signal efficiency for $t\bar{t}$ and $t\bar{t}V$ trainings (ROC curves) for the different

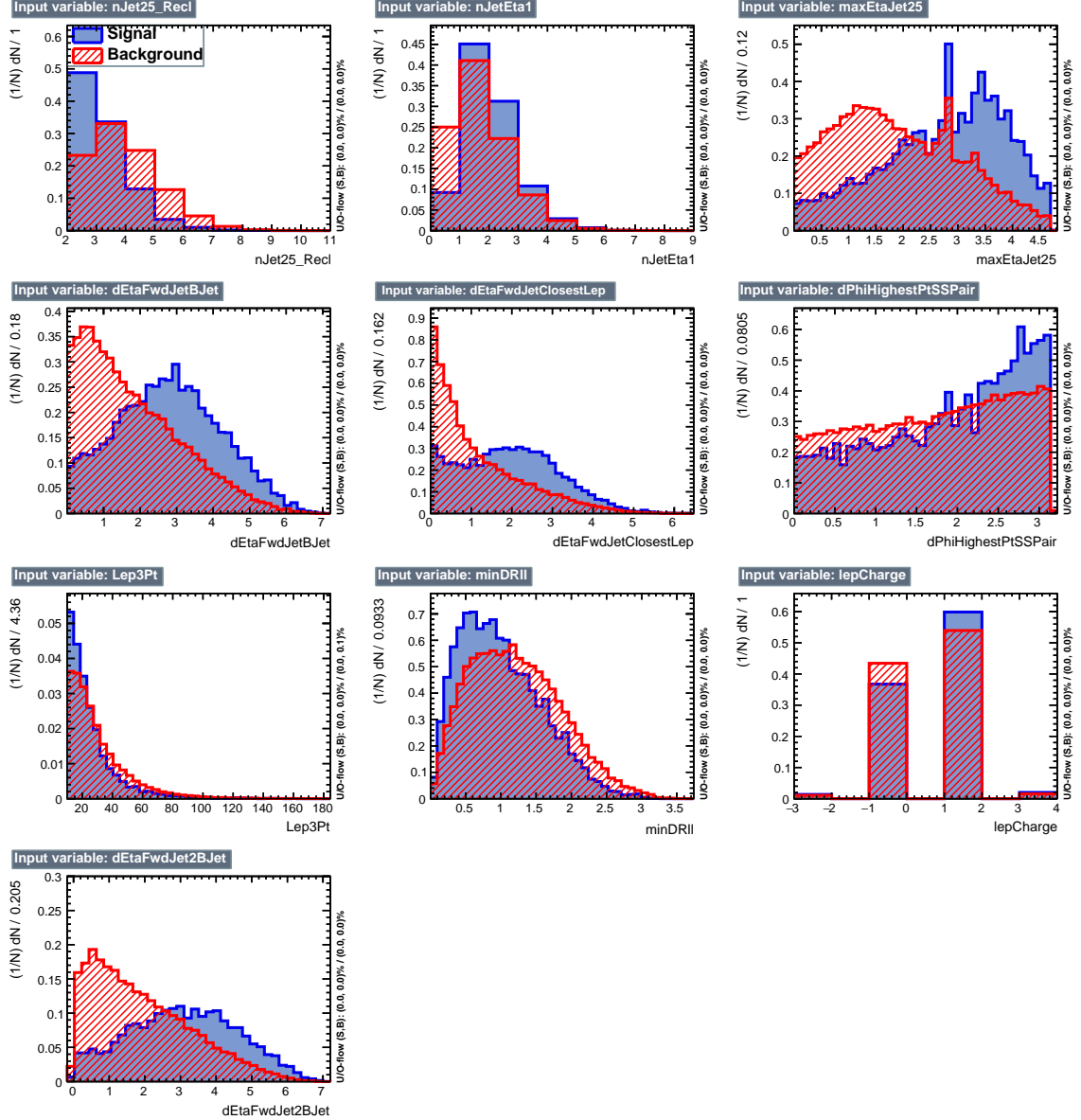


Figure 6.5: BDT inputs as seen by TMVA (signal, in blue, is tHq , background, in red, is $t\bar{t}W+t\bar{t}Z$) for the three lepton channel, discriminated against $t\bar{t}V$ background.

algorithms that were evaluated.

In both cases the gradient boosted decision tree (“BDTA_GRAD”) classifier offers the best results, followed by an adaptive BDT classifier (“BDTA”). The BDTA_GRAD classifier output distributions for signal and backgrounds are shown on the bottom of Fig. 6.7. As expected, a good discrimination power is obtained using default discrim-

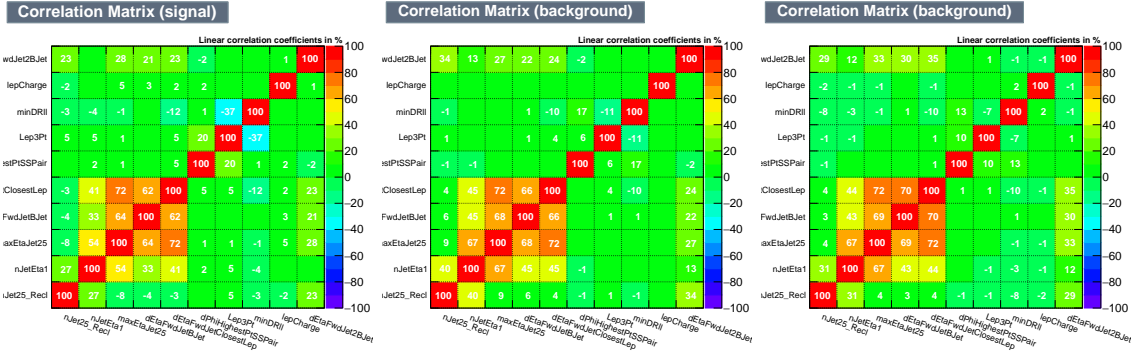


Figure 6.6: Signal (left), $t\bar{t}$ background (middle), and $t\bar{t}V$ background (right.) correlation matrices for the input variables in the TMVA analysis for the three lepton channel.

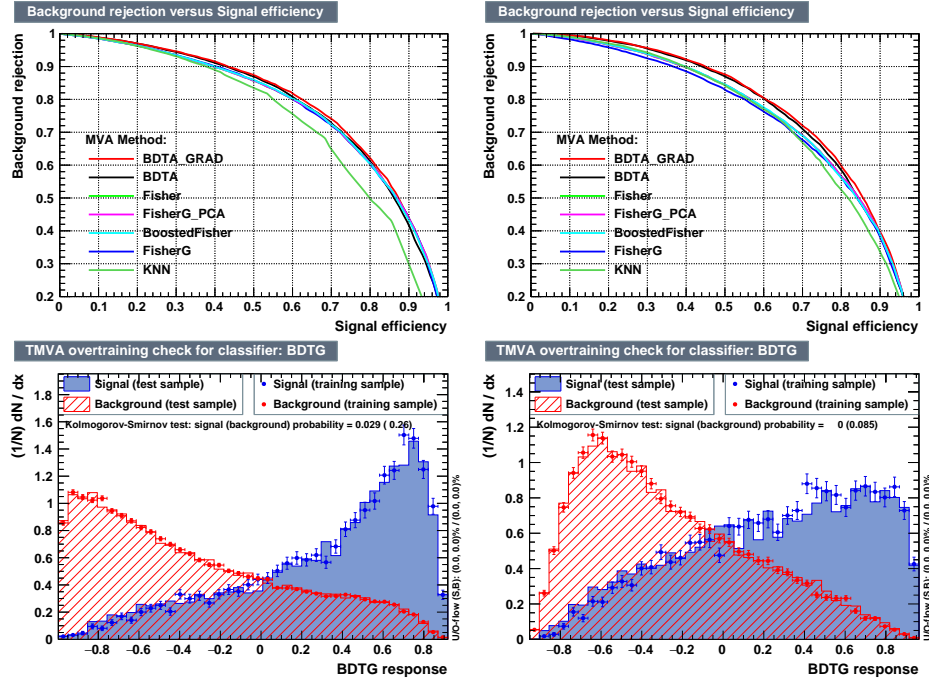


Figure 6.7: Top: background rejection vs signal efficiency (ROC curves) for various MVA classifiers (top) in the three lepton channel against $t\bar{t}V$ (left) and $t\bar{t}$ (right). Bottom: classifier output distributions for the gradient boosted decision trees, for training against $t\bar{t}V$ (left) and against $t\bar{t}$ (right).

inatory parameter values, with minimal overtraining. TMVA provides a ranking of the
input variables by their importance in the classification process, shown in Tab. 6.10.
The TMVA settings used in the BDT training are shown in Tab. 6.11.

ttbar training			ttV training		
Rank	Variable	Importance	Variable	Importance	
1	minDRll	1.329e-01	dEtaFwdJetBJet	1.264e-01	
2	dEtaFwdJetClosestLep	1.294e-01	Lep3Pt	1.224e-01	
3	dEtaFwdJetBJet	1.209e-01	maxEtaJet25	1.221e-01	
4	dPhiHighestPtSSPair	1.192e-01	dEtaFwdJet2BJet	1.204e-01	
5	Lep3Pt	1.158e-01	dEtaFwdJetClosestLep	1.177e-01	
6	maxEtaJet25	1.121e-01	minDRll	1.143e-01	
7	dEtaFwdJet2BJet	9.363e-02	dPhiHighestPtSSPair	9.777e-02	
8	nJetEta1	6.730e-02	nJet25_Recl	9.034e-02	
9	nJet25_Recl	6.178e-02	nJetEta1	4.749e-02	
10	lepCharge	4.701e-02	lepCharge	4.116e-02	

Table 6.10: TMVA input variables ranking for BDTA_GRAD method for the trainings in the three lepton channel. For both trainings the rankings show almost the same 5 variables in the first places.

```

TMVA.Types.kBDT
NTrees=800
BoostType=Grad
Shrinkage=0.10
!UseBaggedGrad
nCuts=50
MaxDepth=3
NegWeightTreatment=PairNegWeightsGlobal
CreateMVAPdfs

```

Table 6.11: TMVA configuration used in the BDT training.

2249 6.6 Additional discriminating variables

2250 Two additional discriminating variables were tested considering the fact that the
 2251 forward jet in the background could come from the pileup; since we have a real
 2252 forward jet in the signal, it could give some improvement in the discriminating power.
 2253 The additional variables describe the forward jet momentum (fwdJetPt25) and the
 2254 forward jet identification(fwdJetPUID). Distributions for these variables in the three
 2255 lepton channel are shown in the figure 6.8. The forward jet identification distribution
 2256 show that for both, signal and background, jets are mostly real jets.

2257 The testing was made including in the MVA input one variable at a time, so we

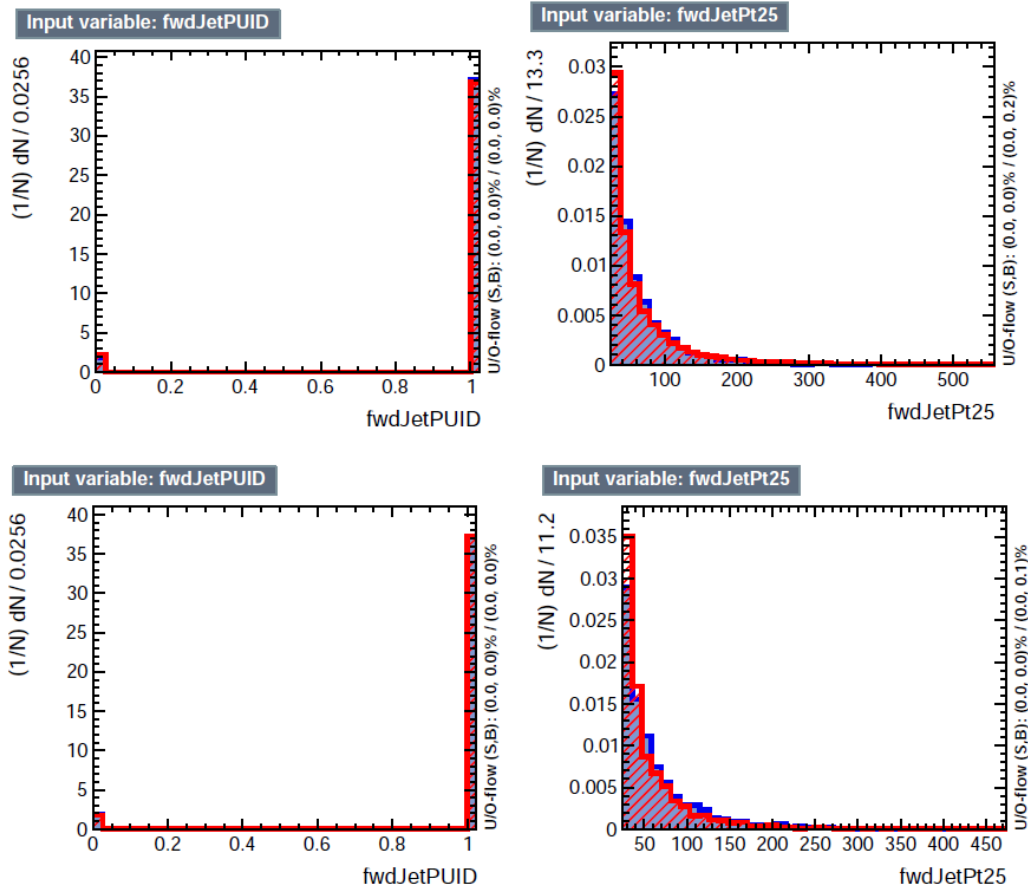


Figure 6.8: Additional discriminating variables distributions for ttV training (Top row) and tt training (bottom row) in the three lepton channel. The origin of the jets in the forward jet identification distribution is tagged as 0 for “pileup jets” while “real jets” are tagged as 1.

2258 can evaluate the discrimination power of each variable, and then both simultaneously.
 2259 `fwdJetPUID` was ranked in the last place in importance (11) in both training (ttV
 2260 and tt) while `fwdJetPt25` was ranked 3 in the ttV training and 7 in the tt training.
 2261 When training using 12 variables, `fwdJetPt25` was ranked 5 and 7 in the ttV and tt
 2262 trainings respectively, while `fwdJetPUID` was ranked 12 in both cases.

2263 The improvement in the discrimination performance provided by the additional
 2264 variables is about 1%, so it was decided not to include them in the procedure. Table
 2265 6.12 show the ROC-integral for all the testing cases we made.

ROC-integral	
base 10 var ttv	0.848
+ fwdJetPUID ttv	0.849
+ fwdJetPt25 ttv	0.856
12 var ttv	0.856
<hr/>	
base 10 var tt	0.777
+ fwdJetPUID tt	0.777
+ fwdJetPt25 tt	0.787
12 var	0.787

Table 6.12: ROC-integral for all the testing cases we made in the evaluation of the additional variables discriminating power. The improvement in the discrimination performance provided by the additional variables is about 1%

2266 **References**

- 2267 [1] J. Schwinger. “Quantum Electrodynamics. I. A Covariant Formulation”. Phys-
2268 ical Review. 74 (10): 1439-61, (1948).
- 2269 [2] R. P. Feynman. “Space-Time Approach to Quantum Electrodynamics”. Physical
2270 Review. 76 (6): 769-89, (1949).
- 2271 [3] S. Tomonaga. “On a Relativistically Invariant Formulation of the Quantum
2272 Theory of Wave Fields”. Progress of Theoretical Physics. 1 (2): 27-42, (1946).
- 2273 [4] D.J. Griffiths, “Introduction to electrodynamics”. 4th ed. Pearson, (2013).
- 2274 [5] F. Mandl, G. Shaw. “Quantum field theory.” Chichester: Wiley (2009).
- 2275 [6] F. Halzen, and A.D. Martin, “Quarks and leptons: An introductory course in
2276 modern particle physics”. New York: Wiley, (1984) .
- 2277 [7] File: Standard_Model_of_Elementary_Particle_dark.svg. (2017, June 12)
2278 Wikimedia Commons, the free media repository. Retrieved November
2279 27, 2017 from <https://www.collegiate-advanced-electricity.com/single-post/2017/04/10/The-Standard-Model-of-Particle-Physics>.
- 2281 [8] E. Noether, “Invariante Variationsprobleme”, Nachrichten von der Gesellschaft
2282 der Wissenschaften zu Göttingen, mathematisch-physikalische Klasse, vol. 1918,
2283 pp. 235-257, (1918).

- 2284 [9] C. Patrignani et al. (Particle Data Group), Chin. Phys. C, 40, 100001 (2016)
2285 and 2017 update.
- 2286 [10] M. Goldhaber, L. Grodzins, A.W. Sunyar “Helicity of Neutrinos”, Phys. Rev.
2287 109, 1015 (1958).
- 2288 [11] Palanque-Delabrouille N et al. “Neutrino masses and cosmology with Lyman-
2289 alpha forest power spectrum”, JCAP 11 011 (2015).
- 2290 [12] M. Gell-Mann. “A Schematic Model of Baryons and Mesons”. Physics Letters.
2291 8 (3): 214-215 (1964).
- 2292 [13] G. Zweig. “An SU(3) Model for Strong Interaction Symmetry and its Breaking”
2293 (PDF). CERN Report No.8182/TH.401 (1964).
- 2294 [14] G. Zweig. “An SU(3) Model for Strong Interaction Symmetry and its Breaking:
2295 II” (PDF). CERN Report No.8419/TH.412(1964).
- 2296 [15] M. Gell-Mann. “The Interpretation of the New Particles as Displaced Charged
2297 Multiplets”. Il Nuovo Cimento 4: 848. (1956).
- 2298 [16] T. Nakano, K, Nishijima. “Charge Independence for V-particles”. Progress of
2299 Theoretical Physics 10 (5): 581-582. (1953).
- 2300 [17] N. Cabibbo, “Unitary symmetry and leptonic decays” Physical Review Letters,
2301 vol. 10, no. 12, p. 531, (1963).
- 2302 [18] M.Kobayashi, T.Maskawa, “CP-violation in the renormalizable theory of weak
2303 interaction,” Progress of Theoretical Physics, vol. 49, no. 2, pp. 652-657, (1973).
- 2304 [19] File: Weak Decay (flipped).svg. (2017, June 12). Wikimedia Com-
2305 mons, the free media repository. Retrieved November 27, 2017 from

- 2306 https://commons.wikimedia.org/w/index.php?title=File:Weak_Decay_(flipped)
2307 .svg&oldid=247498592.
- 2308 [20] Georgia Tech University. Coupling Constants for the Fundamental
2309 Forces(2005). Retrieved January 10, 2018, from http://hyperphysics.phy-
2310 astr.gsu.edu/hbase/Forces/couple.html#c2
- 2311 [21] M. Strassler. (May 31, 2013).The Strengths of the Known Forces. Retrieved Jan-
2312 uary 10, 2018, from https://profmattstrassler.com/articles-and-posts/particle-
2313 physics-basics/the-known-forces-of-nature/the-strength-of-the-known-forces/
- 2314 [22] S.L. Glashow. “Partial symmetries of weak interactions”, Nucl. Phys. 22 579-
2315 588, (1961).
- 2316 [23] A. Salam, J.C. Ward. “Electromagnetic and weak interactions”, Physics Letters
2317 13 168-171, (1964).
- 2318 [24] S. Weinberg, “A model of leptons”, Physical Review Letters, vol. 19, no. 21, p.
2319 1264, (1967).
- 2320 [25] M. Peskin, D. Schroeder, “An introduction to quantum field theory”. Perseus
2321 Books Publishing L.L.C., (1995).
- 2322 [26] A. Pich. “The Standard Model of Electroweak Interactions”
2323 https://arxiv.org/abs/1201.0537
- 2324 [27] F.Bellaiche. (2012, 2 September). “What’s this Higgs boson anyway?”. Retrieved
2325 from: https://www.quantum-bits.org/?p=233
- 2326 [28] M. Endres et al. Nature 487, 454-458 (2012) doi:10.1038/nature11255

- 2327 [29] F. Englert, R. Brout. “Broken Symmetry and the Mass of Gauge
 2328 Vector Mesons”. Physical Review Letters. 13 (9): 321-23.(1964)
 2329 doi:10.1103/PhysRevLett.13.321
- 2330 [30] P.Higgs. “Broken Symmetries and the Masses of Gauge Bosons”. Physical Re-
 2331 view Letters. 13 (16): 508-509,(1964). doi:10.1103/PhysRevLett.13.508.
- 2332 [31] G.Guralnik, C.R. Hagen and T.W.B. Kibble. “Global Conservation Laws
 2333 and Massless Particles”. Physical Review Letters. 13 (20): 585-587, (1964).
 2334 doi:10.1103/PhysRevLett.13.585.
- 2335 [32] CMS collaboration. “Observation of a new boson at a mass of 125 GeV with
 2336 the CMS experiment at the LHC”. Physics Letters B. 716 (1): 30-61 (2012).
 2337 arXiv:1207.7235. doi:10.1016/j.physletb.2012.08.021
- 2338 [33] ATLAS collaboration. “Observation of a New Particle in the Search for the Stan-
 2339 dard Model Higgs Boson with the ATLAS Detector at the LHC”. Physics Letters
 2340 B. 716 (1): 1-29 (2012). arXiv:1207.7214. doi:10.1016/j.physletb.2012.08.020.
- 2341 [34] ATLAS collaboration; CMS collaboration (26 March 2015). “Combined Mea-
 2342 surement of the Higgs Boson Mass in pp Collisions at $\sqrt{s}=7$ and 8 TeV with
 2343 the ATLAS and CMS Experiments”. Physical Review Letters. 114 (19): 191803.
 2344 arXiv:1503.07589. doi:10.1103/PhysRevLett.114.191803.
- 2345 [35] LHC InternationalMasterclasses“When protons collide”. Retrieved from http://atlas.physicsmasterclasses.org/en/zpath_protoncollisions.htm
 2346
- 2347 [36] CMS Collaboration, “SM Higgs Branching Ratios and Total Decay Widths (up-
 2348 date in CERN Report4 2016)”. <https://twiki.cern.ch/twiki/bin/view/LHCPhysics/CERNYellowReportPageBR> , last accessed on 17.12.2017.

- 2350 [37] R.Grant V. “Determination of Higgs branching ratios in $H \rightarrow W^+W^- \rightarrow l\nu jj$
2351 and $H \rightarrow ZZ \rightarrow l^+l^-jj$ channels”. Physics Department, University of Ten-
2352 nessee (Dated: October 31, 2012). Retrieved from <http://aesop.phys.utk.edu/ph611/2012/projects/Riley.pdf>
- 2354 [38] LHC Higgs Cross Section Working Group, Denner, A., Heinemeyer, S. et al.
2355 “Standard model Higgs-boson branching ratios with uncertainties”. Eur. Phys.
2356 J. C (2011) 71: 1753. <https://doi.org/10.1140/epjc/s10052-011-1753-8>
- 2357 [39] F. Maltoni, K. Paul, T. Stelzer, and S. Willenbrock, “Associated production
2358 of Higgs and single top at hadron colliders”, Phys.Rev. D64 (2001) 094023,
2359 [hep-ph/0106293].
- 2360 [40] S. Biswas, E. Gabrielli, F. Margaroli, and B. Mele, “Direct constraints on the
2361 top-Higgs coupling from the 8 TeV LHC data,” Journal of High Energy Physics,
2362 vol. 07, p. 073, (2013).
- 2363 [41] M. Farina, C. Grojean, F. Maltoni, E. Salvioni, and A. Thamm, “Lifting de-
2364 generacies in Higgs couplings using single top production in association with a
2365 Higgs boson,” Journal of High Energy Physics, vol. 05, p. 022, (2013).
- 2366 [42] T.M. Tait and C.-P. Yuan, “Single top quark production as a window to physics
2367 beyond the standard model”, Phys. Rev. D 63 (2000) 014018 [hep-ph/0007298].
- 2368 [43] F. Demartin, F. Maltoni, K. Mawatari, and M. Zaro, “Higgs production in
2369 association with a single top quark at the LHC,” European Physical Journal C,
2370 vol. 75, p. 267, (2015).

- 2371 [44] CMS Collaboration, “Modelling of the single top-quark production in associa-
 2372 tion with the Higgs boson at 13 TeV.” [https://twiki.cern.ch/twiki/bin/](https://twiki.cern.ch/twiki/bin/viewauth/CMS/SingleTopHiggsGeneration13TeV)
 2373 [viewauth/CMS/SingleTopHiggsGeneration13TeV](#), last accessed on 16.01.2018.
- 2374 [45] CMS Collaboration, “SM Higgs production cross sections at $\sqrt{s} =$
 2375 13 TeV.” [https://twiki.cern.ch/twiki/bin/](https://twiki.cern.ch/twiki/bin/view/LHCPhysics/CERNYellowReportPageAt13TeV)
 2376 [view/LHCPhysics/CERNYellowReportPageAt13TeV](#), last accessed on 16.01.2018.
- 2377 [46] S. Dawson, The effective W approximation, Nucl. Phys. B 249 (1985) 42.
- 2378 [47] S. Biswas, E. Gabrielli and B. Mele, JHEP 1301 (2013) 088 [[arXiv:1211.0499 \[hep-ph\]](#)].
- 2380 [48] F. Demartin, B. Maier, F. Maltoni, K. Mawatari, and M. Zaro, “tWH associated
 2381 production at the LHC”, European Physical Journal C, vol. 77, p. 34, (2017).
 2382 [arXiv:1607.05862](#)
- 2383 [49] LHC Higgs Cross Section Working Group, “Handbook of LHC Higgs Cross
 2384 Sections: 4.Deciphering the Nature of the Higgs Sector”, [arXiv:1610.07922](#).
- 2385 [50] J. Ellis, D. S. Hwang, K. Sakurai, and M. Takeuchi.“Disentangling Higgs-Top
 2386 Couplings in Associated Production”, JHEP 1404 (2014) 004, [[arXiv:1312.5736](#)].
- 2387 [51] CMS Collaboration, V. Khachatryan et al., “Precise determination of the mass
 2388 of the Higgs boson and tests of compatibility of its couplings with the standard
 2389 model predictions using proton collisions at 7 and 8 TeV,” [arXiv:1412.8662](#).
- 2390 [52] ATLAS Collaboration, G. Aad et al., “Updated coupling measurements of the
 2391 Higgs boson with the ATLAS detector using up to 25 fb^{-1} of proton-proton
 2392 collision data”, ATLAS-CONF-2014-009.

- 2393 [53] ATLAS and CMS Collaborations, “Measurements of the Higgs boson produc-
 2394 tion and decay rates and constraints on its couplings from a combined ATLAS
 2395 and CMS analysis of the LHC pp collision data at $\sqrt{s} = 7$ and 8 TeV,” (2016).
 2396 CERN-EP-2016-100, ATLAS-HIGG-2015-07, CMS-HIG-15-002.
- 2397 [54] File:Cern-accelerator-complex.svg. Wikimedia Commons,
 2398 the free media repository. Retrieved January, 2018 from
 2399 <https://commons.wikimedia.org/wiki/File:Cern-accelerator-complex.svg>
- 2400 [55] J.L. Caron , “Layout of the LEP tunnel including future LHC infrastructures.”,
 2401 (Nov, 1993). A C Collection. Legacy of AC. Pictures from 1992 to 2002. Re-
 2402 trieval from <https://cds.cern.ch/record/841542>
- 2403 [56] M. Vretenar, “The radio-frequency quadrupole”. CERN Yellow Report CERN-
 2404 2013-001, pp.207-223 DOI:10.5170/CERN-2013-001.207. arXiv:1303.6762
- 2405 [57] L.Evans. P. Bryant (editors). “LHC Machine”. JINST 3 S08001 (2008).
- 2406 [58] CERN Photographic Service.“Radio-frequency quadrupole, RFQ-1”, March
 2407 1983, CERN-AC-8303511. Retrieved from <https://cds.cern.ch/record/615852>.
- 2408 [59] CERN Photographic Service “Animation of CERN’s accelerator net-
 2409 work”, 14 October 2013. DOI: 10.17181/cds.1610170 Retrieved from
 2410 <https://videos.cern.ch/record/1610170>
- 2411 [60] C.Sutton. “Particle accelerator”.Encyclopedia Britannica. July 17, 2013. Re-
 2412 trieval from <https://www.britannica.com/technology/particle-accelerator>.
- 2413 [61] L.Guiraud. “Installation of LHC cavity in vacuum tank.”. July 27 2000. CERN-
 2414 AC-0007016. Retrieved from <https://cds.cern.ch/record/41567>.

- 2415 [62] J.L. Caron, “Magnetic field induced by the LHC dipole’s superconducting coils”.
2416 March 1998. AC Collection. Legacy of AC. Pictures from 1992 to 2002. LHC-
2417 PHO-1998-325. Retrieved from <https://cds.cern.ch/record/841511>
- 2418 [63] AC Team. “Diagram of an LHC dipole magnet”. June 1999. CERN-DI-9906025
2419 retrieved from <https://cds.cern.ch/record/40524>.
- 2420 [64] CMS Collaboration “Public CMS Luminosity Information”.
2421 <https://twiki.cern.ch/twiki/bin/view/CMSPublic/LumiPublicResults#2016>
2422 _proton_proton_13_TeV_collis, last accessed 24.01.2018
- 2423 [65] J.L. Caron. “LHC Layout” AC Collection. Legacy of AC. Pictures
2424 from 1992 to 2002. September 1997, LHC-PHO-1997-060. Retrieved from
2425 <https://cds.cern.ch/record/841573>.
- 2426 [66] J.A. Coarasa. “The CMS Online Cluster: Setup, Operation and Maintenance
2427 of an Evolving Cluster”. ISGC 2012, 26 February - 2 March 2012, Academia
2428 Sinica, Taipei, Taiwan.
- 2429 [67] CMS Collaboration. “The CMS experiment at the CERN LHC” JINST 3 S08004
2430 (2008).
- 2431 [68] CMS Collaboration. “CMS detector drawings 2012” CMS-PHO-GEN-2012-002.
2432 Retrieved from <http://cds.cern.ch/record/1433717>.
- 2433 [69] R. Breedon. “View through the CMS detector during the cooldown of the
2434 solenoid on February 2006. CMS Collection”, February 2006, CMS-PHO-
2435 OREACH-2005-004, Retrieved from <https://cds.cern.ch/record/930094>.
- 2436 [70] A. Dominguez et. al. “CMS Technical Design Report for the Pixel Detector
2437 Upgrade”, CERN-LHCC-2012-016. CMS-TDR-11.

- 2438 [71] CMS Collaboration. “Description and performance of track and primary-vertex
2439 reconstruction with the CMS tracker,” Journal of Instrumentation, vol. 9, no.
2440 10, p. P10009,(2014).
- 2441 [72] CMS Collaboration and M. Brice. “Images of the CMS Tracker Inner
2442 Barrel”, November 2008, CMS-PHO-TRACKER-2008-002. Retrieved from
2443 <https://cds.cern.ch/record/1431467>.
- 2444 [73] M. Weber. “The CMS tracker”. 6th international conference on hyperons, charm
2445 and beauty hadrons Chicago, June 28-July 3 2004.
- 2446 [74] CMS Collaboration. “Projected Performance of an Upgraded CMS Detector at
2447 the LHC and HL-LHC: Contribution to the Snowmass Process”. Jul 26, 2013.
2448 arXiv:1307.7135
- 2449 [75] L. Veillet. “End assembly of HB with EB rails and rotation inside SX ”,January 2002. CMS-PHO-HCAL-2002-002. Retrieved from
2450 <https://cds.cern.ch/record/42594>.
- 2452 [76] J. Puerta-Pelayo.“First DT+RPC chambers installation round in the
2453 UX5 cavern.”. January 2007, CMS-PHO-OREACH-2007-001. Retrieved from
2454 <https://cds.cern.ch/record/1019185>
- 2455 [77] X. Cid Vidal and R. Cid Manzano. “CMS Global Muon Trigger” web
2456 site: Taking a closer look at LHC. Retrieved from https://www.lhc-closer.es/taking_a_closer_look_at_lhc/0.lhc_trigger
- 2458 [78] WLCG Project Office, “Documents & Reference - Tiers - Structure,” (2014).
2459 <http://wlcg.web.cern.ch/documents-reference> , last accessed on 30.01.2018.

- 2460 [79] CMS Collaboration. “CMSSW Application Framework”,
 2461 <https://twiki.cern.ch/twiki/bin/view/CMSPublic/WorkBookCMSSWFramework>,
 2462 last accesses 06.02.2018
- 2463 [80] A. Buckleya, J. Butterworthb, S. Giesekec, et. al. “General-purpose event gen-
 2464 erators for LHC physics”. arXiv:1101.2599v1 [hep-ph] 13 Jan 2011
- 2465 [81] A. Quadt. “Top Quark Physics at Hadron Colliders”. Advances in the Physics
 2466 of Particles and Nuclei. Springer-Verlag Berlin Heidelberg. DOI: 10.1007/978-
 2467 3-540-71060-8 (2007)
- 2468 [82] DurhamHep Data Project, “The Durham HepData Project - PDF Plotter.”
 2469 <http://hepdata.cedar.ac.uk/pdf/pdf3.html> , last accessed on 02.02.2018.
- 2470 [83] F. Maltoni, G. Ridolfi, and M. Ubiali, “b-initiated processes at the LHC: a
 2471 reappraisal,” Journal of High Energy Physics, vol. 07, p. 022, (2012).
- 2472 [84] B. Andersson, G. Gustafson, G. Ingelman and T. Sjostrand, “Parton fragmen-
 2473 tation and string dynamics”, Physics Reports, Vol. 97, No. 2-3, pp. 31-145,
 2474 1983.
- 2475 [85] CMS Collaboration, “Event generator tunes obtained from underlying event
 2476 and multiparton scattering measurements;” European Physical Journal C, vol.
 2477 76, no. 3, p. 155, (2016).
- 2478 [86] J. Alwall et. al., “The automated computation of tree-level and next-to-leading
 2479 order differential cross sections, and their matching to parton shower simula-
 2480 tions,” Journal of High Energy Physics, vol. 07, p. 079, (2014).

- 2481 [87] S. Frixione, P. Nason, and C. Oleari, “Matching NLO QCD computations with
2482 Parton Shower simulations: the POWHEG method,” Journal of High Energy
2483 Physics, vol. 11, p. 070, (2007).
- 2484 [88] S. Agostinelli et al., “GEANT4: A Simulation toolkit,” Nuclear Instruments
2485 and Methods in Physics, vol. A506, pp. 250–303, (2003).
- 2486 [89] J.Allison et.al.,“Recent developments in Geant4”, Nuclear Instruments and
2487 Methods in Physics Research A 835 (2016) 186-225.
- 2488 [90] CMS Collaboration “Full Simulation Offline Guide”, <https://twiki.cern.ch/twiki/bin/view/CMSPublic/SWGuideSimulation>, last accessed 04.02.2018
- 2489
- 2490 [91] A. Giammanco. “The Fast Simulation of the CMS Experiment” J. Phys.: Conf.
2491 Ser. 513 022012 (2014)
- 2492 [92] A.M. Sirunyan et. al. “Particle-flow reconstruction and global event description
2493 with the CMS detector”, JINST 12 P10003 (2017) <https://doi.org/10.1088/1748-0221/12/10/P10003>.
- 2494
- 2495 [93] The CMS Collaboration. “ Description and performance of track and pri-
2496 mary vertex reconstruction with the CMS tracker”. JINST 9 P10009 (2014).
2497 doi:10.1088/1748-0221/9/10/P10009
- 2498 [94] J. Incandela. “Status of the CMS SM Higgs Search” July 4, 2012. Pdf slides.
2499 Retrieved from https://indico.cern.ch/event/197461/contributions/1478917/attachments/290954/406673/CMS_4July2012_Final.pdf
- 2500
- 2501 [95] P. Billoir and S. Qian, “Simultaneous pattern recognition and track fitting by
2502 the Kalman filtering method”, Nucl. Instrum. Meth. A 294 219. (1990).

- 2503 [96] W. Adam, R. Fruhwirth, A. Strandlie and T. Todorov, “Reconstruction of
 2504 electrons with the Gaussian sum filter in the CMS tracker at LHC”, eConf
 2505 C 0303241 (2003) TULT009 [physics/0306087].
- 2506 [97] K. Rose, “Deterministic Annealing for Clustering, Compression, Classification,
 2507 Regression and related Optimisation Problems”, Proc. IEEE 86 (1998) 2210.
- 2508 [98] R. Fruhwirth, W. Waltenberger and P. Vanlaer, “ Adaptive Vertex Fitting”,
 2509 CMS Note 2007-008 (2007).
- 2510 [99] CMS collaboration, “Performance of CMS muon reconstruction in pp collision
 2511 events at $\sqrt{s} = 7$ TeV ”, JINST 7 P10002 2012, [arXiv:1206.4071].
- 2512 [100] M. Cacciari, G. P. Salam, and G. Soyez, “The anti- k_t jet clustering algorithm,”
 2513 Journal of High Energy Physics, vol. 04, p. 063, (2008).
- 2514 [101] B. Dorney. “Anatomy of a Jet in CMS”. Quantum Diaries. June
 2515 1st, 2011. Retrieved from <https://www.quantumdiaries.org/2011/06/01/anatomy-of-a-jet-in-cms/>
- 2517 [102] The CMS Collaboration.“Event Displays from the high-energy collisions at 7
 2518 TeV”, May 2010, CMS-PHO-EVENTS-2010-007, Retrieved from <https://cds.cern.ch/record/1429614>.
- 2520 [103] The CMS collaboration. “Determination of jet energy calibration and transverse
 2521 momentum resolution in CMS”. JINST 6 P11002 (2011). <http://dx.doi.org/10.1088/1748-0221/6/11/P11002>
- 2523 [104] The CMS Collaboration, “Introduction to Jet Energy Corrections at
 2524 CMS.”. <https://twiki.cern.ch/twiki/bin/view/CMS/IntroToJEC>, last ac-
 2525 cessed 10.02.2018.

- 2526 [105] CMS Collaboration Collaboration. “Identification of b quark jets at the CMS
2527 Experiment in the LHC Run 2”. Tech. rep. CMS-PAS-BTV-15-001. Geneva:
2528 CERN, (2016). <https://cds.cern.ch/record/2138504>.
- 2529 [106] CMS Collaboration Collaboration. “Performance of missing energy reconstruc-
2530 tion in 13 TeV pp collision data using the CMS detector”. Tech. rep. CMS-PAS-
2531 JME16-004. Geneva: CERN, 2016. <https://cds.cern.ch/record/2205284>.
- 2532 [107] K. Skovpen. “Event displays highlighting the main properties of heavy flavour
2533 jets in the CMS Experiment”, Aug 2017, CMS-PHO-EVENTS-2017-006. Re-
2534 trieved from <https://cds.cern.ch/record/2280025>.
- 2535 [108] G. Cowan. “Topics in statistical data analysis for high-energy physics”.
2536 arXiv:1012.3589v1
- 2537 [109] A. Hoecker et al., “TMVA-Toolkit for multivariate data analysis”
2538 arXiv:physics/0703039v5 (2009)
- 2539 [110] I. Antcheva et al., “ROOT-A C++ framework for petabyte data storage, sta-
2540 tistical analysis and visualization ,” Computer Physics Communications, vol.
2541 182, no. 6, pp. 1384–1385, (2011).
- 2542 [111] L. Lista. “Statistical Methods for Data Analysis in Particle Physics”, 2nd
2543 ed. Springer International Publishing. (2017) <https://dx.doi.org/10.1007/978-3-319-62840-0>
- 2545 [112] Y. Coadou. “Boosted decision trees”, ESIPAP, Archamps, 9 Febru-
2546 ary 2016. Lecture. Retrieved from https://indico.cern.ch/event/472305/contributions/1982360/attachments/1224979/1792797/ESIPAP_MVA160208-BDT.pdf

- 2549 [113] J.H. Friedman. “Greedy function approximation: A gradient boosting ma-
2550 chine”. Ann. Statist. Volume 29, Number 5 (2001), 1189-1232. https://projecteuclid.org/download/pdf_1/euclid-aos/1013203451.
- 2552 [114] F. James, M. Roos, “MINUIT: Function minimization and error analysis”. Cern
2553 Computer Centre Program Library, Geneve Long Write-up No. D506, 1989
- 2554 [115] J. Neyman and E. S. Pearson, “On the problem of the most efficient tests
2555 of statistical hypotheses”. Philosophical Transactions of the Royal Society of
2556 London. Series A, Containing Papers of a Mathematical or Physical Character.
2557 Vol. 231 (1933), pp. 289-337